

PETRO VIETNAM

JOURNAL

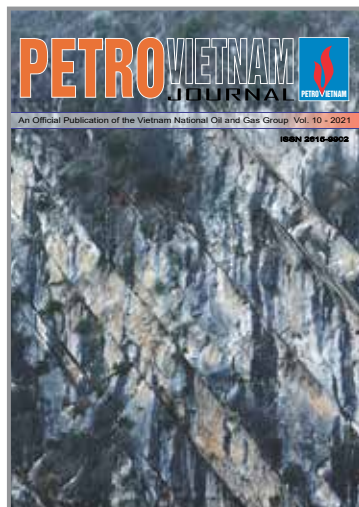


An Official Publication of the Vietnam National Oil and Gas Group Vol. 10 - 2021

ISSN 2615-9902

PETROVIETNAM Vol. 10 - 2021





EDITOR-IN-CHIEF

Dr. Le Xuan Huyen

DEPUTY EDITOR-IN-CHIEF

Dr. Le Manh Hung

Dr. Phan Ngoc Trung

EDITORIAL BOARD MEMBERS

Dr. Trinh Xuan Cuong

Dr. Nguyen Anh Duc

MSc. Vu Dao Minh

M.A. Tran Thai Ninh

MSc. Duong Manh Son

MSc. Le Ngoc Son

Assoc. Prof. Dr. Le Van Sy

Eng. Le Hong Thai

M.A. Bui Minh Tien

MSc. Nguyen Van Tuan

MSc. Pham Xuan Trung

Dr. Tran Quoc Viet

SECRETARY

MSc. Le Van Khoa

M.A. Nguyen Thi Viet Ha

DESIGNED BY

Le Hong Van

MANAGEMENT

Vietnam Petroleum Institute

CONTACT ADDRESS

16th Floor, VPI Tower, Trung Kinh street, Yen Hoa ward, Cau Giay district, Ha Noi

*Tel: (+84-24) 37727108 * Fax: (+84-24) 37727107 * Email: tcdk@pvn.vn/pvj@pvn.vn*

Mobile: (+84)982288671



PETROVIETNAM JOURNAL
Volume 10/2021, p. 4 - 16
ISSN 2615-9902

PETROVIETNAM
JOURNAL

SOME RESULTS OF SEISMIC TRAVEL-TIME REFLECTION TOMOGRAPHY STUDY

Pham Thi Hoang Ha, Doan Huy Hien, To Quang Minh, Mai Thi Lua, Nguyen Hoang Anh
Vietnam Petroleum Institute
Email: haph@vpi.vn.vn
<https://doi.org/10.2306/PVJ.2021.10-02>

Summary
Velocity model is essential for seismic data processing as it plays an important role in migration processes as well as time depth conversion. There are several techniques to reach that goal, among which tomographic inversion is an efficient one. As an upgrade version of handpicked velocity analysis, the tomography technique is based on the reflection ray tracing and conjugate gradient method to estimate an optimum velocity model and can create an initial high quality model for other intensive imaging and modelling module such as reverse-time migration (RTM) and full-waveform inversion (FWI). For the mentioned benefit, we develop a seismic travel-time reflection tomography (SIRT) module to study the accuracy of the approach along with building the technical capability in seismic processing. The accuracy of the module has been tested by both synthetic and real seismic field data, the efficiency and the accuracy of the model have been proven in terms of development method as well as field data application.

Key words: Seismic signal processing, seismic reflection, ray tracing, velocity modelling, seismic tomography, tomographic inversion.

1. Introduction
Velocity model is one of the most important features extracted from the seismic reflection data as it has been used for many purposes such as depth imaging, time-depth conversion and geomechanical model building. The resolution of velocity model building is highly dependent on the complexity of the method to be used and the resolution of the initial model and seismic data. For example, the velocity analysis is the simplest and fastest way to create the velocity model, however, the resolution of this method is poor in both lateral and time directions as the distance between two picking common depth points (CDP) is much higher than the one between two initial CDP intervals. Similarly, within a CDP semblance spectrum for velocity picking, the picking time interval is much higher than the time sampling rate. Full waveform inversion (FWI) in the reverse way, gives the velocity model the highest resolution and accuracy. However, the computational cost is too high to be used widely in the seismic reflection industry. To reach the balance between the accuracy and computational cost, the seismic reflection tomography (SIRT) approach is an alternative method for getting the velocity model for migration purposes and to be used as the initial model for FWI problem, which produces a higher resolution than SIRT.

Tomography is an inversion process that provides a tool for velocity estimations from multichannel seismic reflection data. Tomography can be performed either in the prior-migration domain or in the post-migration domain. In each of these domains, we can access two types of information: kinematic (travel time) and dynamic (amplitude and phase) [1]. Thus, we have at least four ways to sort the tomographic inverse problem out. Table 1 gives a summary of the approaches used for velocity estimation.

During this work, we demonstrate a study of ray-based reflection travel time tomography applied for synthetic and field velocity models. The workflow of this approach is shown in Figure 1. There are several reasons why we chose this kind of approach for studying velocity

4

PETROVIETNAM JOURNAL
Volume 10/2021, p. 17 - 32
ISSN 2615-9902

PETROVIETNAM
JOURNAL

A PRACTICAL METHOD FOR PLANNING LARGE NUMBER OF HORIZONTAL WELLS WITH A RESERVOIR MODEL FOR A FIELD DEVELOPMENT PLAN

Guido Fera', Dinh Viet Anh'
*Schlumberger
Petrovietnam Exploration Production Corporation
Email: anh@shvpp.com.vn
<https://doi.org/10.2306/PVJ.2021.10-03>

Summary
The most advanced technique to evaluate different solutions proposed for a field development plan consists of building a numerical model to simulate the production performance of each alternative. Fields covering hundreds of square kilometers frequently require a large number of wells. There are studies and software concerning optimal planning of vertical wells for the development of a field. However, only few studies cover planning of a large number of horizontal wells seeking full population on a regular pattern.

One of the criteria for horizontal well planning is selecting the well positions that have the best reservoir properties and certain standoffs from oil/water contact. The wells are then ranked according to their performances. Other criteria include the geometry and spacing of the wells. Placing hundreds of well individually according to these criteria is highly time consuming and can become impossible under time restraints. A method for planning a large number of horizontal wells in a regular pattern in a simulation model significantly reduces the time required for a reservoir production forecast using simulation software. The proposed method is implemented by a computer script and takes into account not only the aforementioned criteria, but also new well requirements concerning existing wells, development area boundaries, and reservoir geological structure features.

Some of the conclusions drawn from a study on this method are (1) the new method saves a significant amount of working hours and avoids human errors, especially when many development scenarios need to be considered; (2) a large reservoir with hundreds of wells may have infinite possible solutions, and this approach has the aim of giving the most significant one; and (3) a horizontal well planning module would be a useful tool for commercial simulation software to ease engineers' tasks.

Key words: Asset and portfolio management, field development optimisation and planning, water saturation, reservoir simulation, directional drilling.

1. Introduction
The designs of development plans for oil and gas fields are based on the definition of a drilling schedule. Development wells are drilled to (a) reach and support a production plateau; (b) maximise the hydrocarbon recovery; and (c) provide injection for pressure support or secondary recovery.

The task addressed in this work is a full population of the field with as many horizontal wells as needed to get the maximum possible production rate and optimal desired production that is maintained for several years. This study should be distinguished from other studies available in the literature that are focused on production optimisation with a minimum number of well locations yielding a high recovery per well. The well population in this work is based on a regular pattern rather than selection of optimal random locations. The evaluation of every possible location on a regular pattern was found to be a frequent request from field operators because it suits their local and economic circumstances. Interference be-

17

SCIENTIFIC RESEARCH



PETROLEUM EXPLORATION & PRODUCTION

4. Some results of seismic travel-time reflection tomography study

17. A practical method for planning large number of horizontal wells with a reservoir model for a field development plan

33. Development of HFU-based permeability prediction models using core data for characterisation of a heterogeneous Oligocene sand in the Nam Con Son basin

40. Geomechanical model and sanding onset assessment: A field case study in Vietnam

47. An overview of the application of machine learning in predictive maintenance

PETROLEUM ECONOMICS & MANAGEMENT
PETROVIETNAM JOURNAL
 Volume 10/2021, p. 62-71
 ISSN 2615-9902

ENERGY INTEGRATION: GREEN FUTURE FOR LATE-LIFE OFFSHORE OIL AND GAS ASSETS

Huyen Thi Hoang¹, Huyen Thi Thanh Lu²
¹Vietnam Petroleum Institute
²Ministry of Industry and Trade
 Email: hhoang@vpi.gov.vn
<https://doi.org/10.25805/PVJ.10.2021.62>

Summary

In recent years, the oil and gas industry has been facing objections from a public greatly concerned with the severe environmental impact caused by fossil fuels and their infrastructures, and strong demands from policy makers seeking to meet decarbonisation goals. Amidst a global energy transition, the future demand, finance, and social responsibilities of oil and gas companies are increasingly in question. One of the biggest problems of the industry is what are the 'green' solutions for the late-life offshore oil and gas assets. Energy integration with reusing or repurposing oil and gas assets for new technologies could be a worthwhile investment strategy helping reduce carbon emission from oil and gas production as well as accelerating carbon capture and storage (CCS) and green hydrogen development to support the global decarbonisation. According to research, the late-life offshore oil and gas assets play an important role in energy integration while helping to have more opportunities to develop the new technologies that are in the early stage of development with high capex, necessary to make them more economically attractive and facilitate maximum energy integration. Reusing or repurposing oil and gas infrastructure can lead to 30% capex saving and million tons of CO₂ eq emission reductions.

In this paper, potential concepts of energy integration for offshore oil and gas assets are introduced, and some lessons learned and implications for reusing or repurposing late-life offshore assets for Vietnam are also presented.

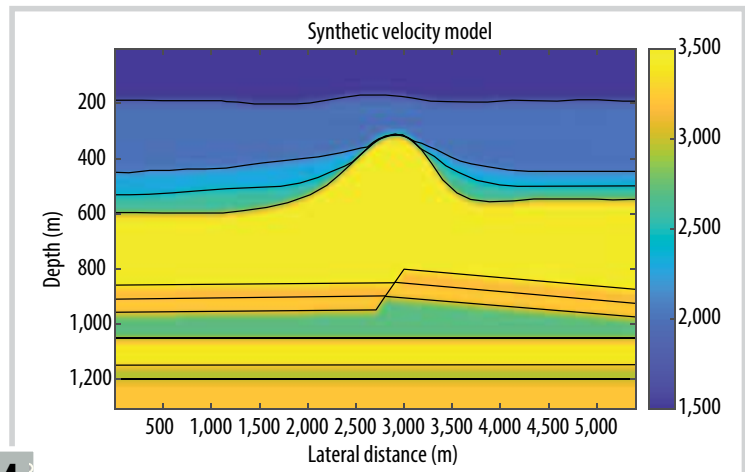
Key words: Energy integration, late-life offshore oil and gas assets, electrification, green hydrogen, carbon capture and storage.

1. Introduction

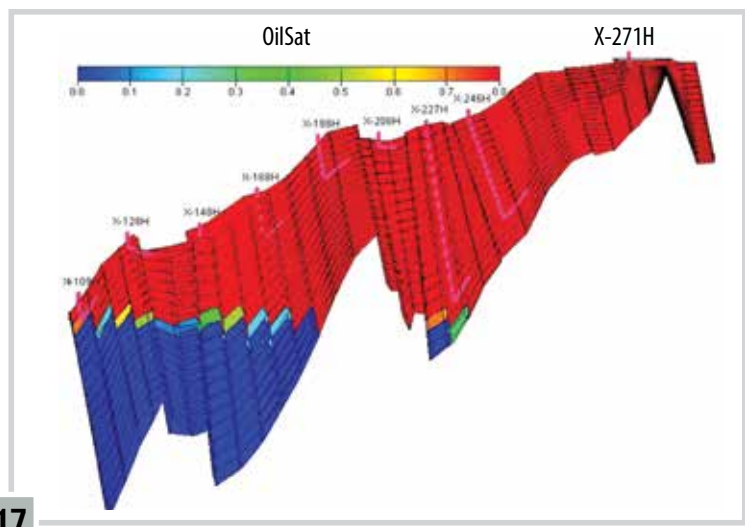
After years of production, the oil and gas industry is facing an increasing demand for decommissioning which requires large costs and negatively affects the surrounding environment. Though worldwide estimates vary greatly, on average, decommissioning (decom) a complete platform may cost USD 15 million to USD 20 million in shallow waters (such as in the Gulf of Mexico), about GBP 30 million (USD 40 million) for small platforms, and GBP 200 million (USD 260 million) for large structures in deep waters (such as in the UK North Sea) [1]. According to Rystad Energy [2], the total value of the global pool of decom projects that will accumulate through 2024 could reach USD 42 billion, dominated by the UK North Sea. Besides, post-decom environment impacts are also of great concern since a typical eight leg structure provides a home for 12,000 to 14,000 fishes, and a typical four-leg structure provides 2 to 3 acres of habitat for hundreds of marine species, according to a study by the Coastal Marine Institute [3]. Therefore, one of the critical issues in the oil and gas industry is how to reduce the decom cost and protect the environment.

Conventionally, late-life offshore oil and gas assets must be decommissioned if they cannot work longer or be reused/repurposed. If the scrap steel market is stable and developed, contractors will get scrap revenue from the sale [4]. Otherwise, the scrap yards will charge the contractors to unload steel platforms [5]. Operating contractors are responsible for executing safe and environmentally sound decommissioning when operations cease. Nevertheless, almost all scrapping yards are on beaches so pollutants can cause serious environmental harm with long-term effects for occupational, public, and environmental health [4]. A 'green' solution for offshore oil and gas assets is

62 PETROVIETNAM JOURNAL VOL 10/2021



4



17



PETROLEUM ECONOMICS & MANAGEMENT

62. Energy integration: Green future for late-life offshore oil and gas assets

SOME RESULTS OF SEISMIC TRAVEL-TIME REFLECTION TOMOGRAPHY STUDY

Pham The Hoang Ha, Doan Huy Hien, Ta Quang Minh, Mai Thi Lua, Nguyen Hoang Anh

Vietnam Petroleum Institute

Email: hapth@vpi.pvn.vn

<https://doi.org/10.47800/PVJ.2021.10-01>

Summary

Velocity model is essential for seismic data processing as it plays an important role in migration processes as well as time depth conversion. There are several techniques to reach that goal, among which tomographic inversion is an efficient one. As an upgrade version of handpicked velocity analysis, the tomography technique is based on the reflection ray tracing and conjugate gradient method to estimate an optimum velocity model and can create an initial high quality model for other intensive imaging and modelling module such as reverse-time migration (RTM) and full-waveform inversion (FWI). For the mentioned benefit, we develop a seismic travel-time reflection tomography (SeisT) module to study the accuracy of the approach along with building the technical capability in seismic processing. The accuracy of the module has been tested by both synthetic and real seismic field data; the efficiency and the accuracy of the model have been proven in terms of development method as well as field data application.

Key words: Seismic signal processing, seismic reflection, ray tracing, velocity modelling, seismic tomography, tomographic inversion.

1. Introduction

Velocity model is one of the most important features extracted from the seismic reflection data as it has been used for many purposes such as depth imaging, time-depth conversion and geomechanical model building. The resolution of velocity model building is highly dependent on the complexity of the method to be used and the resolution of the initial model and seismic data. For example, the velocity analysis is the simplest and fastest way to create the velocity model, however, the resolution of this method is poor in both lateral and time directions as the distance between two picking common depth points (CDP) is much higher than the one between two initial CDP intervals. Similarly, within a CDP semblance spectrum for velocity picking, the picking time interval is much higher than the time sampling rate. Full waveform inversion (FWI), in the reverse way, gives the velocity model the highest resolution and accuracy. However, the computational

cost is too high to be used widely in the seismic reflection industry. To reach the balance between the accuracy and computational cost, the seismic reflection tomography (SeisT) approach is an alternative method for getting the velocity model for migration purposes and to be used as the initial model for FWI problem, which produces a higher resolution than SeisT.

Tomography is an inversion process that provides a tool for velocity estimations from multichannel seismic reflection data. Tomography can be performed either in the prior-migration domain or in the post-migration domain. In each of these domains, we can access two types of information: kinematic (travel time) and dynamic (amplitude and phase) [1]. Thus, we have at least four ways to sort the tomographic inverse problem out. Table 1 gives a summary of the approaches used for velocity estimation.

During this work, we demonstrate a study of ray-based reflection travel time tomography applied for synthetic and field velocity models. The workflow of this approach is shown in Figure 1. There are several reasons why we chose this kind of approach for studying velocity



Date of receipt: 19/3/2021. Date of review and editing: 19/3 - 23/4/2021.
Date of approval: 7/10/2021.

Table 1. Types and domains of tomography for velocity estimation [1]

	Prior-migration domain	Post-migration domain
Ray-based (kinematic)	Reflection travel-time tomography Cross-well transmission tomography Refraction tomography	Pre-stack time migration tomography Pre-stack depth migration tomography
Waveform-based (dynamic)	Full waveform inversion (also known as waveform tomography, wave equation tomography, and diffraction tomography)	Wave-equation migration velocity analysis (WEM-VA) Wavepath tomography

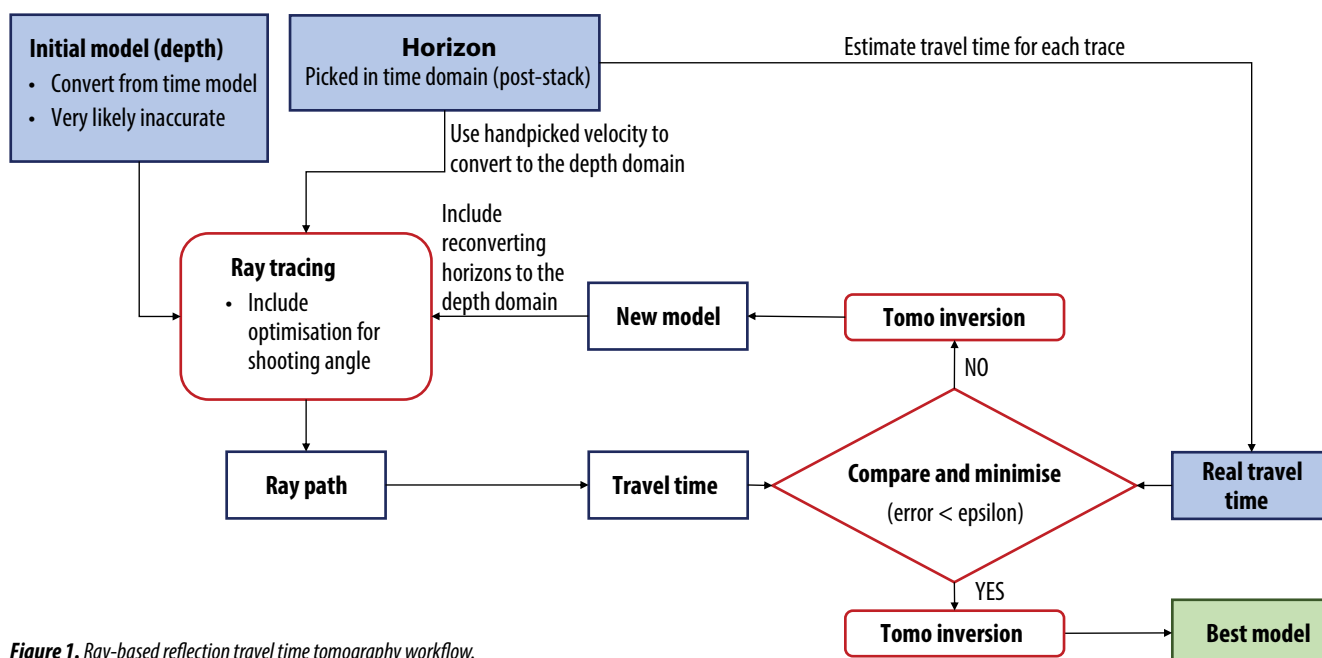


Figure 1. Ray-based reflection travel time tomography workflow.

estimation. Firstly, there is more physical information contained in the prior-migration domain than in the post-migration domain, where data has been migrated by using a not-optimised velocity model. Secondly, although waveform-based tomography can create a highly detailed velocity model, it demands a large computational cost. The ray-based method produces a velocity model of less resolution but still has the advantage of “robustness” (good quality), when carefully implemented [2].

2. Theoretical background

Like many other geophysical inverse problems, the ray-based reflection travel-time tomography consists of two basic steps:

- Determine a set of seismic reflectors and estimated travel times for various source-receiver positions based on the Eikonal equation’s solution.
- Iteratively update the velocity model by minimising the difference between calculated travel time and observation travel time. In this algorithm, the conjugate

gradient method is adopted to build a best-fit velocity model by iteratively comparing estimated travel times with the observed travel time for a given set of horizons.

2.1. Seismic ray tracing formulation and its numerical solution

In this step, the procedure of estimating travel times is performed by Runge-Kutta ray tracing technique in depth domain. Hence, for real data, all input objects of ray tracing procedure, including starting model and seismic horizons, must be converted from time to depth domain. In case of synthetic data, converting is not required because the velocity model is already in depth domain and all reflectors will be hand-picked on this model.

Ray tracing is a method for estimating the ray path through a media of varying propagation velocity, absorption characteristics, and reflecting surfaces. Under these circumstances, the ray path may bend, change direction, or reflect off surfaces, thus complicating analysis.

The ray trajectories are found by solving a certain differential equation that can be derived from the wave equation as follows [3]:

$$\nabla^2 \psi - \frac{1}{v^2(\vec{x})} \frac{\partial^2 \psi}{\partial t^2} = 0 \tag{1}$$

Equation 1 has a solution assumed in the form:

$$\psi(\vec{x}, t) = A(\vec{x}) e^{2\pi i f(t - T(\vec{x}))} \tag{2}$$

where $A(\vec{x})$ and $T(\vec{x})$ are unknown functions describing amplitude and travel time that are expected to vary with position.

By substituting Equation 2 into Equation 1 and considering weak velocity gradients as well as high frequencies regardless of the velocity gradient, we achieve the following results:

$$[\vec{\nabla}T]^2 - \frac{1}{v(\vec{x})^2} = 0 \tag{3}$$

$$\frac{A}{2} \nabla^2 T + \vec{\nabla}A \cdot \vec{\nabla}T = 0 \tag{4}$$

Equation 4 is called the geometrical spreading equation because its solution can be shown to describe the flow of energy along a ray path.

Equation 3 is the non-linear, partial-differential equation called the eikonal equation. For high frequencies or small velocity variations, a solution to the eikonal equation gives accurate travel times through complex media [3]. Using the method of characteristics, we can transform this equation into a system of first-order ordinary differential equations (ODE) that can be solved by standard numerical methods

$$\begin{aligned} \frac{d\vec{x}}{dt} &= v^2(\vec{x}) \vec{p} \\ \frac{d\vec{p}}{dt} &= -\frac{\vec{\nabla}v(\vec{x})}{v(\vec{x})} \end{aligned} \tag{5}$$

where \vec{p} is slowness vector.

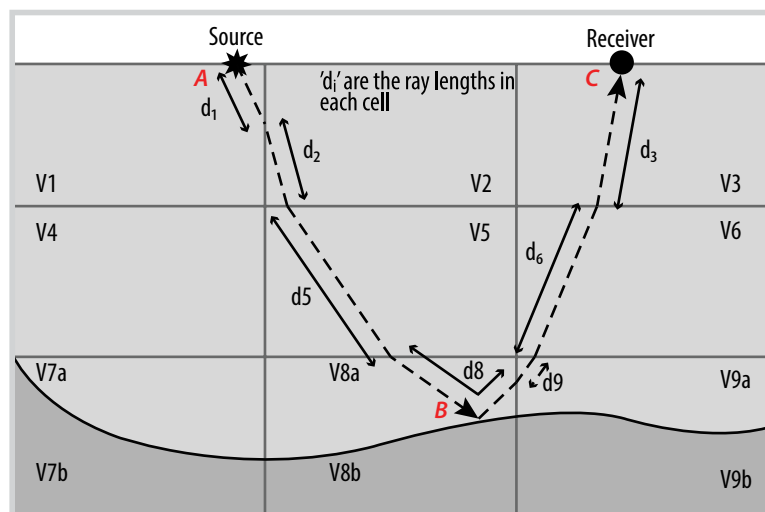


Figure 2. Graphical representation of ray tracing in velocity field [1].

Our study adopts the Runge-Kutta method to solve this ODE system [4].

The time step dt for solving the ODE system (Equation 5) must be chosen to be consistent with the velocity grid. If dt is too big, the velocity model will be updated sparsely, because the conjugate gradient method will edit only grids, where rays propagate through. If dt is too small, the number of tracing steps for a ray to reach its intended destination will be large and this will also lead to heavy computational cost. In our study, we apply an additional linear interpolation to ensure that every grid on the ray path is updated in the iterative procedure.

Our velocity field is discretised into samples for computational simulation. In this field, the ray trajectory is estimated repeatedly after every fixed time interval or step (Figure 2). At the end of each step, the current position of a tracing ray is updated and the values of the velocity and ray parameters at the nearest sample to this position are used to define the next position of the ray.

During simulated seismic acquisition, waves initiate at a shooting point (source) at or near the surface, propagate through the Earth's layers and may reach the receiving point (receiver), also at or near the surface, by reflection, refraction, or both. This complicated process can be described on a velocity model, as mentioned above, by using the Runge-Kutta ray tracing technique. Figure 1 shows the graphical representation of this model where simulated rays are reflected off the picked horizon and turn back to the surface. A distinctive feature of reflection tomography is that the ray will be reflected off a chosen horizon before arriving at the surface receiver. The calculation of the slowness vector of a reflected ray is demonstrated in Figure 3, where \vec{p}_1 is the incident ray's slowness and \vec{p}_2 is the reflected ray's slowness vectors. In the co-ordinate system Ogh at the reflection point on the horizon, the tangent opponent of the slowness vector is unchanged, while the normal opponent is changed in sign. Thus, components of the reflected slowness vector

are computed from those of the given incident slowness vector as follows:

$$\begin{aligned} pg_2 &= pg_1 \\ ph_2 &= -ph_1 \end{aligned} \quad (6)$$

where $pg_{1,2}$ and $ph_{1,2}$ denote as the incident ray and reflected ray slowness, respectively.

Additionally, the reflected rays as shown in Figure 2 could also travel in many other ways such as the turning ray that may never reach the intended reflector as in Figure 8. This is due to the total internal reflection at the shallower reflector (the incident angle is greater than the critical angle). Though the turning ray is also very useful for near surface tomography (such as building the velocity model for seismic land survey), it is not the target of this study.

A crucial issue for ray tracing is that for a particular pair of surface source-and-receiver, how do we determine the shooting angle for the ray from the source so that it could reach the intended receiver's location? If we shoot the ray by an arbitrary angle, it is likely not to reach the target receiver. Our solution for this issue is to use shooting angles determined by several methods. A simple way to try is to use a basic geometrical calculation as shown in Figure 4. Given the location of S and R (source and receiver) and the dip β of the reflector (near the location of CDP), the shooting angle can be computed by the formula:

$$\alpha = \gamma - \beta = \tan^{-1}\left(\frac{d}{2h}\right) - \beta \quad (7)$$

where d is the source-receiver offset and h is the depth of the projection point of the midpoint on the horizon.

As this ray tracing simulation was not utilised well for estimating an optimum shooting angle, the geometrically calculated value was used as an initial guess to optimise the procedure. Several optimisation algorithms such as bisection search, Gauss-Newton algorithm and the steepest descent method [4] have been tested, and we find out that the latter usually gives the best angle estimates for an acceptable number of iterations. In some

exceptional cases when the steepest descent does not work properly due to the local minimum convergence, the bisection search will be employed to reach the nearest possible point to the receiver position.

For far-offset-receivers on the same source record, we can apply the least-squares regression [4] to the set of near-offset shooting angles (already calculated/optimised) to arrive at a more accurate starting value for the steepest descent calculation of the current shooting angle. By this way, the number of steepest descent iterations will be much less than that in the case of using the geometrical initial angle estimation. In Table 2, we summarised the way to find out the optimum.

A particular notice during our experiments to improve optimisation convergence was that a smoothing filter would need to be applied to the velocity model and all horizons. Moreover, the speed and accuracy of the angle finding process are also enhanced significantly.

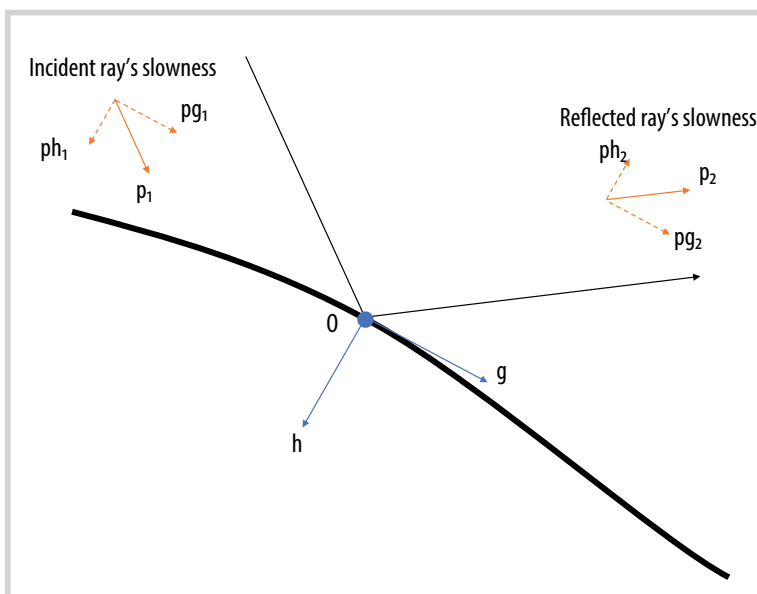


Figure 3. Recalculation of slowness vector at the point of reflection.

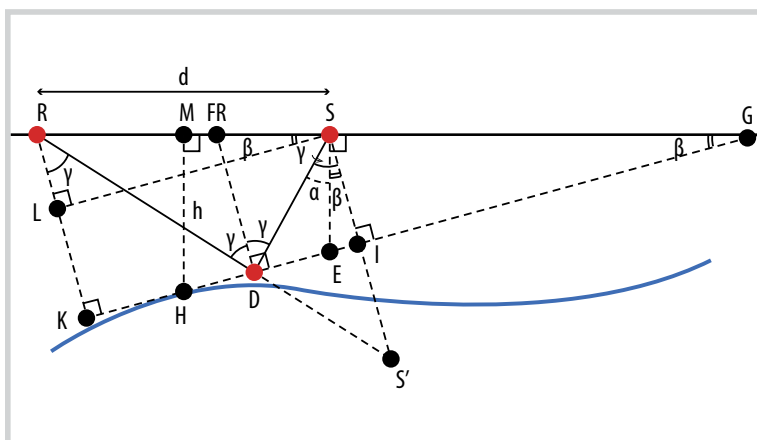


Figure 4. Geometrical representation of angle finding problem.

Table 2. Number of iterations of angle estimation procedure with acceptable error ±3 m around receiver's location

		Source's location (m)					Method to calculate initial guess for the steepest descent optimisation
		0	1,000	2,000	3,000	4,000	
Offset (m)	125	4	2	4	3	2	Geometrical
	137.5	2	3	3	2	2	
	150	0	1	2	1	0	
	162.5	0	1	1	1	0	Least-squares regression
	175	0	0	0	1	1	
	187.5	0	1	2	1	1	
	200	0	1	1	0	1	
	212.5	0	1	1	1	1	
	225	0	1	1	1	0	
237.5	1	1	1	1	1		

2.2. Inversion problem

If the velocity model is very deviated from the actual one, the errors between estimated travel times by the simulated ray tracing and their true values will be large. We thus need to minimise these errors using the optimisation routine by gradually adjusting the velocity model toward that goal. By this way, the estimated velocity model will gradually approach the actual one.

Consider the velocity model described earlier in Figure 2, which is divided into nine constant velocity cells, and a single ray reflecting off a horizon at point B, for a source at A and a receiver at C. The arrival time T_{ABC} for the ray path ABC is given by Equation 7 as:

$$T_{ABC} = \frac{d_1}{v_1} + \frac{d_2}{v_2} + \frac{d_5}{v_5} + \frac{d_8}{v_{8a}} + \frac{d_9}{v_{9a}} + \frac{d_6}{v_6} + \frac{d_3}{v_3} \quad (8)$$

Using many ray paths traversing the cells in the model, we can obtain a set of simultaneous equations (with measured travel time T and the unknowns are elements v_i of the velocity field). The task of solving those simultaneous equations (known as the tomography inversion) will result in the determination of the velocity distribution along such ray paths.

We have many arrival time measurements for a given sub-surface reflector element. Consider the five ray paths gathering shown in Figure 5, and the associated arrival times along the moveout trajectory (Figure 6). The travel time expression for these five ray paths can be written as:

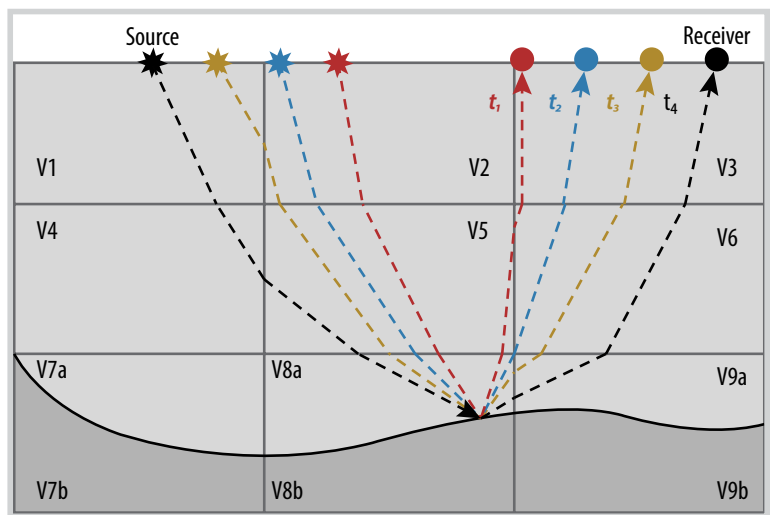


Figure 5. Input gathering in nine cell model (j=1,9) [1].

$$t_i = \sum_{j=1}^N \frac{d_{ij}}{v_j} = \sum_{j=1}^N d_{ij} s_j \quad (9)$$

Or, in matrix notation:

$$T = DS \quad (10)$$

where t_i is the total travel time along the i^{th} ray path;

d_{ij} is the path length in the j^{th} cell of the velocity model for i^{th} the ray;

v_j is the velocity in the j^{th} cell;

s_j is the slowness in the j^{th} cell, where we have N cells in the model (in this example, N = 9).

In Equation 10, T is a vector of two-way travel time measured for sound waves emanating from a source, propagating through the earth and reflecting off a horizon, then returning to an individual receiver. D is a matrix of path lengths that the ray paths have in each cell of the velocity model (Figure 2) [1]. The matrix D is determined in step 1 using ray tracing technique. S is a vector of velocity model and will be estimated numerically.

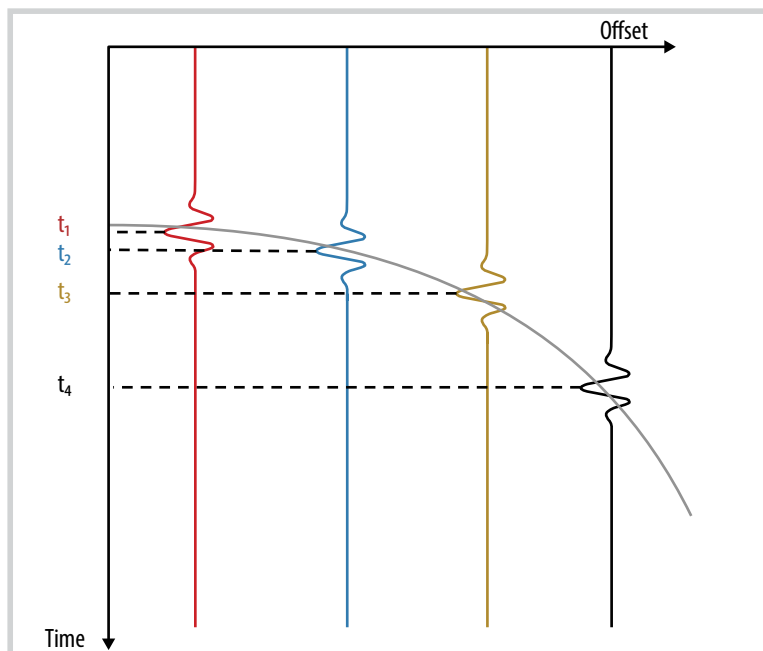


Figure 6. Moveout trajectory for a reflector: an autopicker will determine the t values ($i = 1, 4$) [1].

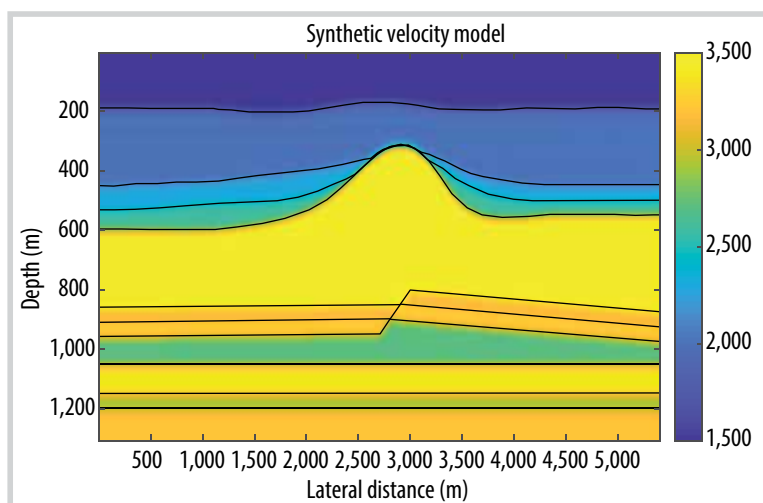


Figure 7. True velocity model with picked horizons (acoustic discontinuities).

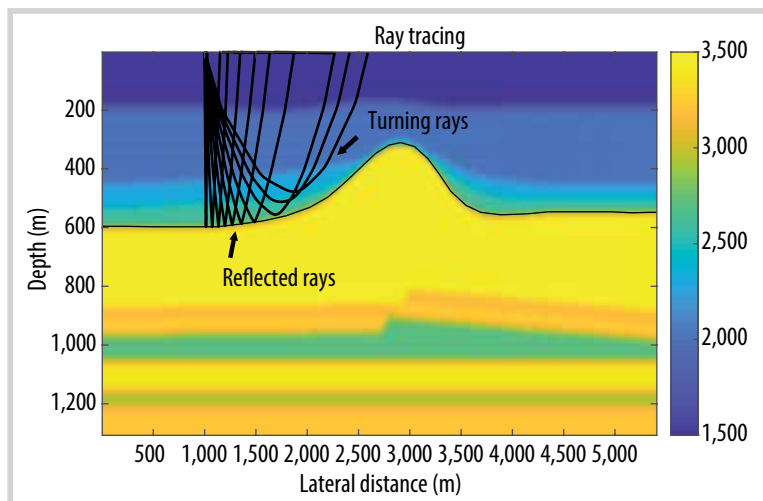


Figure 8. Ray tracing by Runge-Kutta method with a picked reflector.

To solve S in Equation 10, normally the least-squares method is applied. However, a better way is to use the conjugate gradient (CG) method due to the nature of faster computational complexity. CG is the most popular iterative method for solving large systems of linear equations like Equation 9 because CG has a time complexity of $O(m\sqrt{k})$, whereas the steepest descent has a time complexity of $O(mk)$. Both algorithms have a space complexity of $O(m)$, where k is the spectral condition number of matrix D , and m is the number of non-zero entries in the matrix [5]. Upon application of a few CG iterations, the velocity model is updated to an optimised model much closer to the actual one.

3. Synthetic data verification

A synthetic velocity model (Figure 7) is used to verify the effectiveness of the method. The model is created in depth domain and contains ten seismic reflectors with an anticline in the high velocity region. There is also a fault-like structure in the deeper region of the model, which is an interesting object for the tomographic inversion study.

The optimisation procedure is applied to our true velocity model to estimate the shooting angle for each source-receiver pair and obtain the true travel time information, which is then used as the reference, or input, of iterative procedure.

The acquisition geometry was defined by a system composed of 207 sources (with a source interval of 25 m) and 10 receivers for each source (with a receiver interval of 12.5 m); all were placed on the water surface. Calculated travel times of all source-receiver pairs are used as reference data in tomographic inverse procedure. The inversion adopts the simple and powerful conjugate gradient method as mentioned in section 2.2. We use a strong smooth version of the true velocity model as the initial model for this step. The results of tomographic inversion test are presented in Figure 9.

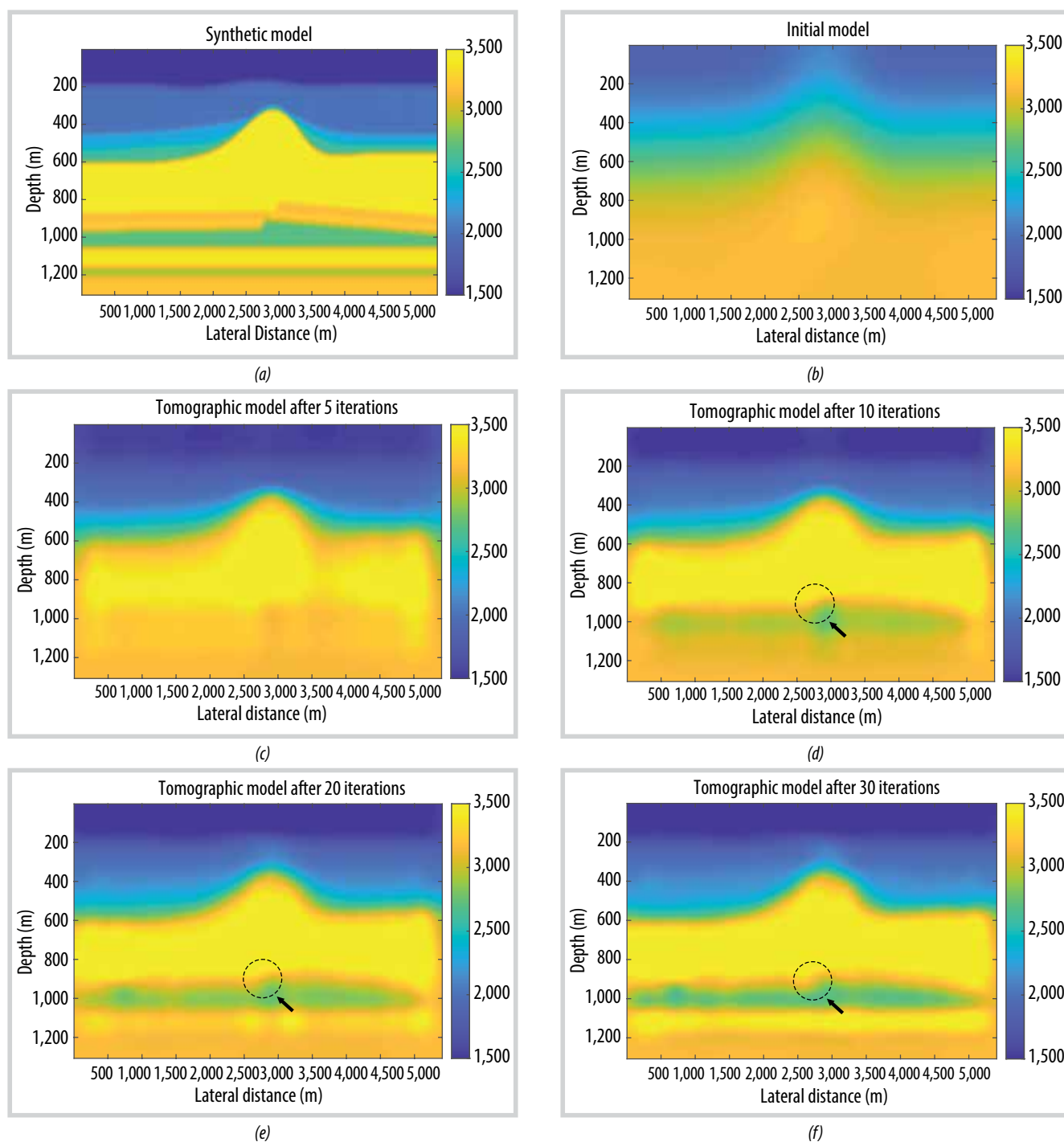


Figure 9. Results of tomographic inverse process. a) True velocity model; b) Initial model; c) Estimated tomographic model after 5 iterations; d) Estimated tomographic model after 10 iterations; e) Estimated tomographic model after 20 iterations; f) Estimated tomographic model after 30 iterations.

Table 3. Root-mean-square error of velocity models

Model	RMSE (m/s)	Average relative error of velocity model (%)
Initial model	370.6	18.15
Estimated model after 5 CG iterations	219.6	10.75
Estimated model after 10 CG iterations	176.4	8.65
Estimated model after 20 CG iterations	156.1	7.65
Estimated model after 30 CG iterations	152.9	7.5

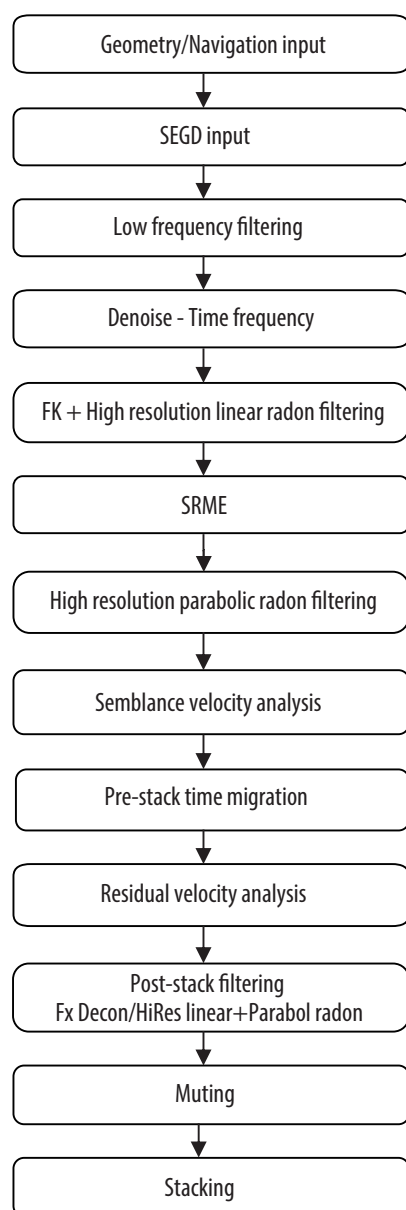


Figure 10. Basic processing steps.

The algorithm starts from an over-smoothed model (Figure 9b) without any clear seismic features, and eventually converges to a much more realistic result. Shallow zone and high velocity section are recovered after only 5 CG iterations. By increasing the number of CG iterations, deeper layers of velocity model are also inverted more and more accurately. As seen in Figure 9d, the interesting fault-like structure is quickly recovered after 10 iterations. The algorithm accuracy can be estimated by calculating the root-mean-square error (RMSE). The smaller the RMSE, the closer the fit of estimated model to the true data. The RMSEs are shown in Table 3.

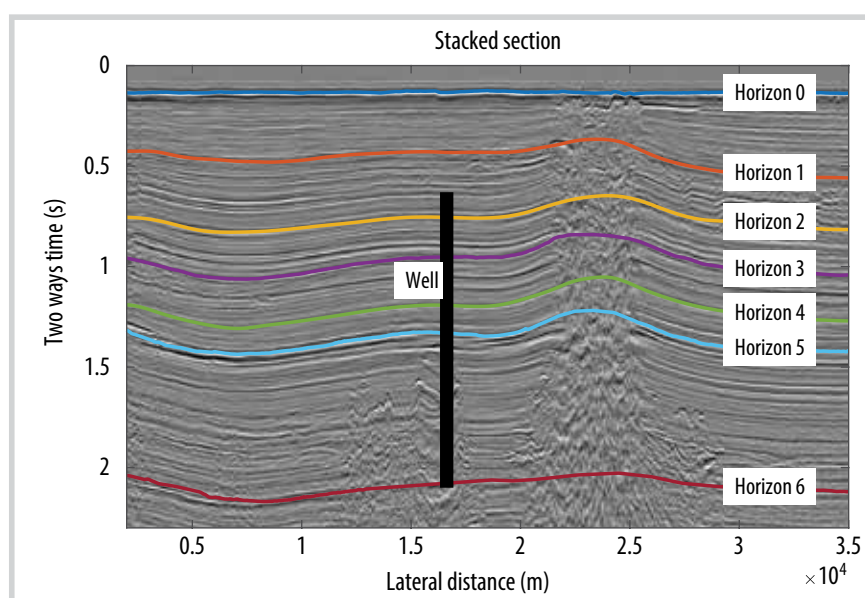


Figure 11. A seismic line used in the study with picked horizons and well location.

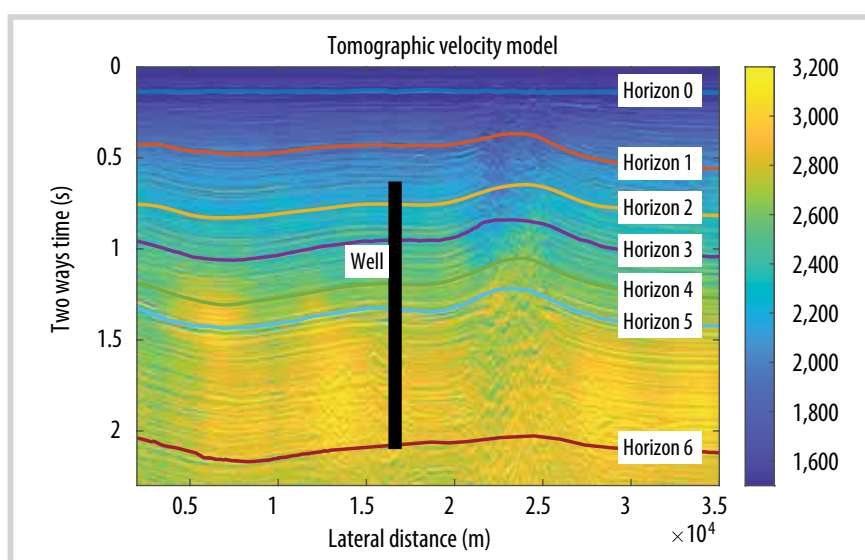


Figure 12. Tomographic velocity model overlaid with seismic data.

4. Field data application

We now present the application of our tomographic inverse algorithm to a 2D data set from a field offshore Vietnam. This data set is processed and interpreted by a geophysical team of the Vietnam Petroleum Institute (VPI). The basic processing steps are shown in Figure 10.

A distinct difference from the modelling case is that the data (velocity fields) in the synthetic modelling is already in the depth domain, while in the case of field application, the input data (seismic data, picked RMS velocity and picked horizons) is only in the time domain. Thus, there's a need to convert the input (picked horizons) from time to depth domain during the iterative procedure, which is

not at a true depth but a depth depending on the current velocity model. By minimising the travel time residual, we hope the depths also converge to the true solution. Thus, beside the CG iterations to improve the velocity model to perform ray tracing with the current seismic-depth-domain horizons, there will be an outer loop to update the velocity model in depth with the updated depth of the horizons (Figure 1). Other than that, the inversion proceeds similarly to the synthetic modelling case.

Figure 11 shows stacked data with picked horizons and well location. From the process of applying algorithms to synthetic data we found that the more horizons are picked, the better the result of tomographic inversion will be. However, using more horizons also means more computational cost, especially for field data, where the number of shot-receiver pairs is usually a lot. In this work, we picked 7 horizons, among which 3 located above, 1

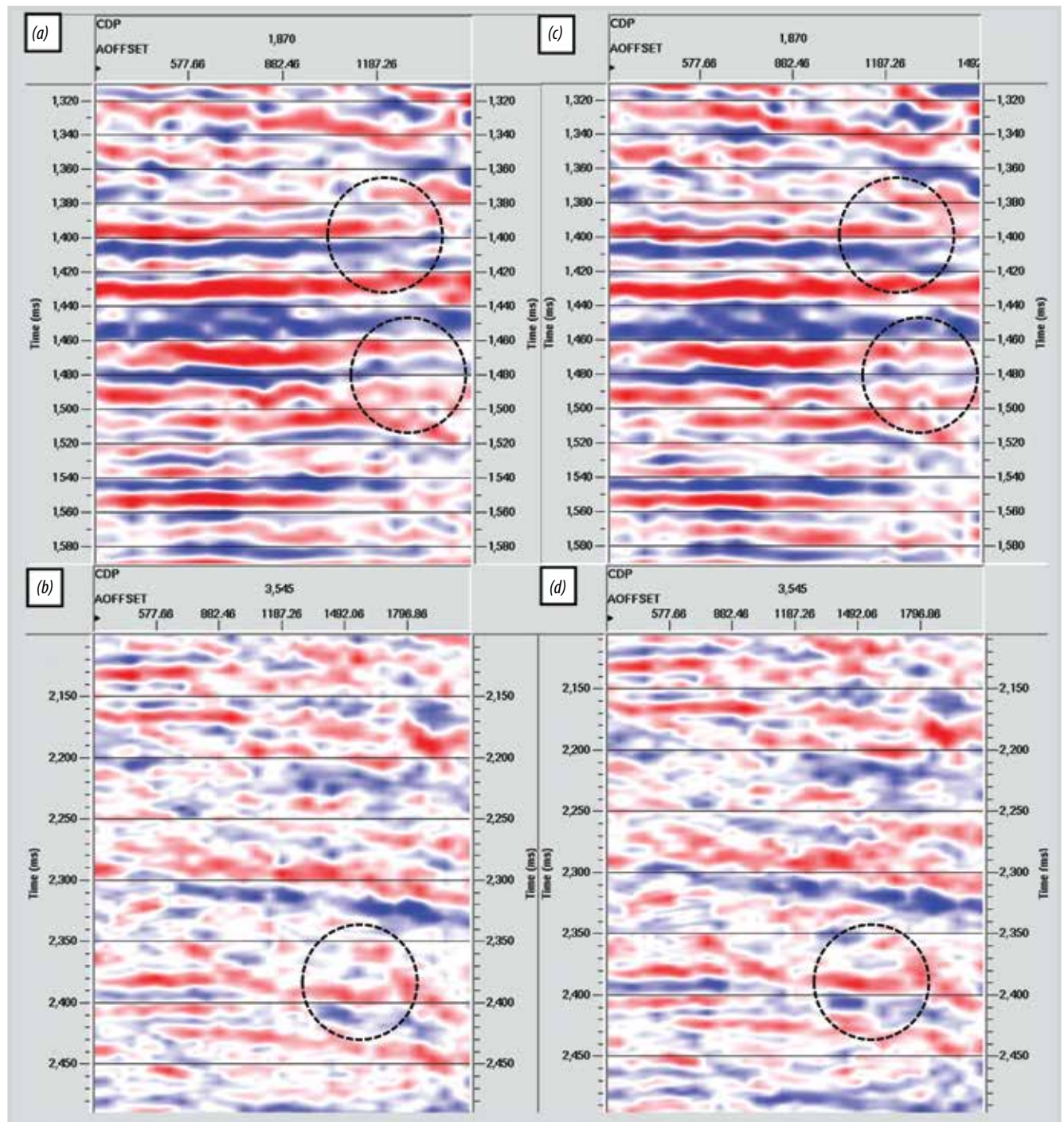


Figure 13. Comparison of CDP gatherings after PSTM with (a, b) handpicked velocity and (c, d) tomographic velocity.

located below and 3 went through the region with well measurement data.

Once the velocity model is inverted by SeisT, it will be overlaid by stack section; then the velocity change as well as anomaly possibly associated with hydrocarbon accumulation can be observed as in Figure 12. In this particular seismic line, the seismic velocity model has been successfully inverted by the proposed SeisT algorithm, and the velocity surrounding the well location (at the diapir),

where the gas was discovered, tends to be smaller than laterally surrounding area.

Unlike the case of synthetic model, for field data, we do not have an “absolutely” true velocity model to compare our tomographic results. So, we must try other ways to check if our algorithm works properly. In this work, we demonstrate two different methods for quality control (QC). One is using the estimated velocity model as the input for Kirchhoff Pre-Stack Time Migration (PSTM); its output is expected to contain flatten seismic events in the CDP gatherings (Figure 13). The other method is to compare the inverse model with the well data located nearby the studied line.

The average residuals of the estimated models are calculated as an additional verifying method. With the residual defined as the differences between the travel times estimated by the ray tracing method and the

Table 4. Average residual of velocity models

Model	Average travel time residual (ms)
Estimated model after 10 CG iterations	3.664
Estimated model after 20 CG iterations	3.147
Estimated model after 30 CG iterations	3.093
Estimated model after 50 CG iterations	3.033

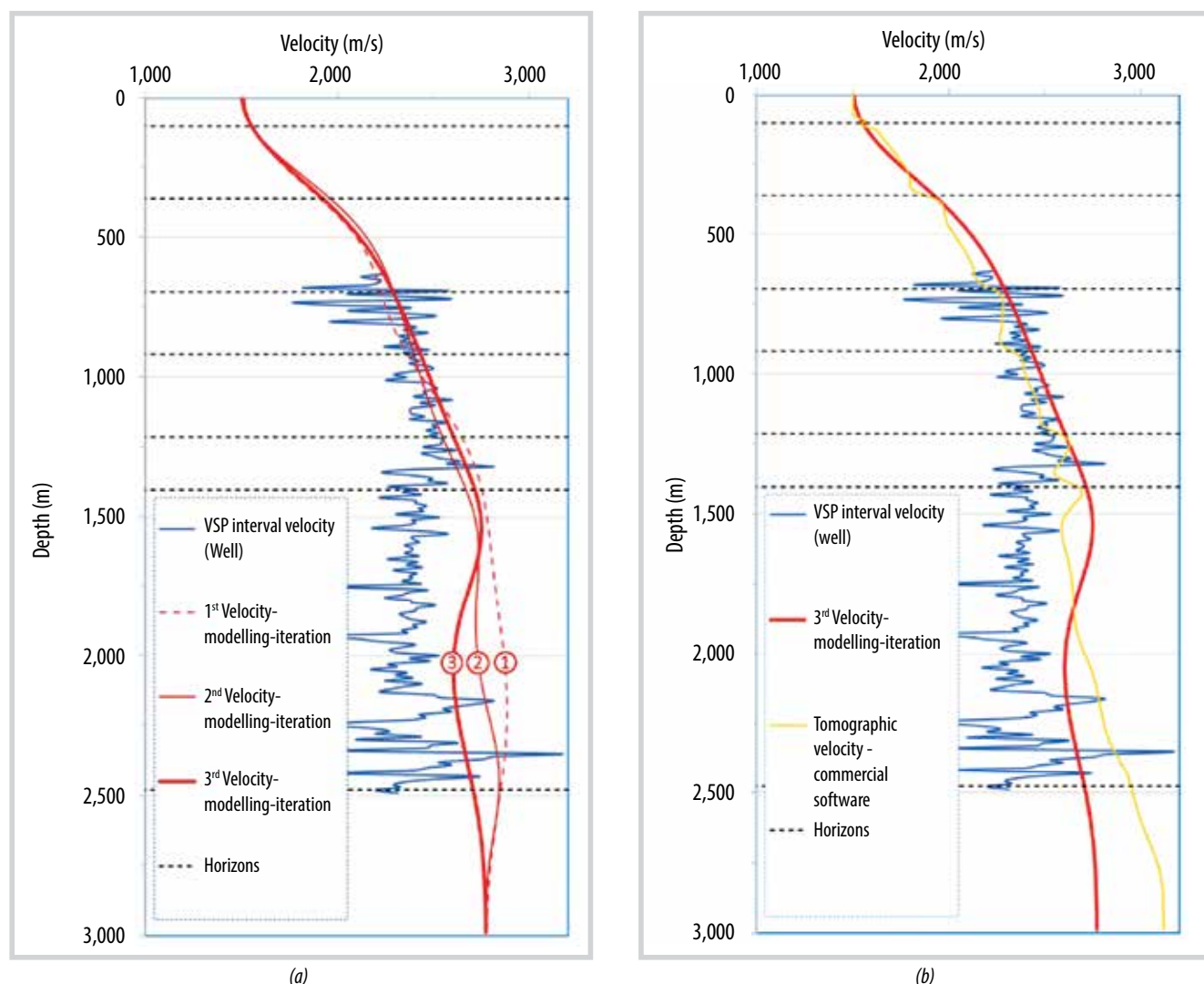


Figure 14. Comparison of tomographic velocity with (a) VSP velocity from well data and (b) commercial software.

true travel times (horizons picked), the average residuals after CG iterations are calculated and shown in Table 4.

We can see from Table 4 that, when CG iteration increases, the average residual of the estimated model decreases more and more slowly. This phenomenon can be explained by the fact that, as the average residual gets closer to the sampling interval, it should be much harder for the optimisation routine to improve the results.

The location of picked horizons in the depth domain is calculated using a picked velocity model. This means if the velocity model is updated by tomographic inversion, the horizons' location should also be recalculated. For this reason, we have made several velocity modelling iterations, in each of which the location of the horizons is

defined using the velocity model estimated in the previous one. The improvement of this iterative procedure is shown in Figure 14a.

An independent check of the tomographic inversion result can be achieved by comparing to VSP velocity measurement of a local well (Figure 14); the well location is indicated in Figure 11. The tomographic inverted velocity is slightly higher than well VSP velocity, so the result is encouraging. A tomographic inversion result using a commercial software is also displayed in Figure 14b. The commercial software model (based on the grid-tomo algorithm) is better than ours in terms of frequency content - a room for our future improvements. However, our algorithm gives a better matched velocity estimation with the VSP velocity in the slow-velocity-anomaly zone (1,500 - 2,500 m).

We would also like to investigate the effect of "well calibration" as often performed in the industry. Effectively, the velocity model used to convert the horizons from time to depth domain has

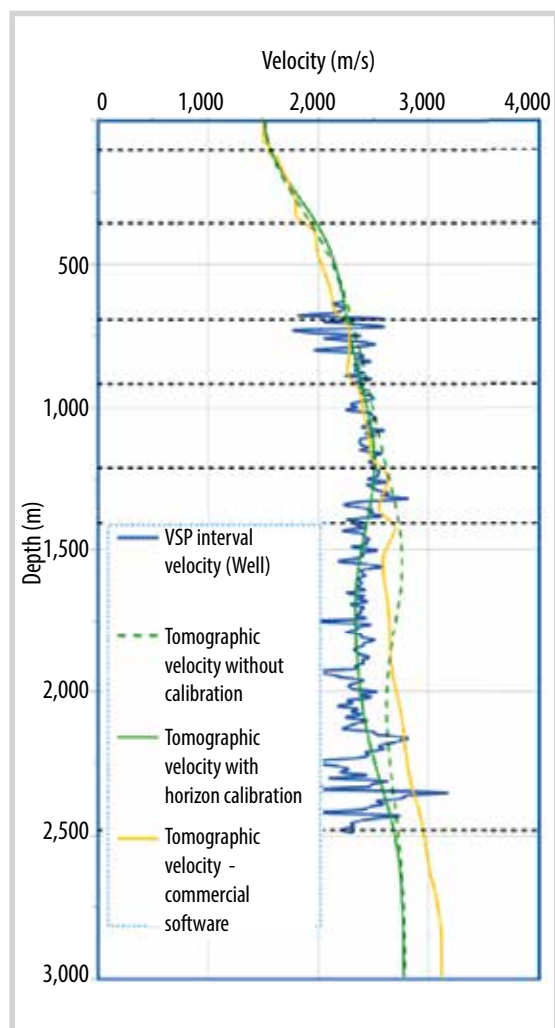


Figure 15. Comparison of tomographic velocity using well calibration with well data.

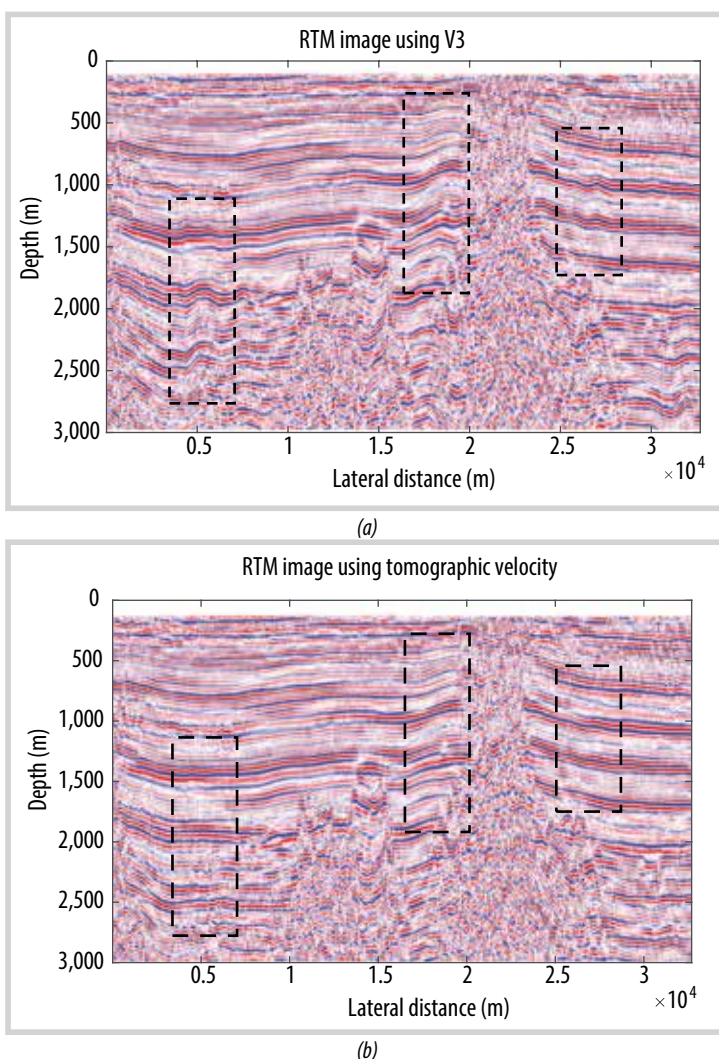


Figure 16. RTM images using (a) handpicked velocity V3 and (b) tomographic velocity.

been calibrated to get closer to the well VSP velocity (at the well the model is matched with well data). The final tomographic inversion velocity at the well matches closely with the low frequency component (i.e. the trend) of the VSP velocity (Figure 15).

5. Application of tomographic inversion results

As an application of the tomographic velocity results, we used the Reverse Time Migration (RTM) to perform seismic depth imaging which can (hopefully) illustrate the improvements of the tomographic inversion compared to the handpicked velocity model. As shown in Figure 16b, seismic events in RTM image using tomographic velocity contain less artifacts than those using the handpicked velocity model (V3) in Figure 16a. The result in Figure 16b is partly comparable to the Kirchhoff migration result (Figure 11).

6. Discussion

The accuracy of horizon picking plays a significant role in ray-based reflection travel time tomography since the picked horizons will act as the reference arrival times for the inversion process. These horizons (after being converted to the depth domain) are also used in the ray tracing procedure, where arrival time of a particular source-receiver pair is estimated for the current version of the velocity model. This estimated arrival time is then compared to the reference one to optimise our velocity model. Thus, the quality of the ray-based reflection travel time tomography depends much on the quality of horizon picking, which is now performed manually. One way to improve the quality of horizon picking is to use auto-picking functions of software such as Kingdom, Landmark, and Petrel, etc. A more advanced auto-picking version can be obtained from PaleoScan software [6], which can simultaneously pick many horizons in a chronological order. Auto-picking can improve not only the quality but also the quantity of horizon picking in an efficiently short amount of time.

In the case where seismic reflectors are not evident such as in the zone of basement or salt/mud diapirs, seismic reflection travel time tomography might hit troubles. Therefore, a different approach must be considered, such as "common focus point (CFP) tomography" [7] or diffraction-based tomography [8].

During the implementation of the tomography algorithm, it is noted that, the system of equations in

(Equation 9) can only be solvable (in the least-squares sense) if the number of equations is greater than the number of unknowns. In general, the number of equations is equal to the number of source-receiver pairs times the number of horizons; and the number of unknowns equals to the number of grids in the velocity model. If the above condition is not satisfied (which is usually the case), additional constraints must be applied to solve this system of equations. A common constraint is using the smoothing filter to correlate nearby points. Other techniques such as constraint by "dip/azimuth" or "shaping regularisation" [9] can be considered too. Even with constraints, a non-uniqueness condition for the solution is possible and an accurate initial velocity model will be an important factor that strongly affects the quality of the final optimised model. An accurate initial model also greatly affects the speed of solving system (Equation 9) (less time to converge). For the field example, we use the smooth version of the hand-picked velocity (V3) as the initial model.

In general, the development of the reflection tomography technology by the VPI team has achieved several accomplishments:

- For the modelling data, the tomographic result has recovered some seismic characteristics in the original velocity model such as layering and fault features;
- In the field data application, the inverse tomographic velocity produces more flattened events on CDP gatherings than the hand-picked one after pre-stack migration;
- It can also be reliably used as the velocity model for the RTM module with improvement over artifacts, compared to the result using hand-picked velocity model.

However, there are still shortcomings such as the matching with the well data. The slight mismatch between the tomographic inversion and well VSP velocity could be attributed by (over-) smoothing of the velocity field, insufficient number of horizons, and/or the lack of modelling for other physical phenomenon modelling (anisotropy, Q effect...), which can be overcome partially by using the well calibration method.

7. Conclusions

In this work, the development of travel time reflection tomography technology at the VPI is demonstrated through synthetic and field results. Many issues faced by

the team during the study and development of ray-based reflection travel time tomography have been discussed. We indicate that the quality of final tomographic results depends on many factors, especially the accuracy of the initial velocity model and the quality of horizon picking. We can reach further improvements by considering other constraint techniques (smoothing) and/or modelling more complicated physically, such as modelling Q and/or anisotropy effect. Although in this iteration of the technology, a basic tomographic inversion software and workflow are developed, its completion has highlighted some important insight of the process, including:

- The necessary algorithm, software module, and workflow for understanding the core techniques (ray tracing, optimisation, inversion) used in the tomographic inversion;
- The implementation of reflection tomography method to invert a better acoustic velocity model (compared to the normal handpick flow).

The basic model will need further development including more complicated physical models, such as Q, anisotropic tomography. More advanced versions of velocity model building such as 3D tomography or full waveform inversion are also among the future goals.

Acknowledgements

We would like to thank the Vietnam Petroleum Institute (VPI) for the support given to the development of the travel time reflection tomography technology.

References

[1] Ian F. Jones, *An introduction to: Velocity model building*. EAGE, 2010.

[2] R.G. Pratt, F. Gao, C. Zelt, and A. Levander, "A comparison of Ray-Based and Waveform Tomography - Implications for migration", *64th EAGE Conference & Exhibition*, 2002. DOI: 0.3997/2214-4609-pdb.5.B023.

[3] Gary F. Margrave, "Raytracing for inhomogeneous media", *Numerical Methods of Exploration Seismology with Algorithms in MATLAB*. The University of Calgary, 2003, pp. 105 - 112.

[4] Steven C. Chapra and Raymond P. Canale, *Numerical methods for engineers*. McGraw-Hill Education, 2015.

[5] Jonathan Richard Shewchuk, *An introduction to the conjugate gradient method without the agonizing pain*. School of Computer Science Carnegie Mellon University, 1994.

[6] Eliis, "PaleoScan software". [Online]. Available: <https://www.eliis-geo.com/paleoscan-overview-a.html>.

[7] B.E. Cox and D.J. Verschuur, "Tomographic inversion of focusing operators", *63rd EAGE Conference & Exhibition, Netherlands, 11 - 15 June 2001*. DOI: 10.3997/2214-4609-pdb.15.M-35.

[8] Mahasweta Mahapatra and Samiran Mahapatra, "Seismic diffraction tomography technique using very fast simulated annealing", *Journal of Applied Geophysics*, Vol. 67, No. 2, pp. 125 - 129, 2009. DOI: 10.1016/j.jappgeo.2008.10.004.

[9] Sergey Fomel, "Shaping regularization in geophysical estimation problems", *Geophysics*, Vol. 72, No. 2, 2007. DOI: 10.1190/1.2433716.

A PRACTICAL METHOD FOR PLANNING LARGE NUMBER OF HORIZONTAL WELLS WITH A RESERVOIR MODEL FOR A FIELD DEVELOPMENT PLAN

Guido Fava¹, Dinh Viet Anh²

¹Schlumberger

²Petrovietnam Exploration Production Corporation

Email: anhdv@pvep.com.vn

<https://doi.org/10.47800/PVJ.2021.10-02>

Summary

The most advanced technique to evaluate different solutions proposed for a field development plan consists of building a numerical model to simulate the production performance of each alternative. Fields covering hundreds of square kilometres frequently require a large number of wells. There are studies and software concerning optimal planning of vertical wells for the development of a field. However, only few studies cover planning of a large number of horizontal wells seeking full population on a regular pattern.

One of the criteria for horizontal well planning is selecting the well positions that have the best reservoir properties and certain standoffs from oil/water contact. The wells are then ranked according to their performances. Other criteria include the geometry and spacing of the wells. Placing hundreds of well individually according to these criteria is highly time consuming and can become impossible under time restraints. A method for planning a large number of horizontal wells in a regular pattern in a simulation model significantly reduces the time required for a reservoir production forecast using simulation software. The proposed method is implemented by a computer script and takes into account not only the aforementioned criteria, but also new well requirements concerning existing wells, development area boundaries, and reservoir geological structure features.

Some of the conclusions drawn from a study on this method are (1) the new method saves a significant amount of working hours and avoids human errors, especially when many development scenarios need to be considered; (2) a large reservoir with hundreds of wells may have infinite possible solutions, and this approach has the aim of giving the most significant one; and (3) a horizontal well planning module would be a useful tool for commercial simulation software to ease engineers' tasks.

Key words: Asset and portfolio management, field development optimisation and planning, water saturation, reservoir simulation, directional drilling.

1. Introduction

The designs of development plans for oil and gas fields are based on the definition of a drilling schedule. Development wells are drilled to (a) reach and support a production plateau; (b) maximise the hydrocarbon recovery; and (c) provide injection for pressure support or secondary recovery.

The task addressed in this work is a full population of the field with as many horizontal wells as needed to get the maximum possible production rate and optimal desired production that is maintained for several years. This study should be distinguished from other studies available in the literature that are focused on production optimisation with a minimum number of well locations yielding a high recovery per well. The well population in this work is based on a regular pattern rather than selection of optimal random locations. The evaluation of every possible location on a regular pattern was found to be a frequent request from field operators because it suits their local and economic circumstances. Interference be-



Date of receipt: 30/9/2021. Date of review and editing: 30/9 - 7/10/2021.

Date of approval: 7/10/2021.

This article was presented at SPE Kuwait Oil and Gas Show and Conference and licensed by SPE (License ID: SPE-175169-MS) to the republish full paper in Petrovietnam Journal.

tween wells is implied in such conditions. Every location needs to be filtered against several restrictions, and the optimal vertical planning of the horizontal section needs to be defined. Doing this task individually for hundreds of wells is highly time consuming, thus unpractical, and can become impossible under time restraints.

This problem is solved by developing a programme that automates the subject task, issuing the simulator keywords with all the items needed for the section of a simulator data file referring to new wells position and production. In this study, a commercial black oil reservoir simulation software was used.

The next variable to be defined is the schedule on which each well is to be drilled. The programme contributes to this task by issuing a drilling queue. The output of the programme is but a starting point from which many locations will be depurated, and the drilling schedule may be optimised in subsequent simulation runs.

2. Literature review

There are a few software packages that can provide new well locations for field development plan. The best approach is performed by the Plan Opt module in the simulator. However, this application is specific for vertical wells. A guided decision software is another option, but it specifies not being accurate for horizontal wells.

There are a number of studies concerning finding well locations. These studies focus on a different goal though, which is to optimise the number of wells by carefully selecting the best locations. Hazlett and Babu [1] provide an analytic solution of Babu and Odeh [2] for horizontal well productivity that is used together with a search method to find optimal well locations. The solution of Babu and Odeh for horizontal wells in a box of homogeneous properties is generalised for heterogeneous media. This equation is useful for the computation of productivity index.

Cullick et al. [3] present a process for simultaneously determining many optimal locations for producing and injecting wells. The optimisation is performed by a software system that executes the reservoir simulator, an economic analysis, and the optimiser. A set of well targets is generated on a conventional reservoir model by ranking its properties.

In a study by Cottini-Loureiro and Araujo, the optimal well location is achieved by combining the methods of multiple realisation approach and quality map [4]. The

multiple realisation approach is based on identifying key parameters of the reservoir and modelling of the reservoir response for a combination of parameters. The quality map is a 2D representation of the quality of all the area of the reservoir in terms of production. It is generated by running a flow simulator multiple times, varying the position of a single well in each run until the entire grid is covered.

None of the papers found in the literature refers to a regular pattern development, which has been frequently requested by field operators because it is suitable for local and economic circumstances. Another issue is that previous studies generally propose the use of software that is not readily available.

3. Methodology

A step-by-step procedure of the proposed technique follows.

3.1. Oil column index map

The first criterion used to evaluate the well location spatially is the areal oil in place, volume of oil in place per unit surface, oil column index, or the $H_u \times \Phi \times S_o$ quantity. This number can be expressed in units of thickness or commonly in Rbo/acre through a conversion factor of 1 ft = 7757.4630 Rbo/acre.

There are several ways of evaluating this quantity depending on the software used for the geological model. In the example case, a script was written to calculate a map of $H_u \times \Phi \times S_o$ from the files of the simulation model because the geological model was not provided.

An oil column index map provides a view of the density of oil accumulation over all the area of the field. Best areas can be easily spotted so as to locate vertical or horizontal wells assuming that the vertical permeability is good enough to drain each sector of the field with a single horizontal branch.

In the case that the reservoir is divided totally or partially in the vertical direction by horizontal intercalations or barriers, $H_u \times \Phi \times S_o$ needs to be calculated for each division. Also, each of those divisions will be processed by the well location programme.

3.2. Programme input and output

The developed programme locates as many horizontal wells as possible in a field, on the basis of a regular rect-

angular pattern. The total oil in place for the drainage area of each location is added and compared with a minimum value. Locations under the minimum mean theoretically nonproductive wells and are discarded, together with those falling in restricted areas and other obstacles. Finding the maximum possible number of wells has the objective of achieving the maximum production and supporting it during a number of years.

Within each location, the well position is vertically optimised, i.e., the well will be connected to the layer that gives the higher productivity index and respects a minimum standoff from the water level.

As every potential location is covered with the regular pattern, the additional information provided by the programme is the order in which the wells will be drilled. The input and output are referred to the commercial simulator model.

- Input data
- + Grid dimensions;
- + Grid file (geometry);
- + Properties;
- + Sizes of rectangular pattern (drainage area);
- + Length of horizontal well;
- + Orientation of the wells (X or Y);
- + Co-ordinates I, J, K of existing well connections;
- + Co-ordinates I, J, K of obstacles or forbidden locations;
- + Co-ordinates I, J, K of development area;
- + Map of Rbo/acre (bi dimensional grid).

Keywords are those corresponding to the specific simulator.

The dimensions of the rectangular pattern are usually established based on the field operator's policy on minimum spacing and drainage area. If this is not the case, an initial value can be given by experience in similar fields. The length of the horizontal well is a matter of drilling feasibility.

The orientation of the wells, along the X or Y axis in this programme, is a parameter that has to be chosen according to the main flow direction of the reservoir. In isotropic reservoirs, it will be a sensitivity parameter. Sensitivity can also be run on drainage area and horizontal length.

- Output data

This information is for new wells in a format suitable for the reservoir simulation software's Schedule section:

- + Wellhead specification;
- + Well connections;
- + Well production control;
- + Drilling order.

Keywords are those corresponding to the specific simulator.

3.3. Processing the results

Once the output of the programme is obtained, the keywords are added to the Schedule section of the model, and a forecast is run. A field or group target is imposed.

The new wells are all closed in the well completion data keyword, and they will be opened to production as soon as the field cannot meet its target in the order they are listed on the drilling queue list. The main results of such run are:

- Achievement of target rate;
- Duration of production plateau;
- Increment of oil cumulative for the field in the forecasted period;
- Number of wells with effective production.

3.4. Result evaluation

The conditions for which the wells were located in the original pattern may have changed by the moment many of them are opened because of the water influx and other fluid movement. The arrays S_w and $H_u \times \Phi \times S_o$ can be calculated at a later time (i.e., when the main regions of the reservoir are flooded), and the programme will be run again.

In this case, besides using the mentioned arrays as input, the new located wells that are considered good in Step 3 are included in the existing well list. The purpose of this additional run is to correct the vertical location of wells that can perform better if drilled higher at later time.

This step may not be necessary in fields where saturation change is not important. On the other extreme, this step can be performed more than once.

3.5. Test runs

Repeating Step 3 with a smaller number of wells can significantly modify the production of the wells that are kept. Successive runs of Step 3, and eventually Step 4, will define which wells are required to achieve the targets for field development.

3.6. Application and report

The wells defined in Step 5 can be used for forecasts at lower plateau targets, usually supporting the plateau production longer time.

4. Computer programme

The aim of the developed programme is to fully populate a field with horizontal wells following a regular rectangular pattern.

A defined surface of the field is totally covered, with exception of locations that fall into:

- Existing wells;
- Non-productive areas;
- Obstacles such as faults;
- Areas restricted by administrative or other reasons.

This programme can be repeated with several alternatives, e.g. well orientation (X or Y), spacing, and horizontal length. From each output, a forecast can be run to find the maximum production and support it during a number of years.

It is not the objective of the programme to give the optimal solution for developing the field. As mentioned in the previous section, that solution can be found only by loading several alternative outputs from the programme into the simulation model and comparing the results.

The programme described is aimed and restricted to use with the referred commercial software grid and solution files as input. Also, the output from the programme consists of files that can directly be included in the Schedule section of the reservoir simulation software's data file. However, it is expected that the programme can be modified to be used for other reservoir simulators as well.

4.1. Programme input

The version of the programme that is ready to use has been developed for application on a specific field with a single characteristic: high-permeability channels driving water.

The user will prepare a text file containing the following information in free format. This file is called the well input file. An example of the well input file is provided in the Appendix. The data contained in that file are, line by line:

- I, J, K dimensions;
- Character string to fill each well completion data line after the K connections;
- Character string to fill each well production control line after the name of the well;
- Maximum and minimum I coordinates of development area; maximum and minimum J coordinates of development area; I and J sizes of rectangular drainage area; horizontal length; orientation code: 0 = X, 1 = Y;
- Characters of well name and initial number for wells;
- Character string to fill each WELSPECS line after the well coordinates.

From 7 to $(I_{\max} - I_{\min} + 7)$ is $J_{\min}(I)$, $J_{\max}(I)$. These lines define the area where the wells are allowed. The next lines are I, J coordinates of connections of existing wells and other obstacles.

Other files required as input are:

- Permeability input file contains the array as extracted from the grid file of the commercial simulator, which is an input of the reservoir model (this input is specific for this version of the programme, and is used to avoid locating wells in the high-permeability channels);
- Z co-ordinates file contains the array as extracted from the grid file of commercial simulator, which is an input for the reservoir model (this specific array specifies the depths for each one of eight corners of each cell in the model);
- Connate water saturation input file contains an array of connate water saturation; it can be exported from a postprocessor module once the reservoir model is initialised;
- Current water saturation input file contains an array of water saturation at the start time for the forecast; it can be exported from the postprocessor module once the reservoir model has been run to the end;
- Transmissibility data in X and Y directions contains an array of horizontal transmissibility in the direction normal to well orientation; it can be exported from the postprocessor module once the reservoir model is

initialised (this input is specific for this version of the programme, which assumes that the wells having the highest normal transmissibility will have the highest productivity index);

- Oil column index data-contains a 2D (I, J) array of the variable oil column index = $H_u \times \Phi \times S_o$ in Rbo/acre; this variable has been calculated by multiplying the porosity (Φ) of each cell by its net thickness (H_u) and its oil saturation (S_o), and for each I and J, the value of $H_u \times \Phi \times S_o$ for each cell has been added for all the column from $K = 1$ to K maximum (this can be made by means of a script in the postprocessor module or using a Fortran programme).

With all data files in the run directory, the programme can be run by opening the command window, positioning in the run directory, and typing HorWS, which is the name of the programme.

4.2. Programme workflow

The programme starts by reading the dimensions I, J, K of the model to allocate the input arrays. Once the arrays have the correspondent dimensions, the input files are read. The mobile water saturation for each cell is calculated as the difference between actual water saturation (S_{wat}) and critical water saturation (S_{wcr}). The location of the well inside each rectangular area of the pattern is defined symmetrically based on the sizes of area, well length, and orientation. As mentioned above, this version of the programme looks for the high-permeability channels, of approximately 100 D, connecting the aquifer with the crest of the reservoir. Such channels consist of cells where permeability is greater than or equal to 100 D and where this value is constant vertically from $K = 1$ to K maximum. Cells in this condition are detected, so wells are avoided on these channels and at a distance of 5 cells from them. In a more general version, this definition can be made outside the programme. Then, the co-ordinates of the channel cells can be included in the list of obstacles where drilling is forbidden.

The regular pattern is covered starting from the corner of the development area having the lowest I and J co-ordinates and proceeding along the J axis. Each location is filtered from obstacles (e.g. wells and channels). If there is an old well in the rectangular area of the location, then the programme goes to the next location. The summation of the oil column index is made for all the cells connected to the well; if it is zero, the location is discarded. This value will be used to classify the wells according to

the potential oil they can recover. To define the depth to drill the horizontal section of the well, the first criterion is to keep a standoff above mobile water. Starting from the uppermost layer and along the well length, the mobile water saturation is compared to a reference value of 0.15. All layers below the one having mobile water saturation greater than or equal to the reference are discarded for completion, plus two layers as a standoff from water level. This is under the assumption that mobile water saturation will increase monotonically downwards. From the uppermost layer filtered as described above up to Layer 1, the normal transmissibilities are added along the well length. Then, the well is completed in the layer having the highest transmissibility summation, as it is assumed that it will correspond to the highest productivity index. Note that the well is completed in a single layer, which can depart from horizontality. A minimum value of oil column index greater than zero can be used to filter the locations based on a statistical analysis of the Rbo/acre map.

4.3. Programme output

All the wells that pass the filters are recorded in three output files:

- Well specification file which contains the specifications for each new well;
- Completion data file which contains the well completion specification for every connection of new wells;
- Well control file which contains the well production control standard specifications for each new well; the wells are specified as shut, and they will be opened automatically to attain the production targets by using the drilling queue keyword that is added to the file as described below.

A subroutine is used to assign, from the array of corner Z co-ordinates, the eight corners corresponding to each connected cell. The corresponding depths are averaged, and the deepest connection is selected as representative for each well. At this point, every potential location is covered with the regular pattern. The next step is to classify the wells to assign the order in which each will be opened. The first criterion is that the lowest wells will be produced earlier so as not to leave oil behind the advancing water.

Another subroutine called ORDEM sorts the wells by their representative depth in descending order. This sorting is done by assigning to each well an order number

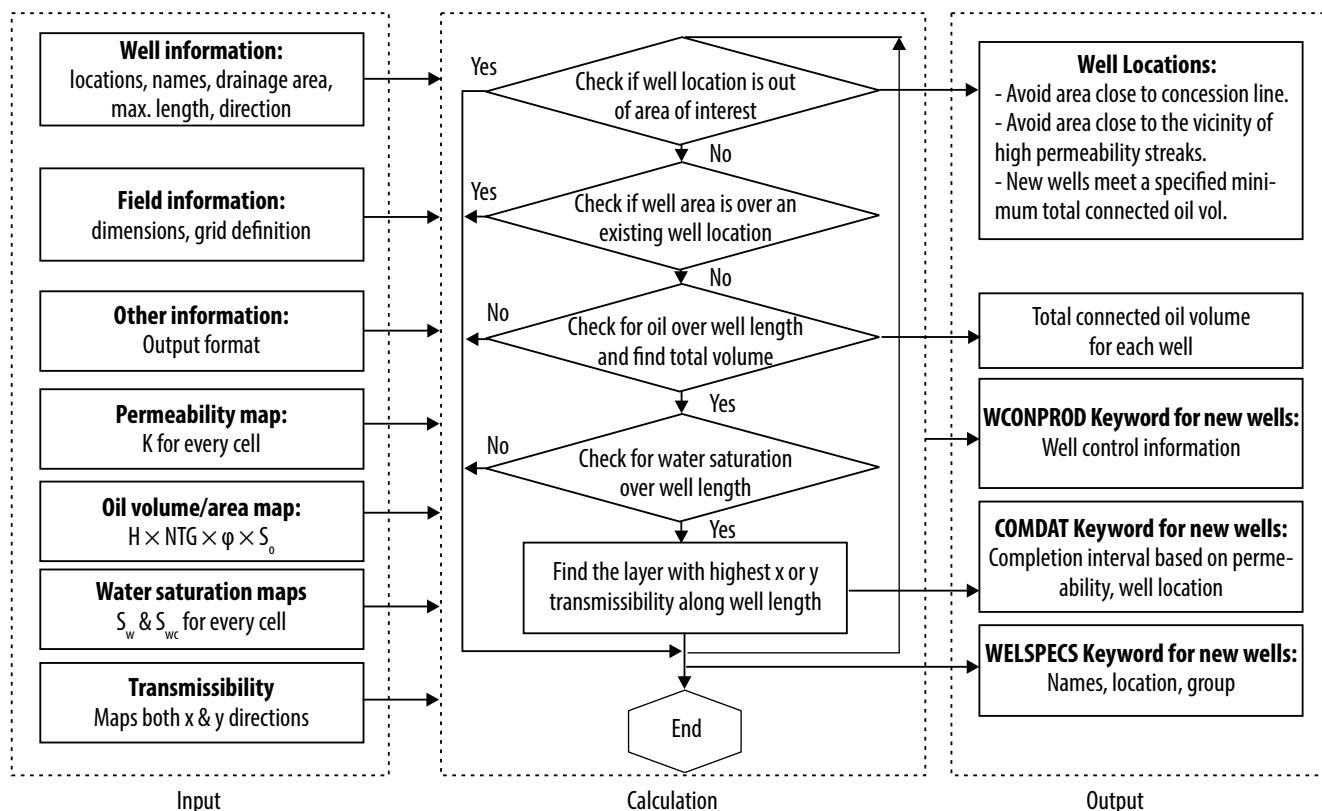


Figure 1. Workflow diagram for the well planning programme.

(vector NUM). The lowest well is assigned 1, and the highest well has the highest number.

The total number of wells is divided in three sets. Wells from each set are sorted according to their connected oil column index using the same subroutine. The keyword for drilling queue is added in the well control output file, and well names are added in the following order:

- Lower wells, sorted by decreasing oil column index;
- Medium wells, sorted by decreasing oil column index;
- Upper wells, sorted by decreasing oil column index.

The output files are then ready to be included in the simulator data file to make a forecast run. The method to make the best use of this programme consists of running it using different well spacing and orientations, then including the files from those alternatives in different data files and making the respective forecast runs. The opening queue can be modified by hand using the knowledge of facts outside the scope of this work.

Even after the wells have been selected through several filters, the result of the simulation runs will point out some wells with non-significant production that can be further discarded.

The auxiliary file screenoutput.txt is used to analyse the internal flow of the programme and can later be omitted. Figure 1 shows a workflow diagram of the programme.

5. Application example

5.1. Problem statement

Reservoir E-1 is a sample exercise represented by a 31 x 21 x 17 cells numerical model in the reservoir simulation software. The average horizontal block dimension is 120 x 120 m. There are multiple small sealing faults and shale zones scattered in the reservoir. Water aquifers are at the bottom and the edge of the reservoir. High-permeability streaks are also present in the reservoir with a permeability magnitude of 30 D. There are five existing wells, both vertical and horizontal. The goal is to plan as many horizontal wells as needed to effectively produce the field to its maximum potential. The number of horizontal wells required could be up to 300 depending on the production need and well configuration. Manually placing this large number of wells is a tedious task and may involve many human errors. It becomes impossible under a certain time constraint and when a sensitivity study (considering different well plan scenarios) is required. Thus, the method described above was used for planning new horizontal

wells in the field. The following criteria were considered for this example:

- New wells are placed 100 m away from the high-permeability streaks;
- Only wells that meet the minimum total connected oil volume are output;
- New wells are placed in the layers with the highest transmissibility along the well length and above the water level, which is defined by input data;
- Either wells along the X or Y direction can be considered;
- Output can be imported to the simulation software in form of the keywords for well specification, well production control, well completion, and drilling queue.

5.2. Results

Figure 2 shows the E-1 new wells on a schematic area map.

A useful tool in the analysis of this run is the plot of oil cumulative per well (Figure 3).

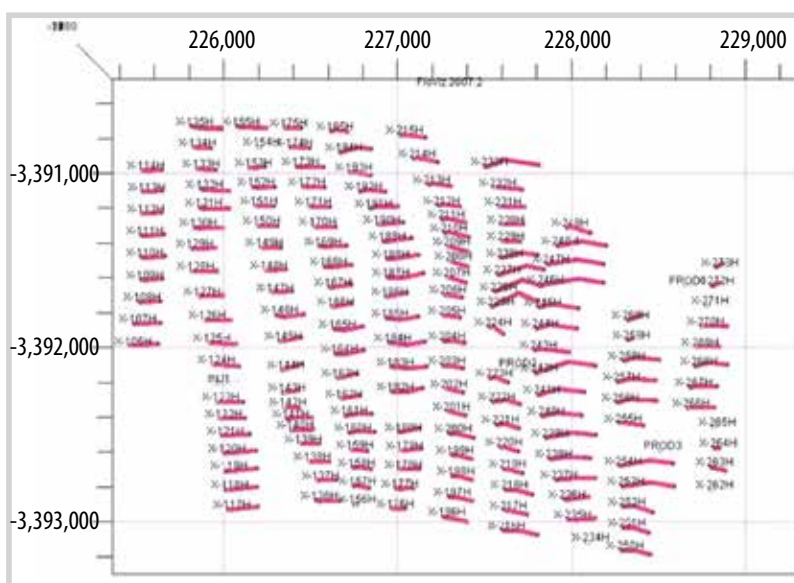
Note that from the more than 400 wells located, half of them have a non-significant cumulative and can be discarded. A criterion for discarding a well can be producing less than 3% of total field increment in cumulative.

Figure 4 shows the new wells on and oil column index map. All new wells are at good distance (100 m) away from the high-permeability streaks. Figure 5 is a cross section of an oil saturation map showing the completion interval of three wells. The wells are well above the high water saturation level. It should be noted that the programme also compared the transmissibilities of the layers above the water level and completed the well in the layer with the highest transmissibility.

6. Other cases

6.1. Horizontal well in the Y direction

In this case, the azimuth of the well



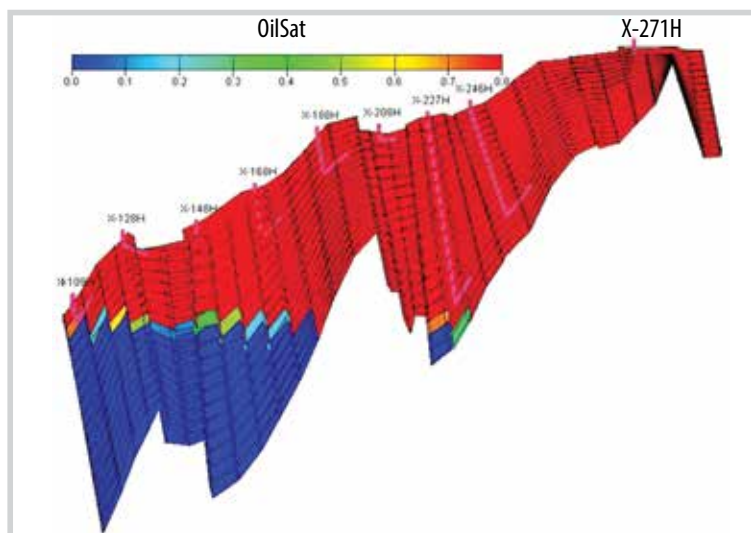


Figure 5. Cross section of oil saturation map showing the new wells for reservoir E-1.

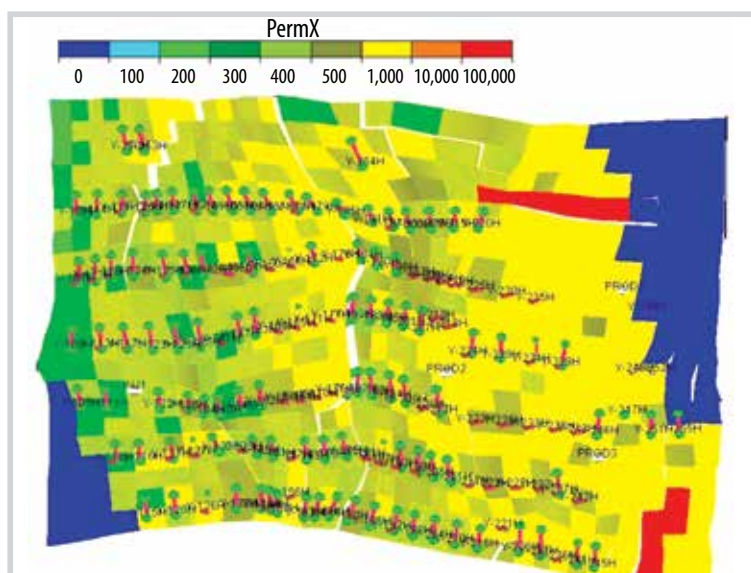


Figure 6. New horizontal well in the Y direction for reservoir E-1.

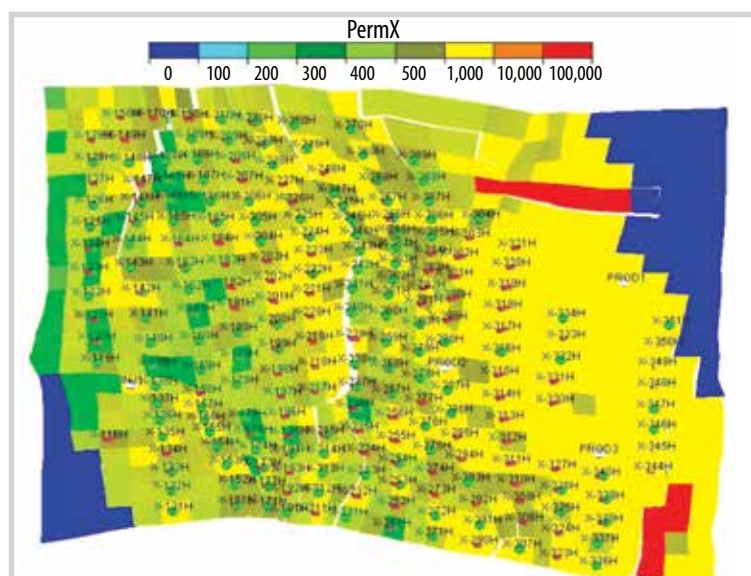


Figure 7. Permeability map showing the new wells with shorter length in reservoir E-1.

is in the Y direction instead of the X direction. The dimensions of the well drainage area were switched (the edge along the X axis is now along the Y axis and vice versa). Figure 6 shows the resultant new wells oriented along the Y directions in a permeability map. Similar to the case of new well in an X direction, all criteria were also met in this case.

6.2. Shorter well length

In this case, the maximum length of the new wells was set to be shorter than previous cases (reduced to 350 ft from 700 ft). The drainage area was reduced, and the new wells were closer to one another. Figure 7 shows the permeability map with the resulting wells.

7. Assumptions and limitations

The workflow described above is valid in the following assumptions and limitations:

- The cost of drilling wells has secondary incidence in the economy of the project. This is valid in present circumstances in many locations, as clients require placing a large number of wells to get high production even when interference will occur;
- The cells in the area where the wells will be planned are square and have homogeneous size;
- The thickness of all layers is similar in this area;
- The average thickness of two layers is a valid standoff from water;
- The horizontal transmissibility is defining the well's productivity index;
- The wells will follow the layers even if the layer has high dip;
- Mobile water saturation increases monotonically with depth;
- Each well will be able to drain all the volume contained in its drainage area, meaning horizontal barriers are irrelevant.

The theoretical calculation of the productivity index of a horizontal well is a complex problem which some authors (Hazlett and Babu [1],

Babu and Odeh [2]) have attempted to solve. The found correlations have given poor matches with the model results, so the transmissibility was adopted as a criterion instead of productivity index for the sake of simplicity.

8. Improvements and generalisation

The present version of the programme was created to meet the requirements of developing a specific field, but it can be applied to any case for which the given assumptions are valid. It still can be easily adapted for other cases.

However, there are some improvements, clearly foreseen while developing the programme, which are being worked out:

- Using a standoff given in depth, rather than a number of layers;
 - Calculating the productivity index of the well using the correlation of Babu and Odeh [2] or similar;
 - Using productivity index as a criterion for qualifying the wells rather than transmissibility;
 - Using productivity index to rank the wells in the opening queue;
 - Using all the volume of the well drainage area as a criterion for qualifying wells (assuming that the vertical barriers along the axis of the well are not continuous or significant);
 - Giving an alternative drilling order for the wells based on the number of available rigs and a logical path of the rigs along the field;
 - Detaching the module for defining the high-permeability channels as a separate programme;
 - Giving a special treatment to faults, as they can be considered obstacles for drilling.
- A further step will be to generalise the programme to cover cases where the above assumptions are not valid:
- Using geometric coordinates X, Y, Z rather than grid coordinates I, J, K;
 - Defining the wells as horizontal even in high dip layers (thus not following the layer);
 - Using any orientation for the wells besides those parallel to the X or Y axis;
 - Input from map files instead of simulator files;
 - Output in geometric co-ordinates X, Y, Z besides co-ordinates I, J, K.

9. Conclusions

The new method helps to save significant working hours and avoid human errors, especially when many development scenarios need to be considered. A large reservoir with hundreds of wells may have infinite possible solutions; this approach has the aim of giving the most significant. A horizontal well planning module would be a useful tool for commercial simulation software to ease engineers' tasks.

Nomenclature

H_u : Net thickness

S_o : Oil saturation

S_{wat} : Water saturation array

S_{wcr} : Critical water saturation array

Φ : Porosity

References

- [1] Randy D. Hazlett and D. Krishna Babu, "Optimal well placement in Heterogeneous reservoirs through semi-analytic modeling", *SPE Journal*, Vol. 10, No. 3, pp. 286 - 296, 2005. DOI: 10.2118/84281-PA.
- [2] D.K. Babu and A.S. Odeh, "Productivity of a horizontal well appendices A and B", *SPE Annual Technical Conference and Exhibition, Houston, Texas, 2 - 5 October 1988*. DOI: 10.2118/18334-MS.
- [3] A. Stan Cullick, Keshav Narayanan, and Sheldon Burt Gorell, "Optimal field development planning of well locations with reservoir uncertainty", *SPE Annual Technical Conference and Exhibition, Dallas, Texas, 9 - 12 October 2005*. DOI: 10.2118/96986-MS.
- [4] Alvaro Cottini Loureiro and Mariela G. Araujo Fresky, "Optimized well location by combination of multiple-realization approach and quality map methods", *SPE Annual Technical Conference and Exhibition, Dallas, Texas, 9 - 12 October 2005*. DOI: 10.2118/95413-MS.

SI Metric Conversion Factors

$$\text{bbl} \times 1.589873 \times 10^{-1} = \text{m}^3$$

$$\text{ft} \times 3.048 \times 10^{-1} \dagger = \text{m}$$

$$\text{ft}^3 \times 2.831685 \times 10^{-2} = \text{m}^3$$

$$\text{Stbo/Acre} \times 25451.2 = 1 \text{ m}$$

† Conversion factor is exact

APPENDIX

Programme Code

```

PROGRAM WellsNew7
  DIMENSION IPO(:, :), PERM(:, :, :), STBA
(:, :), SWC(:, :, :), SW09(:, :, :)
  DIMENSION DSW(:, :, :), TRAN(:, :, :), CH
ANL(:, :, :), IPO2(:, :, :)
  DIMENSION LIMJL(:), LIMJM(:)
  DIMENSION ZCORN(:)
  DIMENSION ZM(640), TRM(640), OIP(640)
  CHARACTER WEL*2,
COMPLET*64, GRU*5, SPEC*17, CONPROD*64
  INTEGER LC8(8), NE(640), NUM(640)
  N=1
  OPEN (1, FILE='Perm.txt', ERR=7)
  N=2
  OPEN (2, FILE='welinput.txt', ERR=7)
  N=3
  OPEN (3, FILE='compnew7.txt', ERR=7)
  PRINT *, N
  WRITE(10, *, ERR=8) N
  N=4
  OPEN (4, FILE='stboacre.inc', ERR=7)
  PRINT *, N
  WRITE(10, *, ERR=8) N
  N=5
  OPEN (5, FILE='wspecnew7.txt', ERR=7)
  PRINT *, N
  WRITE(10, *, ERR=8) N
  N=7
  OPEN (6, FILE='Swc.txt', ERR=7)
  PRINT *, N
  N=8
  OPEN (7, FILE='Sw09.txt', ERR=7)
  PRINT *, N
  N=9

```

```

OPEN (8, FILE='tran.txt', ERR=7)
PRINT *, N
N=10
OPEN (9, FILE='wconprod7.txt', ERR=7)
PRINT *, N
N=11
OPEN (10, FILE='screenoutput.
txt', ERR=7)
PRINT *, N
N=12
OPEN (11, FILE='zcorn.txt', ERR=7)
  * Dimensions of grid must be in in-
put file wel.txt. First line box.
  READ(2, *, END=8, ERR=7) IM, JM, KM
  PRINT *, IM, JM, KM
  WRITE(10, *, ERR=8) IM, JM, KM
  READ(2, 12, END=8, ERR=7) COMPLET
  PRINT *, COMPLET
  WRITE(10, *, ERR=8) COMPLET
  READ(2, 12, END=8, ERR=7) CONPROD
  PRINT *, CONPROD
  WRITE(10, *, ERR=8) COMPLET
  READ(2, *, END=8, ERR=7) IPMIN, IPMX, JP
MIN, JPMX, NCRI, NCRJ, LEN, NOR
  PRINT *, IPMIN, IPMX, JPMIN, JPMX, NCRI,
NCRJ, LEN, NOR
  WRITE(10, *, ERR=8) IPMIN, IPMX, JPMIN, J
PMX, NCRI, NCRJ, LEN, NOR
  READ(2, *, END=8, ERR=7) WEL, NEW, KMAX
  PRINT *, WEL, NEW
  WRITE(10, *, ERR=8) WEL, NEW
  READ(2, 28, END=8, ERR=7) GRU, SPEC
  PRINT *, GRU, SPEC
  WRITE(10, *, ERR=8) GRU, SPEC
  PRINT *, 'FILE WEL.TXT READ'
  WRITE(10, *, ERR=8) 'FILE WEL.TXT
READ'

```

```

* Define position of horizontal
well of length LEN in pattern NCRiXN-
CRJ
* Orientation of horizontal well X:
NOR=0; Y: NOR=1
* Co-ordinates of the well
IW=(NCRI-LEN*(1-NOR))/2
JW=(NCRJ-LEN*NOR)/2
* Co-ordinates of the well +
Length - 1
IWF=IW+(LEN-1)*(1-NOR)
JWF=JW+(LEN-1)*NOR
PRINT *,IW,IWF,JW,JWF
ALLOCATE (IPO(IM,JM),STAT=MALLOC)
IF(MALLOC.NE.0) PRINT *,'allocation
error in IPO'
ALLOCATE (IPO2(IM,JM),STAT=MALLOC)
IF(MALLOC.NE.0) PRINT *,'allocation
error in IPO2'
ALLOCATE (STBA(IM,JM),STAT=MALLOC)
IF(MALLOC.NE.0) PRINT *,'allocation
error in STBA'
ALLOCATE
(PERM(IM,JM,KM),STAT=MALLOC)
IF(MALLOC.NE.0) PRINT *,'allocation
error in PERM'
ALLOCATE (SWC(IM,JM,KM),STAT=MALLOC)
IF(MALLOC.NE.0) PRINT *,'allocation
error in SWC'
ALLOCATE
(SW09(IM,JM,KM),STAT=MALLOC)
IF(MALLOC.NE.0) PRINT *,'allocation
error in SW09'
ALLOCATE (DSW(IM,JM,KM),STAT=MALLOC)
IF(MALLOC.NE.0) PRINT *,'allocation
error in DSW'
ALLOCATE
(TRAN(IM,JM,KM),STAT=MALLOC)
IF(MALLOC.NE.0) PRINT *,'allocation

```

```

error in TRAN'
ALLOCATE (CHANL(IM,JM),STAT=MALLOC)
IF(MALLOC.NE.0) PRINT *,'allocation
error in CHANL'
ALLOCATE (LIMJL(IPMX),STAT=MALLOC)
IF(MALLOC.NE.0) PRINT *,'allocation
error in LIMJL'
ALLOCATE (LIMJM(IPMX),STAT=MALLOC)
IF(MALLOC.NE.0) PRINT *,'allocation
error in LIMJM'
IM1= IM+1
JM1=JM+1
MZCORN=8*IM*JM*KM
ALLOCATE (ZCORN(MZCORN),STAT=MALLOC)
IF(MALLOC.NE.0) PRINT *,'could not
allocate ZCORN'
READ(11,*,END=8,ERR=7) ZCORN
DO I=IPMIN,IPMX
READ(2,*,END=8,ERR=7)
LI,LIMJL(LI),LIMJM(LI)
END DO
DO J=1,JM
DO I=1,IM
CHANL(I,J)=0
IPO(I,J)=0
IPO2(I,J)=0
END DO
END DO
* Reads PERMsity array in input
PERM.txt. First line PERM
* READ(1,*,END=8,ERR=7) ABC
* PRINT *,ABC
READ(1,*,END=8,ERR=7) PERM
PRINT *,N
WRITE(10,*,ERR=8)N
PRINT *,PERM(6,6,8)
N=6

```

```

READ(4,*,END=8,ERR=7) STBA
PRINT *,N
WRITE(10,*,ERR=8)N
N=7
READ(6,*,END=8,ERR=7) SWC
N=8
PRINT *,N
WRITE(10,*,ERR=8)N
READ(7,*,END=8,ERR=7) SW09
N=9
PRINT *,N
WRITE(10,*,ERR=8)N
READ(8,*,END=8,ERR=7) TRAN
N=10
PRINT *,N
WRITE(10,*,ERR=8)N
DO K=1,KM
DO J=1,JM
DO I=1,IM
DSW(I,J,K)=SW09(I,J,K)-SWC(I,J,K)
END DO
END DO
END DO
PRINT *, 'DSW OF 1ST CELL', SW09(6,6
,6),SWC(6,6,6),DSW(6,6,6)
WRITE(10,*,ERR=8)'DSW OF 1ST
CELL',DSW(6,6,6)
* M1=0 index to start new line;
M1=1 to close a line
* Defining current well locations
DO L=1,5120
READ(2,*,END=45,ERR=7) IP, JP
IPO(IP,JP)=1
END DO
45 CONTINUE
* Defining region within.5 km of

```

```

high permeability channel
PRINT*, 'CHANNEL VALUE',CHANL(2,3)
WRITE(10,*,ERR=8)'CHANNEL
VALUE',CHANL(2,3)
DO IH=IPMIN,IPMX
DO JH=JPMIN,JPMX
CI=0
DO 30 KH=1,24
IF (PERM(IH,JH,KH).EQ.KMAX) THEN
CI=1
ELSE
CI=0
ENDIF
30 CONTINUE
IF (CI.EQ.1) THEN
CHANL(IH,JH)=1
ENDIF
ENDDO
ENDDO
PRINT*,CHANL(45,45)
IS=1
JS=1
IE=1
JE=1
DIST=5
DO 29 IH=IPMIN,IPMX
DO JH=JPMIN,JPMX
IF (CHANL(IH,JH).EQ.1) THEN
IF (IH.LT.(IPMIN+DIST)) THEN
IS=IH
ELSE
IS=IH-DIST
ENDIF
IF (JH.LT.(JPMIN+DIST)) THEN
JS=JH

```

```

ELSE
JS=JH-DIST
ENDIF
IF (IH.GT.(IPMX-DIST)) THEN
IE=IH
ELSE
IE=IH+DIST
ENDIF
IF (JH.GT.(JPMX-DIST)) THEN
JE=JH
ELSE
JE=JH+DIST
ENDIF
DO I=IS,IE
DO J=JS,JE
IPO2(I,J)=1
ENDDO
ENDDO
ENDIF
ENDDO
29 CONTINUE
DO I=1,IM
DO J=1,JM
WRITE(10,*,ERR=8)I,J,CHANL(I,J)
ENDDO
ENDDO
* DEFINING NEW WELL LOCATIONS
NWC=0
DO I=IPMIN,IPMX-NCRI,NCRI
DO J=LIMJL(I),LIMJM(I)-NCRJ,NCRJ
M1=0
K1=0
MAR=0
OP=0
I10=I+NCRI-1
J5=J+NCRJ-1
ZM(NWC+1)=0
* VERIFIES IF LOCATION IS OVER EX-
ISTING WELL
DO 32 IN=I,I10
DO 36 JN=J,J5
IF(IPO(IN,JN).EQ.1) THEN
GO TO 50
ENDIF
36 CONTINUE
32 CONTINUE
* SUMMATION OF OIL VOLUME OVER WELL
LENGTH
38 DO 40 IN=I+IW,I+IWF
DO JN=J+JW,J+JWF
OP=OP+STBA(IN,JN)
END DO
40 CONTINUE
IF(OP.EQ.0) THEN
GO TO 50
ENDIF
NEW=NEW+1
DO 132 IN=I,I10
DO 136 JN=J,J5
IF(IPO2(IN,JN).EQ.1) THEN
GO TO 50
ENDIF
136 CONTINUE
132 CONTINUE
* FINDING THE LOWEST LAYER ABOVE
LAYER WITH MAX. SW DIFFERENCE
K2=KM
KD=KM
DSWMAX=0.15
DO IN=I+IW,I+IWF
DO 41 JN=J+JW,J+JWF

```

```

DO K=1,KD
IF(DSW(IN,JN,K).GE.DSWMAX) THEN
IF(K.GT.2)THEN
K2=K-2
GO TO 41
ELSE
GO TO 50
ENDIF
ENDIF
ENDDO
41 CONTINUE
ENDDO
* FINDING THE LAYER WITH MAX. TRANS.
K3=K2
TRANMAX=0
DO 26 K=K2,1,-1
TRANTOT=0
DO IN=I+IW,I+IWF
DO JN=J+JW,J+JWF
TRANTOT=TRAN(IN,JN,K)+TRANTOT
ENDDO
ENDDO
IF(TRANTOT.GT.TRANMAX) THEN
TRANMAX=TRANTOT
K3=K
* PRINT *, 'TRANMAX', TRANMAX
ENDIF
26 CONTINUE
*WRITING OUTPUT TO FILES
IF(OP.GT.50000) THEN
TRANCOMP=0
SWCOMP=0
DO 22 IN=I+IW,I+IWF
DO 25 JN=J+JW,J+JWF
IF(STBA(IN,JN).GT.0) THEN
IF(TRANMAX.GT.0) THEN
IF(TRAN(IN,JN,K3).GT.0) THEN
TRANCOMP=TRAN(IN,JN,K3)
SWCOMP=SW09(IN,JN,K3)
WRITE(3,16,ERR=8)WEL,NEW,'H',IN,JN,
K3,K3,COMPLET,TRANCOMP,SWCOMP
M1=1
ENDIF
ENDIF
ENDIF
CALL ZMED(I,J,K3,IM,JM,LC8)
SZ=0
DO L=1,8
M=LC8(L)
SZ=SZ+ZCORN(M)
END DO
SZ=SZ/8
IF(SZ.GT.ZM(NWC+1)) THEN
ZM(NWC+1)=SZ
ENDIF
25 CONTINUE
22 CONTINUE
IF(M1.EQ.1) THEN
WRITE(5,20,ERR=8)WEL,NEW,'H',GRU,I+
IW,J+JW,SPEC,OP,TRANMAX
WRITE(9,13,ERR=8)WEL,NEW,'H',CONPRO
D,OP,TRANMAX,ZM(NWC+1)
NWC=NWC+1
NE(NWC)=NEW
NUM(NWC)=NWC
OIP(NWC)=OP
TRM(NWC)=TRANMAX
ENDIF
ENDIF
N=9
50 CONTINUE

```

```

END DO
END DO
WRITE(3,16,ERR=8) '/'
*Well classification by: 1) depth
2) OIP in three sets
ION=1
CALL ORDEM(ZM,NUM,ION,NWC)
WRITE(9,16,ERR=8) '/'
WRITE(9,*,ERR=8)'QDRILL'
M1=NWC/3
* Lower Wells
ION=1
CALL ORDEM(OIP,NUM,ION,M1)
DO L=ION,M1
NM=NUM(L)
WRITE(9,20,ERR=8)WEL,NE(NM),'H'
END DO
WRITE(9,16,ERR=8) '/'
WRITE(9,*,ERR=8)'QDRILL'
* Medium Wells
ION=M1+1
M2=2*M1
CALL ORDEM(OIP,NUM,ION,M2)
DO L=ION,M2
NM=NUM(L)
WRITE(9,13,ERR=8)WEL,NE(NM),'H'
END DO
WRITE(9,16,ERR=8) '/'
WRITE(9,*,ERR=8)'QDRILL'
* Upper Wells
ION=M2+1
CALL ORDEM(OIP,NUM,ION,NWC)
DO L=ION,NWC
NM=NUM(L)
WRITE(9,13,ERR=8)WEL,NE(NM),'H'
END DO
WRITE(9,16,ERR=8) '/'
8 PRINT *,N,'FIN'
PRINT *,'TOTAL NO. OF WELL:',NWC
WRITE(10,*,ERR=8)'TOTAL NO. OF
WELL:',NWC
WRITE(10,*,ERR=8)N,'FIN'
STOP
7 PRINT *,'File not opened'
WRITE(10,*,ERR=8)'File not opened'
16 FORMAT(A2,I3,A1,
4I6,2XA64,F10.3,F10.4)
28 FORMAT(A5,A17)
20 FORMAT(A2,I3,A1,2XA5,2I6,2XA17,'
/',F10.0,F10.3)
12 FORMAT(A64)
13 FORMAT(A2,I3,A1,
A40,F10.0,F10.3,F10.1)
5 CLOSE (1)
CLOSE (2)
CLOSE (3)
END
SUBROUTINE ZMED(I0,J0,K0,IMI,JMJ,L8)
INTEGER L8(8)
* For each cell:
* Corner 1 lower i lower j upper k
i- j- k+
* Corner 2 higher i lower j upper k
i+ j- k+
* Corner 3 lower i higher j upper k
i- j+ k+
* Corner 4 higher i higher j upper
k i+ j- k+
* Corner 5 lower i lower j down k
i- j- k-
* Corner 6 higher i lower j down k
i+ j- k-
* Corner 7 lower i higher j down k
i- j+ k-

```

* Corner 8 higher i higher j down k
i+ j- k-

IJ4=4*IMI*JMJ

* to extract z co-ordinates for
each corner, from ZCORN array, above
convention

L8(2)=2*I0+4*IMI*((J0-
1)+2*JMJ*(K0-1))

L8(1)=L8(2)-1

L8(4)=2*I0+2*IMI*((2*J0-
1)+4*JMJ*(K0-1))

L8(3)=L8(4)-1

L8(5)=L8(1)+IJ4

L8(6)=L8(5)+1

L8(7)=L8(3)+IJ4

L8(8)=L8(7)+1

RETURN

END

* SUBROUTINE ORDEM orders a subset
of wells through number NPO

* by descending values of vector
Za. The subset starts at Juno, ends at
LM.

* Vector NPO may initially have the
numeral order (1,2,3,...) and is output

* having in the first place the
well number having the highest Za,
and subsequently

* to the well having the lowest Za

SUBROUTINE ORDEM(ZA,NPO,JUNO,LM)

DIMENSION ZA(640)

INTEGER NPO(640)

ML=(LM+JUNO-1)/2

DO IA=JUNO,ML

ZMX=-1E32

ZMN=1E32

DO IB=IA,LM-IA+JUNO

IC=NPO(IB)

IF(ZA(IC).GT.ZMX) THEN

ZMX=ZA(IC)

IMAX=IB

ELSE

IF(ZA(IC).LT.ZMN) THEN

ZMN=ZA(IC)

IMIN=IB

ENDIF

ENDIF

END DO

*In each step places the well hav-
ing the highest value in subsequent
order

* at the beginning, and the well
having the lowest value at the end.
Places

* are exchanged with wells in those
positions.

* Reference is the well number at
the original list.

NPOIMAX=NPO(IMAX)

NPO(IMAX)=NPO(IA)

NPO(IA)=NPOIMAX

NPOIMIN=NPO(IMIN)

NPO(IMIN)=NPO(LM+JUNO-IA)

NPO(LM+JUNO-IA)=NPOIMIN

END DO

RETURN

END

DEVELOPMENT OF HFU-BASED PERMEABILITY PREDICTION MODELS USING CORE DATA FOR CHARACTERISATION OF A HETEROGENEOUS OLIGOCENE SAND IN THE NAM CON SON BASIN

Nguyen Van Hieu¹, Nguyen Hong Minh¹, Phan Ngoc Quoc¹, Pham Huy Giao^{1,2}

¹Vietnam Petroleum Institute (VPI)

²PetroVietnam University (PVU)

Email: hieunv@vpi.pvn.vn

<https://doi.org/10.47800/PVJ.2021.10-03>

Summary

Core data by both routine and special core analysis are required to understand and predict reservoir petrophysical characteristics. In this research, a total number of 50 core plugs taken from an Oligocene sand in the Nam Con Son basin, offshore southern Vietnam, were tested in the core laboratory of the Vietnam Petroleum Institute (VPI).

The results of routine core analysis (RCA) including porosity and permeability measurements were employed to divide the study reservoir into hydraulic flow units (HFUs) using the global hydraulic elements (GHEs) approach. Based on five classified HFUs, 16 samples were selected for special core analysis, i.e., mercury injection capillary pressure (MICP) and grain size analyses for establishing non-linear porosity-permeability model of each HFU based on Kozeny-Carman equation, which provides an improved prediction of permeability ($R^2 = 0.846$) comparing to that by the empirical poro-perm relationship ($R^2 = 0.633$).

In addition, another permeability model, namely the Winland R35 method, was applied and gave very satisfactory results ($R^2 = 0.919$). Finally, by integrating the results from MICP and grain size analyses, a good trendline of pore size distribution index (λ) and grain sorting was successfully obtained to help characterise the study reservoir. High λ came with poor sorting, and vice versa, the low λ corresponded to good sorting of grain size.

Key words: Core analysis, hydraulic flow units (HFU), non-linear poro-perm, Oligocene sand, Nam Con Son basin.

1. Introduction

Many essential parameters to understand reservoir characteristics are derived from a series of core analysis, from core testing, routine core to special core analysis. The aim of this study is to find out a number of relevant relationships between different petrophysical parameters based on the core testing data to help predict permeability, pore size distribution and grain sorting for a reservoir. Nam Con Son basin (Figure 1) is the second largest hydrocarbon basin after Cuu Long basin, and the biggest natural gas producing basin in Vietnam. While oil production continually declines in Cuu Long, the exploration and production activities in Nam Con

Son play an important role for the oil and gas industry of the country. Unfortunately, the clastic reservoirs in this basin are often found heterogeneous, in particular the Oligocene sands, therefore finding good non-linear permeability prediction models is an important task.

In this study, core plugs were taken from conventional cores collected in Oligocene sandstone. Each core plug has 1.5" diameter and approximately 2" length. After the samples were trimmed to get the right cylinder shape, the cores were cleaned to remove any salt or hydrocarbon contents, and dried in a humidity oven for at least 48 hours at 60 °C and 40 %RH to preserve sensitive clay minerals. When the drying process was completed, the samples were stored in desiccators to avoid vapour absorption. Core testing including porosity, permeability, MICP and grain size measurements was conducted.



Date of receipt: 5/7/2021. Date of review and editing: 5/7 - 30/9/2021.

Date of approval: 7/10/2021.

The porosity was measured by UltraPore-300™ and CMS-300 equipment using the Boyle’s Law gas expansion method.

Gas (nitrogen) permeability was determined using gas permeameter (GasPerm) equipment. Firstly, the sample was pushed in the core holder and confined, then nitrogen was passed through the sample at a known flow rate. Upstream pressure and flow rate were monitored until stable indicating steady-state conditions. Permeability using Darcy’s equation was calculated from these data.

Mercury injection capillary pressure (MICP) was performed on Autopore IV equipment, the sample was initially filled with mercury under a vacuum and was incrementally pressurised to a maximum of 60,000

psia. The volume of mercury injected was determined by the change in capacitance in the capillary stem. This equipment can detect pore diameter range from approximately 0.002 μm to 360 μm.

The grain size analysis was also conducted during thin section analysis. Based on standard deviation (σ_1) of grain size, the grain sorting of each sample was classified to three main types as poorly, moderately, or well-sorted.

2. Methodology

2.1. Core preparation

A total of 50 core plugs were taken and their porosity and permeability were measured, based on which the target reservoir was divided into five hydraulic flow units by Global Hydraulic Elements method. Subsequently, 16 samples were selected from the identified HFUs for MICP and grain size analyses (Figure 2).

2.2. Presentation and analysis of core data

2.2.1. Empirical porosity-permeability (poro-perm) cross plot

This is the most used porosity-permeability relationship, constructed by plotting the core-measured permeability ($\log k$) versus porosity (Φ) values in a semilogarithmic scale. It is an empirical poro-perm model that can effectively predict the permeability based on core porosity measurements [2]. However, in reality most reservoirs are geologically heterogeneous and anisotropic, thus a simple empirical poro-perm model may not work well, and more complex porosity-permeability models have been developed to help predict permeability, in particular for the uncored reservoir intervals. One of these non-linear models

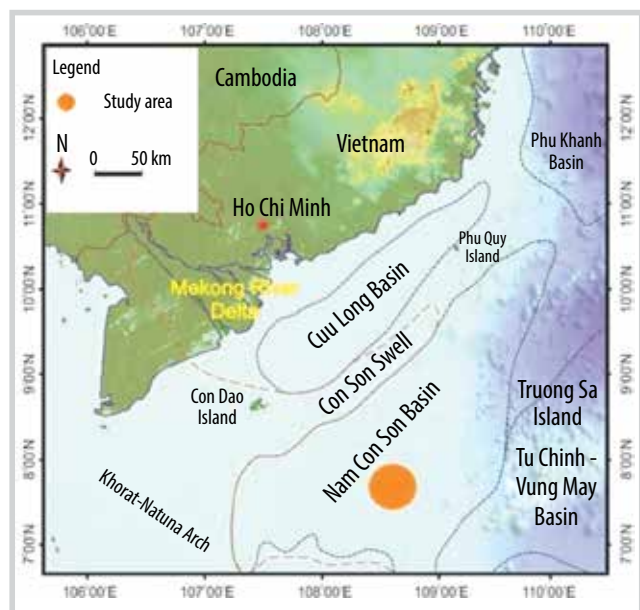


Figure 1. Study location in the Nam Con Son basin, Vietnam [1].

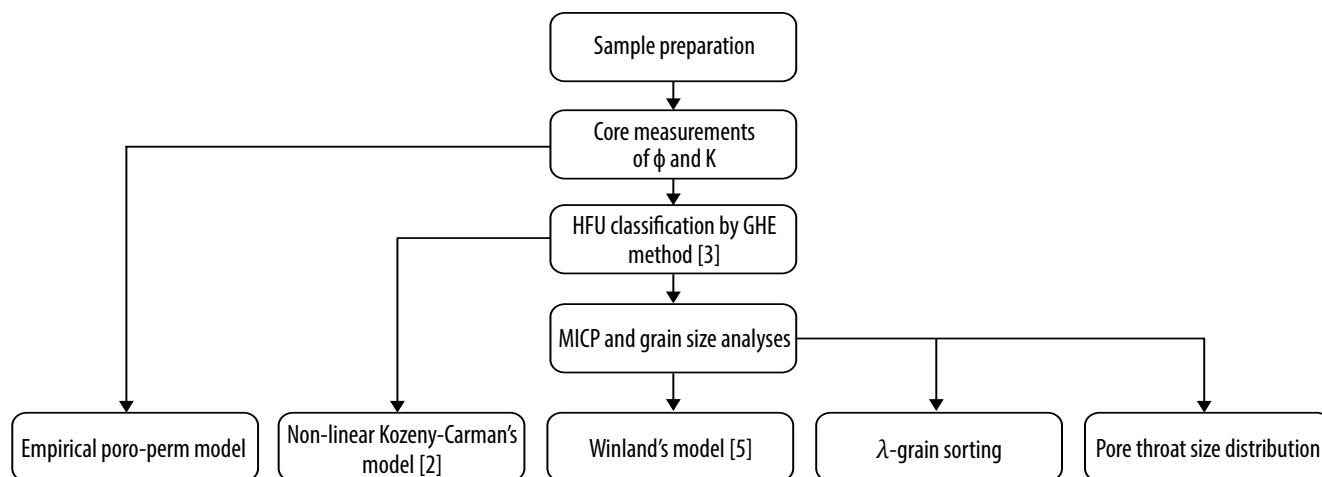


Figure 2. Flowchart of the study.

Table 1. Hydraulic unit lower boundaries (shown as FZI values) for GHEs [3]

FZI	48.026	24.013	12.006	6.003	3.002	1.501	0.750	0.375	0.188	0.094
GHE	10	9	8	7	6	5	4	3	2	1

based on Kozeny-Carman Equation 2 is described in the following.

2.2.2. Classification of HFU by GHE method [3]

Hydraulic flow unit is a concept commonly used in petrophysics nowadays [2]. It is considered as a part of the reservoir where geological and petrophysical properties that affect the flow of fluid are consistent and predictably different from those of other parts of the same reservoir.

Corbett and Potter have developed a new technique of reservoir rock typing using the flow zone indicator (FZI) values [3]. They defined rock type and HFUs based on a series of ten FZI boundary values (Table 1).

The hydraulic quality of the rock is controlled by its pore geometry, which is a function of mineralogy and texture such as grain size, grain shape, sorting and packing as presented in Kozeny-Carman equation below [2]:

$$K = \frac{1}{F_s \tau^2 S_{gr}^2} \frac{\Phi_e^3}{(1-\Phi_e)^2} \quad (1)$$

Where:

K is permeability, μm^2 ;

F_s is the shape factor;

τ is tortuosity;

S_{gr} is the specific surface area per unit grain volume, μm^{-1} ;

Φ_e is effective porosity, frac.

Taking square root of both sides of Equation 1 one gets:

$$\sqrt{\frac{K}{\Phi_e}} = \left(\frac{1}{\sqrt{F_s \tau S_{gr}}} \right) \left(\frac{\Phi_e}{1-\Phi_e} \right) \quad (2)$$

Denoting: $\sqrt{\frac{K}{\Phi_e}} = RQI$ is reservoir quality index; $\frac{1}{\sqrt{F_s \tau S_{gr}}} = FZI$ is flow zone indicator that represents textural characteristics of the reservoir; $\frac{\Phi_e}{1-\Phi_e} = \Phi_z$ is normalised porosity, which is the ratio between pore volume and grain volume.

Substituting RQI, FZI and Φ_z into Equation 2 one has:

$$FZI = \frac{RQI}{\Phi_z} \quad (3)$$

Finally, Equation 1 can be rewritten as below to allow the permeability calculation of each HFU:

$$K = 1014 \times FZI_{avg}^2 \times \frac{\Phi_e^3}{(1-\Phi_e)^2} \quad (4)$$

where FZI_{avg} is the average FZI value of each HFU; Equation 4 is the permeability model based on Kozeny-Carman equation; 1014 is a constant to convert the permeability unit from μm^2 to millidarcy (mD).

2.2.3. Pore throat size calculation

Pore throat size distribution of reservoir rock offered a promised understanding of fundamental flow processes in the porous matrix. It is, therefore an important parameter that reflects the reservoir quality. For instance, one rock containing the majority of the macro pore throat size suggests it may be a highly permeable rock and vice versa. Based on MICP data, pore throat size can be calculated directly from Washburn equation as below [4]:

$$P_c = \frac{2C\sigma \cos(\theta)}{r_c} \quad (5a)$$

$$r_c = \frac{P_c}{2C\sigma \cos(\theta)} \quad (5a)$$

where P_c is the capillary pressure, psi; C is the Washburn constant (0.145038); σ is the interfacial tension (Air-Hg), dynes/cm (485); θ is the contact angle (Air-Hg), degrees (140); and r_c is the pore throat radius, μm .

2.2.4. Pore size distribution index (λ)

The pore size distribution index (λ) is a key parameter for characterisation of a heterogeneous porous medium, which has a strong influence on the capillary pressure shape curves as shown by Brooks-Corey's equation [5] below:

$$P_c = P_d \left(\frac{S_w - S_{wir}}{1 - S_{wir}} \right)^{\frac{-1}{\lambda}} \quad (6)$$

Taking the logarithm of both sides of Equation 6 one gets:

$$\ln(P_c) = \ln(P_d) + \left(\frac{-1}{\lambda} \right) \ln \left(\frac{S_w - S_{wir}}{1 - S_{wir}} \right) \quad (7)$$

where P_c is capillary pressure, psi; P_d is the entry (displacement) capillary pressure, psi; λ is the pore size

distribution index; S_w is the water saturation (frac); S_{wir} is the irreducible water saturation (frac); $\left(\frac{S_w - S_{wir}}{1 - S_{wir}}\right)$ is the normalised water saturation.

By plotting the values of P_c versus the normalised water saturation on a log-log scale following Equation 7 one will get a straight line having the slope equal to $(-1/\lambda)$, and the intercept of $\ln(P_d)$. This represents the basis of a graphical procedure to determine the pore distribution index.

2.2.5. Pore throat radius (R35) and Winland' R35 approach

R35 is the pore throat radius value corresponding to 35% mercury saturation from mercury injection capillary pressure test. Winland [5] suggested that the effective pore system that dominates flow through rock corresponds to a mercury saturation of 35% as shown in Equations 8a and 8b, and the producing capacity of each pore throat group is shown in Table 2:

$$\log(R35) = 0.732 + 0.588 \log(k) - 0.864 \log(\Phi) \quad (8a)$$

$$\log k = \frac{1}{0.588} [0.732 - 0.864 \log(\Phi) - \log(R35)] \quad (8b)$$

3. Results and discussion

3.1. Empirical porosity-permeability relationship

Measurements of permeability and porosity of all 50 samples are plotted in Figure 3, giving a poro-perm relationship as shown in Equation 9 with $R^2 = 0.633$:

$$K = 2.54 \times 10^{-5} \times e^{73.65\Phi_e} \quad (9)$$

3.2. Hydraulic flow unit identification and permeability prediction

Figure 4 shows a plot of RQI versus Φ_z , based on which five discrete rock types were identified and supposed to correspond to five HFUs, having the average FZI equal to 0.115, 0.287, 0.481, 1.048 and 2.324, respectively (Table 3). It is clearly seen that the higher FZI the better reservoir quality in terms of fluid flow in the reservoir rock. For each HFU, the permeability can be calculated using the non-linear poro-perm model in Equation 4, which is plotted versus the measured permeability as shown in Figure 5, showing a good $R^2 = 0.846$.

Table 2. Production capacity based on R35 [5]

Port size	R35 value (µm)	Production capacity (bbl/day)
Mega	>10	Tens of thousands
Macro	2 to 10	Thousands
Meso	0.1 to 2	Hundreds
Micro	<0.1	Non-pay zone

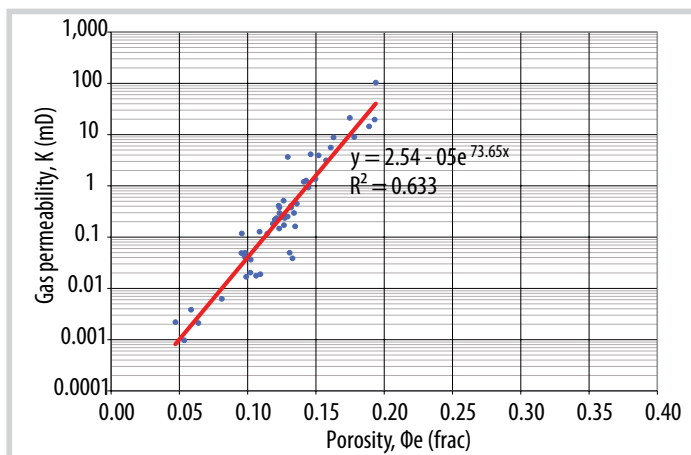


Figure 3. Empirical porosity - permeability model.

Table 3. Average FZI value of five identified HFUs

Hydraulic flow unit	Average flow zone indicator, FZI _{avg.}	Number of samples of each HFU
HFU1	0.115	12
HFU2	0.287	20
HFU3	0.481	7
HFU4	1.048	9
HFU5	2.324	2

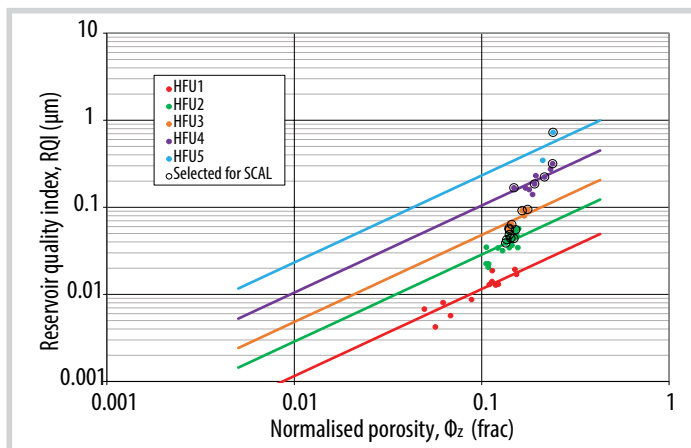


Figure 4. Identification of 5 HFUs based on reservoir quality index (RQI) versus the normalised porosity (Φ_z) relationship.

3.3. Results of mercury injection capillary pressure (MICP) and grain size analyses

Among five classified HFUs, HFU1 has the lowest average FZI. It was considered a non-reservoir and eliminated in further reservoir characterisation. A total of 16 samples from HFU2, HFU3,

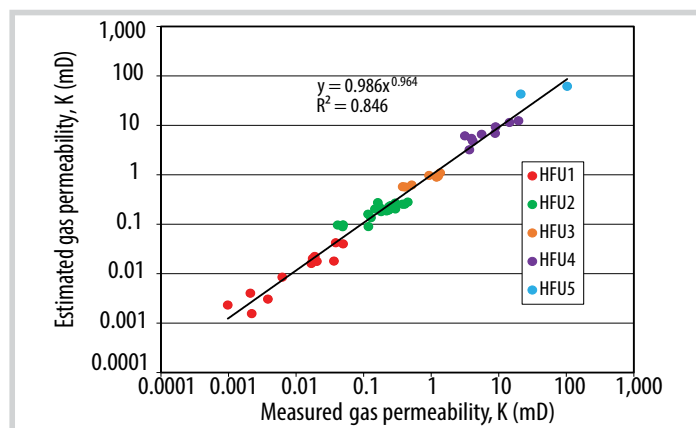


Figure 5. Measured permeability versus calculated permeability by Kozeny-Carman equation for five HFUs.

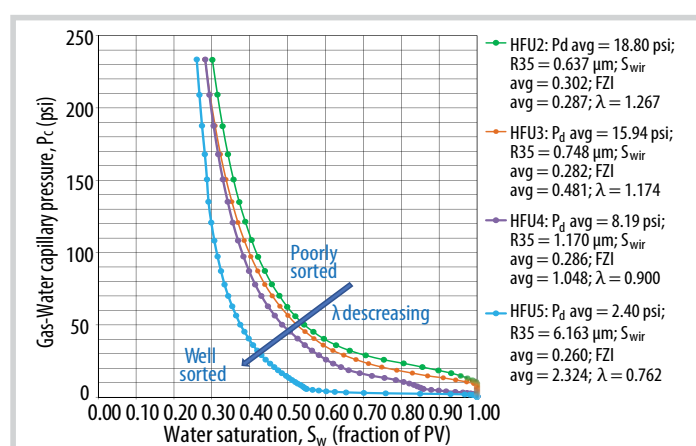


Figure 6. Capillary pressure curves for HFUs 2 to 5.

HFU4 and HFU5 were selected for MICP and grain size analyses. The capillary pressure of the air-mercury system was converted to the gas-water system, and the approximately residual water saturation values were taken at 230 psi of the gas-water system.

The summary of results is presented in Table 4, indicating that the grains of samples in HFU2 were poorly to moderately sorted, showing the highest average pore size distribution index ($\lambda = 1.267$), while most of the well-sorted samples in the HFU4 and HFU5 have lower λ of 0.900 and 0.762, respectively. On the other hand, most of the moderately to well-sorted samples in HFU3 λ range from 1.116 to 1.264. By plotting capillary pressure versus water saturation as shown in Figure 6 with the changes in λ and grain sorting [6], it can be observed that the samples with low λ tend to be well-sorted, whereas those with larger λ showed poorer sorting.

3.4. Pore throat size distribution and R35 value

As seen in Figure 7, the pore throat sizes of all samples are broadly presented from macro to micro and smaller. Generally, the pore throat sizes of HFU2 and HFU3 vary from meso to micro and smaller, while those of HFU4 and HFU5 are found in a narrower range from macro to meso.

Table 4. Summary of MICP and grain size analyses results

Sample No.	Helium porosity frac	Gas permeability mD	RQI, μm	P_d		Lamda (λ)	Correlation coefficient (R^2)	S_{wir} , frac	R35, μm	HFU	Grain size analysis	
				Air-Hq, psi	Air-W, psi						Standard deviation (σ_1)	Grain Sorting
9	0.132	0.41	0.363	97.23	18.84	1.250	0.914	0.317	0.575	2	0.71	M
11	0.129	0.25	0.295	110.13	21.34	1.322	0.918	0.303	0.533	2	0.66	M-W
12	0.120	0.22	0.311	92.48	17.92	1.237	0.920	0.303	0.681	2	0.72	M
13	0.123	0.30	0.345	80.65	15.63	1.210	0.917	0.279	0.806	2	0.70	M
14	0.119	0.18	0.289	108.06	20.94	1.310	0.924	0.348	0.518	2	1.33	P
16	0.125	0.25	0.308	93.66	18.15	1.272	0.930	0.261	0.706	2	0.64	M-W
Average HFU2			0.319	97.03	18.80	1.267		0.302	0.637			
3	0.141	1.20	0.557	67.77	13.13	1.161	0.912	0.239	1.026	3	0.41	W
6	0.123	0.38	0.391	91.66	17.76	1.136	0.879	0.365	0.465	3	0.99	M-C
7	0.126	0.52	0.439	83.75	16.23	1.190	0.912	0.287	0.742	3	0.64	M-W
8	0.150	1.36	0.538	71.44	13.84	1.116	0.902	0.273	0.833	3	0.69	M-W
10	0.123	0.41	0.410	96.60	18.72	1.264	0.919	0.245	0.673	3	0.62	M-W
Average HFU3			0.467	82.24	15.94	1.174		0.282	0.748			
1	0.178	8.98	1.029	38.50	7.46	0.852	0.873	0.298	1.044	4	0.49	W
4	0.161	5.60	0.967	80.51	15.60	1.165	0.902	0.336	0.593	4	0.55	M-W
5	0.193	19.67	1.325	26.91	5.21	0.864	0.878	0.264	1.879	4	0.45	W
15	0.129	3.67	1.125	23.12	4.48	0.721	0.809	0.248	1.166	4	0.49	W
Average HFU4			1.112	42.26	8.19	0.900		0.286	1.170			
2	0.194	103.27	3.014	12.38	2.40	0.762	0.894	0.260	6.163	5	0.45	W
Average HFU5			3.014	12.38	2.40	0.762		0.260	6.163			A

Referring to Table 4, most of the R35 values of the HFUs 2 to 4 belong to the meso pore size groups with production capacity of hundreds bbl/day, except the HFU5 that has the highest R35 value of 6.163 μm and is identified as macro pore with production capacity of thousands bbl/day.

Permeability predicted by the Winland’s model (Equation 8b) matches well with the measured permeability values as seen in Figure 8, showing good coefficient ($R^2 = 0.919$).

From the results calculated by three permeability models as plotted in Figure 9, one can see that Kozeny-Carman’s model and Winland’s model gave a better correlation coefficient (R^2) compared to that by the empirical poro-perm model.

4. Conclusions and recommendations

Core tests were conducted over a set of 50 core plugs taken from the Oligocene sand in the Nam Con Son basin. Subject to the core analysis and interpretation results, the following conclusions were drawn:

- Based on the conventional RCA measurements of porosity and permeability, an empirical poro-perm model was successfully found for the study Oligocene sand (Figure 3 and Equation 9) with a correlation coefficient $R^2 = 0.633$ as reproduced below:

$$K = 2.54 \times 10^{-5} \times e^{73.65\phi_e} \quad (10)$$

By applying the GHE method [3] the study clastic reservoir was divided into five hydraulic flow units (HFUs) denoted from HFU1 to 5. For each of them, the following non-linear permeability prediction models were found using the modified Kozeny-Carman equation (Equation 4) as reproduced below:

$$K = 1,014 \times 0.013 \times \frac{\phi_e^3}{(1-\phi_e)^2} \quad \text{for HFU1 (11a)}$$

$$K = 1,014 \times 0.082 \times \frac{\phi_e^3}{(1-\phi_e)^2} \quad \text{for HFU2 (11b)}$$

$$K = 1,014 \times 0.232 \times \frac{\phi_e^3}{(1-\phi_e)^2} \quad \text{for HFU3 (11c)}$$

$$K = 1,014 \times 1.099 \times \frac{\phi_e^3}{(1-\phi_e)^2} \quad \text{for HFU4 (11d)}$$

$$K = 1,014 \times 5.401 \times \frac{\phi_e^3}{(1-\phi_e)^2} \quad \text{for HFU5 (11e)}$$

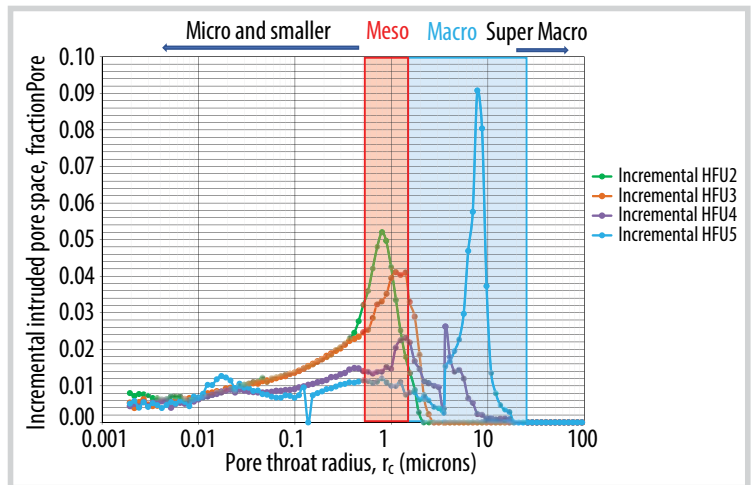


Figure 7. Pore throat size distribution for each HFU.

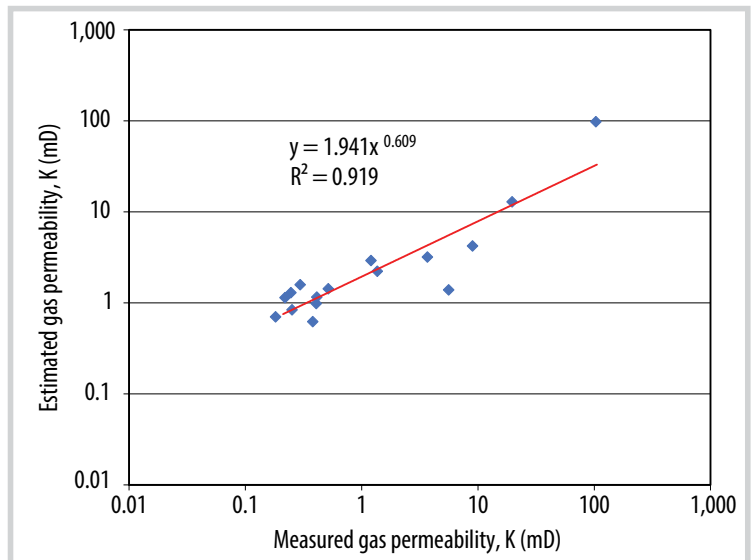


Figure 8. Measured permeability versus permeability calculated by Winland’s equation (Equation 8b).

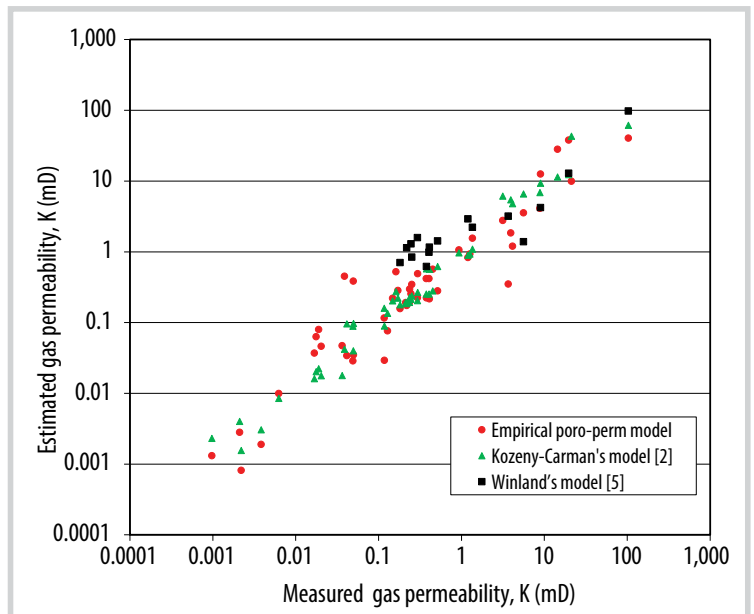


Figure 9. Comparison of three permeability prediction models developed in this study.

By plotting the permeability calculated by Equations 11a-e and comparing with the measured permeability as shown in Figure 5, one can see an increase of R^2 to 0.846, which is higher than that by the empirical model mentioned above with $R^2 = 0.633$.

Among the five identified hydraulic flow units, HFU1 has the lowest average FZI and was considered as non-reservoir. A total of 16 samples were selected only from HFU2, HFU3, HFU4 and HFU5 for further SCALs of mercury injection of capillary pressure (MICP) and grain size analyses. It was found that most of the samples in HFU4 and HFU5 have pore throat size distributing in macro and meso size range, while HFU2 and HFU3 were meso and smaller. Consequently, another permeability prediction model based on Winland R35's equation (Equation 8a) was developed in this study using MICP results as follows:

$$\log k = 1.7 [0.732 - 0.864 \log(\Phi) - \log R35] \quad (12)$$

By plotting the permeability calculated by Equation 8b or 12 and comparing with the measured permeability as shown in Figure 8, one can see a significant improvement of R^2 to 0.919, which is higher than that by the empirical poro-perm with $R^2 = 0.633$. Comparison of the 3 permeability models is shown in Figure 9, illustrating clearly the advantages of HFU-based non-linear permeability to the empirical poro-perm for an Oligocene sand in the Nam Con Son basin.

- It was found that grain sorting of the study Oligocene sand is closely related to the pore size distribution index (λ), i.e., the low λ corresponds to well-sorted grains, while the high λ corresponds to more heterogeneity and poorly sorted grains. Based on the R35 values, the HFU2, HFU3 and HFU4 are of meso pores, while HFU5 is of macro pore. The latter, therefore, can produce hundreds to thousands barrels/day.

- As the HFU-based permeability prediction method based on Kozeny-Carman equation proved to be effective in the characterisation of a heterogeneous Oligocene sand in this study, we recommend it be applied to other

clastic reservoirs and fields in the Nam Con Son basin. It is also recommended to revisit the values of FZI used in HFU classification by the GHE method [3] (Table 3), taking into account the local geological conditions.

Acknowledgements

Acknowledgments are due to the data support given by the Vietnam Petroleum Institute (VPI) and the technical assistance by the Vietnam National Foundation for Science and Technology Development (NAFOSTED) under the grant number 105.99-2019.324.

References

- [1] Pham Huy Giao, Pham Hong Trang, Doan Huy Hien, and Pham Quy Ngoc, "Construction and application of an adapted rock physics template (ARPT) for characterizing a deep and strongly cemented gas sand in the Nam Con Son basin, Vietnam", *Journal of Natural Gas Science and Engineering*, Vol. 94, 2021. DOI: 10.1016/j.jngse.2021.104117.
- [2] Djebbar Tiab and Erle C. Donaldson, *Petrophysics: Theory and practice of measuring reservoir rock and fluid transport properties*. Gulf Professional Publisher, 2015.
- [3] P.W.M. Corbett and D.K. Potter, "Petrotyping: A basemap and Atlas for navigating through permeability and porosity data for reservoir comparison and permeability prediction", *International Symposium of the Society of Core Analysts, Abu Dhabi, UAE, 5 - 9 October 2004*.
- [4] Ngo Thanh Vuong, Lu Dinh Vi, Nguyen Hong Minh, Hoang Manh Tan, Nguyen Manh Hung, and Le Minh Vu, "A comparison of permeability prediction methods using core analysis data", *SPE Reservoir Characterisation and Simulation Conference and Exhibition, Abu Dhabi, UAE, 14 - 16 September 2015*. DOI: 10.2118/175650-MS.
- [5] Tarek Ahmed, *Reservoir engineering handbook*. Gulf Professional Publisher, 2019.
- [6] Robert L. Folk, *Petrology of sedimentary rocks*. Hemphill Publishing Company, 1980.

GEOMECHANICAL MODEL AND SANDING ONSET ASSESSMENT: A FIELD CASE STUDY IN VIETNAM

Nguyen Van Hung, Bui Thi Thuy Linh

Petrovietnam University

Email: hungnv@pvu.edu.vn

<https://doi.org/10.47800/PVJ.2021.10-04>

Summary

Sand production is a key issue when selecting and applying completion solutions like open holes, screens or perforated liners. This problem can be seen in several types of reservoirs such as weakly consolidated and non-consolidated carbonates. The paper presents a method to model wellbore failures for sanding prediction. Our study shows that the potential sand risk in this field is defined by the rock strength rather than the in-situ stress. If the rock is sufficiently competent, the potential of sand production is negligible and the development wells can be completed conventionally without any downhole sand control for the reservoir pressure above 1,280 psi and the maximum drawdown pressure of 2,380 psi.

Key words: Sand production, in-situ stress, sand control.

1. Introduction

Mitigation of sand production is an important and challenging issue in the petroleum industry which requires sand control decision-making. Although approximately 60% of the world's oil and gas production comes from carbonates, about 70% of the petroleum reservoirs worldwide are located in sandstone formations where sand production can be a potential problem [1]. Some carbonate reservoirs may also produce solids [2]. In complex reservoir conditions such as deepwater, high temperature, high pressure, there are always problems (produced sand, hydrates, scale, wax/asphaltene, etc.). Sand production can lead to erosion, loss of integrity and potential fatalities. Applying different methods of sand control usually causes a reduction in well productivity and increasing cost of well.

Sanding is caused by the disaggregation of formation rock because of the in-situ stress and the fluid hydrocarbon flow from a weakly consolidated and non-consolidated sandstone reservoir. The sand production process can be divided into three stages: (i) rock matrix failure and opening hole or perforation from which free

sand grains are generated, (ii) detachment of sand grains from failed rock, and (iii) transportation of free grains by reservoir effluents into the wellbore and up to the surface [3]. There are several elements which must be considered to understand the mechanism of sand production that occurs, including near wellbore stress, rock and fluid properties, rock composition, drilling and production operations and geological conditions. Under the initial condition, a virgin formation will be unchanged in its stress state. Perforation or completion of the formation would change the stress state around the perforation hole.

Sand production prediction is important, and traditional remedies used in petroleum engineering today are based on field observation and experience, laboratory experiments and numerical modelling. In recent years, neural network-based techniques evolved through the work of Kanj and Abousleima [4]. The observation and empirical methods attempt to establish a correlation using multi-variable linear regression between the data collected from a sand producing well and the operational and field parameters (production rate, drawdown) relating to reservoir formation, well completion and production. Several projects have been conducted to predict sand production based on the critical stress state at which failure occurs. Tensile failure appears when



Date of receipt: 9/9/2021. Date of review and editing: 9/9 - 30/9/2021.

Date of approval: 7/10/2021.

effective stress in the rock exceeds its tensile strength, which is mostly applicable in high-rate oil and gas wells. For this group, it is generally assumed that a critical flowrate or drawdown exists which is sufficient to break up the material in tension. This mode of failure can best be visualised in relatively uncemented (commonly referred to as an unconsolidated or weakly consolidated) materials where under right seepage forces the cementation can be broken, leading to transport of sand grains. Such models generally render a maximum drawdown that should not be exceeded. Their practical application has mostly been used for predicting the early life drawdown as the effect of depletion is not rigorously factored into the equations thus making their applications in late life situations unconservative. Shear failure occurs when the tangential stress along the shear plane exceeds a critical value, which depends on the normal stress.

Various failure criteria in terms of functions of the effective stress have been developed. For example, the Mohr-Coulomb, Hoek Brown, Druker-Prager, Lade, and Mogi-Coulomb, Weibols and Cook, Griffith, Tresca criteria are used as the shear failure models for sanding onset [5]. Rock mechanical properties are essential for accurate in-situ stress analysis and geomechanical evaluation including wellbore stability analysis, sand production prediction and management, hydraulic fracturing design, fault stability and reactivation analysis, and other geomechanical applications. The rock mechanical parameters typically recommended to populate a geomechanical model are: unconfined compressive strength (UCS), friction angle (θ) or coefficient of internal friction (μ) (where $\mu = \tan\theta$), thick wall cylinder strength (TWC), elastic moduli (Poisson's ratio (ν), and Young's modulus (E)). While the mechanical parameters can be derived from well logs (bulk density, compressional and shear sonic logs) and laboratory tests on core samples, laboratory measurements of the elastic moduli (triaxial tests) on core samples subjected to the in-situ stress condition are also correlated with well logs to derive a continuous strength profile as a function of depth.

2. Sanding onset workflow

The key feature in sand production prediction is a geomechanical model that consists of field stresses (σ_v , σ_H , σ_h), pore pressure (P_p), direction of σ_H , σ_h , rock strength and elastic moduli [6]. The vertical stress is calculated by integrating the density log (ρ_v) or sonic log. In the absence of both log data, lithological and regional information

can be used to approximate σ_v . The least principal stress is usually evaluated from leak-off tests (LOTs), extended LOTs (ELOTs), or minifrac tests. While a minifrac test is conducted with a particular objective of measuring the minimum horizontal stress in a field, LOTs and ELOTs are usually carried out as part of a drilling programme. In addition, σ_h can be estimated from σ_v and Poisson's ratio by using its relationship or this approach assumes that the ratio between the vertical effective stress and the minimum horizontal effective stress remains constant with depth. The use of regional information and empirical models for σ_h is also useful where reliable field data are not available.

The direction of horizontal stresses is determined from borehole breakout observation, multi-arm calliper logs, drilling-induced tensile fractures (DITF) in high resolution image logs, and transmission of shear wave velocity. If these measures are not available, recent tectonic activities in the area of interest and regional stress data such as the world stress map should be valuable sources of information. It is evident that there is no way to measure or determine directly the value of maximum horizontal stress σ_H . In this situation, the stress polygon method, the linear elastic theory and rock failure criteria for a particular borehole condition should be the good remedies to determine σ_H . Pore pressure is estimated directly from measurements in permeable and reservoir zones such as repeat formation tester (RFT), drillstem test (DST). For sands, the pressures are modelled using buoyancy estimations and depletion, when applicable. It is also important to determine the top of overpressure if any.

The uniaxial compressive rock strength (UCS) profile is determined based on the rock mechanical testing data. There are some references models which can be used: $UCS = 1.35V_p^{2.6}$ (for shale), $UCS = 185165e^{-0.037 \cdot DTCO}$ (for sandstone). The internal friction for lithologies in some cases can be assumed constant 0.4 (for shale), and 0.5 (for sandstone). The Poisson's ratio is 0.2 and 0.3 for sand and shale, respectively.

The geomechanical workflow, as shown in Figure 1, is represented as a series of 10 interdependent steps. The sequence reflects a logical progression of data processing, each step builds upon one or more preceding steps [6].

Sanding onset analysis uses the results of final geomechanical models. These models encompass rock strength profile, initial reservoir pressure, and pressure

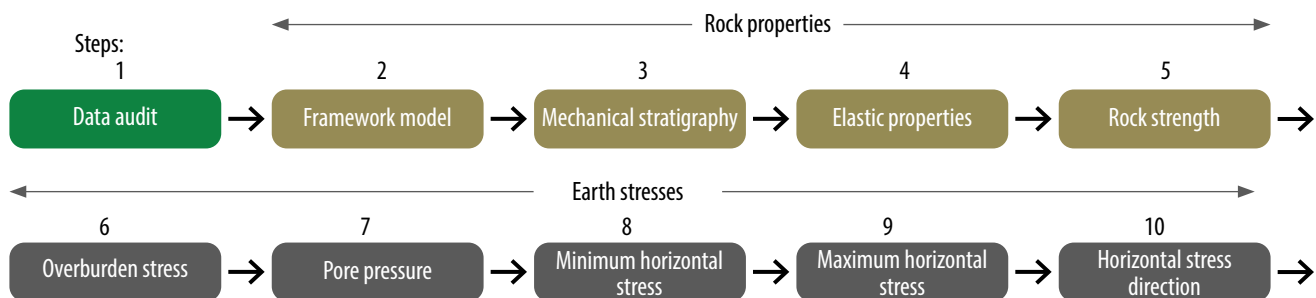


Figure 1. The geomechanical workflow [6].

decline data from the production plan. Then sand-free operating envelopes and sanding evaluation log plots represent specific rock strengths at given depths. The studied reservoir pressure is determined from current drawdown and the planned final abandonment pressures. The sand failure is predicted, and the onset of sand production is assumed from rocks with the specified strength.

3. Shear failure criteria

The first method was used in horizontal wells by BP in 1985 [7]. This method predicts sanding as shear failure, and the production of sand grains is accompanied with fluid flow that transfers disaggregated sands. The mathematical representation is given in Equation 1 and the criterion for sanding is:

$$BHFP \leq (3\sigma_1 - \sigma_3 - \sigma_y) / (2-A) - PrA(2-A) \quad (1)$$

Where CBHFP = critical bottom hole flowing pressure; P_r = current average reservoir pressure; σ_1, σ_3 are the total principal major and minor stresses; σ_y is the effective formation strength ($\sigma_y = 3.1 \times TWC$); Factor 3.1 includes the scale transformation from TWC laboratory sample (OD:ID = 3) to field (OD:ID = infinity); A is the pore elastic constant ($A = (1 - 2\nu) \times \alpha(1 - \nu)$); α is the Biot factor; TWC represents a fundamental measure of strength for an unsupported borehole and perforation.

4. Tensile failure model

This mode of failure can be best matched in weakly consolidated sandstone. This model provides a maximum allowable drawdown. Equation 2 shows the relationship between the rock strength and fluid flow in a perforation:

$$\Delta q = q\mu / 4\pi kr = C(1 + 3\sin\phi) / \tan\phi(1 - \sin\phi) \quad (2)$$

Where q is flow rate, μ is viscosity, r is perforation radius, k is permeability, ϕ is angle of internal friction, C is intact rock cohesive strength.

The critical drawdown (CDP) for liquids is:

$$CDP = 4C \cos\phi / (1 - \sin\phi) \quad (3)$$

5. Case study

5.1. Input data

In order to build the sand production risk model for our proposed production wells, we have collected the following data:

- Geological, petrophysical, logging, drilling, well test, and reservoir data including gamma ray, calliper, neutron porosity, density, resistivity, sonic curves, and dipole logs.
- Geomechanics testing: select rock samples and identify suitable intervals for rock mechanical strength tests.
- In-situ stress model: log data derived strength correlations with strength model from laboratory tests.
- Rock strength model: analysis of density logs, FIT/LOT/ELOT, minifrac, and borehole failure, such as: UCS/C0, TWC, So, θ , E, ν , α .
- Drilling incidents and data from offset wells.

5.2. Geomechanical model

TWC model

Our data collection shows the rock mechanical tests including around 20 UCS and 10 TWC tests. The results are performed in both vertical and horizontal directions. After visual inspection by SEM, X-Ray, and thin-section, we observed that there is no distinct bedding in these cores, so the results from the vertical samples are assumed to be similar to those from the horizontal ones.

The ratio of TWC/UCS from our cores is plotted in Figure 2 and compared with the theoretical model (worldwide data). It can be seen that with hard rocks (UCS > 4,000 psi), the TWC/UCS ratio is constant at just below 2.

However, this ratio increases significantly and can exceed 4 with UCS less than 1,000 psi. This is due to the compaction effect which strengthens the core in TWC behaviour, but it is absent in UCS results. Our result data follow a similar trend to the worldwide data with the range of UCS from 2,096 - 5,670 psi but offset slightly towards the lower TWC/UCS ratios. The model of TWC/UCS ratio from our core tests can be expressed as a function of UCS by Equation 4:

$$\frac{TWC}{UCS} = 87.084UCS^{-0.457} \quad (4)$$

Because TWC values are taken directly in the sand production model, the relationship between TWC and elasticity modulus (Ec) is used to derive a functional continuous rock strength. The reasons for selecting Young's modulus are: Ec can be used to predict strength profiles in the development wells (taking DT data) and, more importantly, the correlation coefficient in the cross-plot is better. Figure 3 shows the relationship between TWC and Ec resulting in the model:

$$TWC = 2460.2Ec - 3209.5 \quad (5)$$

In-situ stress model

Vertical stress and pore pressure model

The analytical models provide stress components in cylindrical coordinates such as tangential, radial around the vertical/horizontal/perforation cavity [8]. These are the stresses that cause the rock surrounding the open cavity to fail. The in-situ principal stresses (vertical, major horizontal stress, minor horizontal stress) are the keys. The

far-field orientation is pivotal for deviated or horizontal wells. The pore pressure also plays a role in modifying the total stress at any point in the rock into an effective stress. In the research area, the normal pressure regime is 0.433 psi/ft over the main intervals of the reservoir in our wells. The vertical stress model is built from density logs $p_b = ad^2 - bd + c$, where d is true vertical depth.

Our density data are available for all wells but the best one is illustrated in Figure 4. We have no data measurement in the shallow depth (less than 1,990 m). The model in this figure indicates a consistent and overlying compaction trend for a standard well (from 1,990 m to 2,532 m). For most sedimentary rocks and in our case, the compaction trend can be described as the relationship between bulk density and depth by Equation 6. This model overestimated formation densities near the mud line, and at depths greater than 3,532 m at TVD. The gradient of overburden is 0.950 psi/ft.

$$\rho_b = 14,768d^2 - 57,808d + 56,858 \quad (6)$$

Minimum horizontal stress

We applied both direct and theoretical methods. Obviously, the direct field measurement is normally preferred by minifrac test and LOT, FIT. In the FIT test, we verify the quality of the cementing of casing, and the pressure is increased until leak-off occurs to the formation due to fracture initiation. In the LOT test, the pressure goes up until fracture initiation has been seen (FIP or leak-off pressure). There is no signal of mud losses during drilling

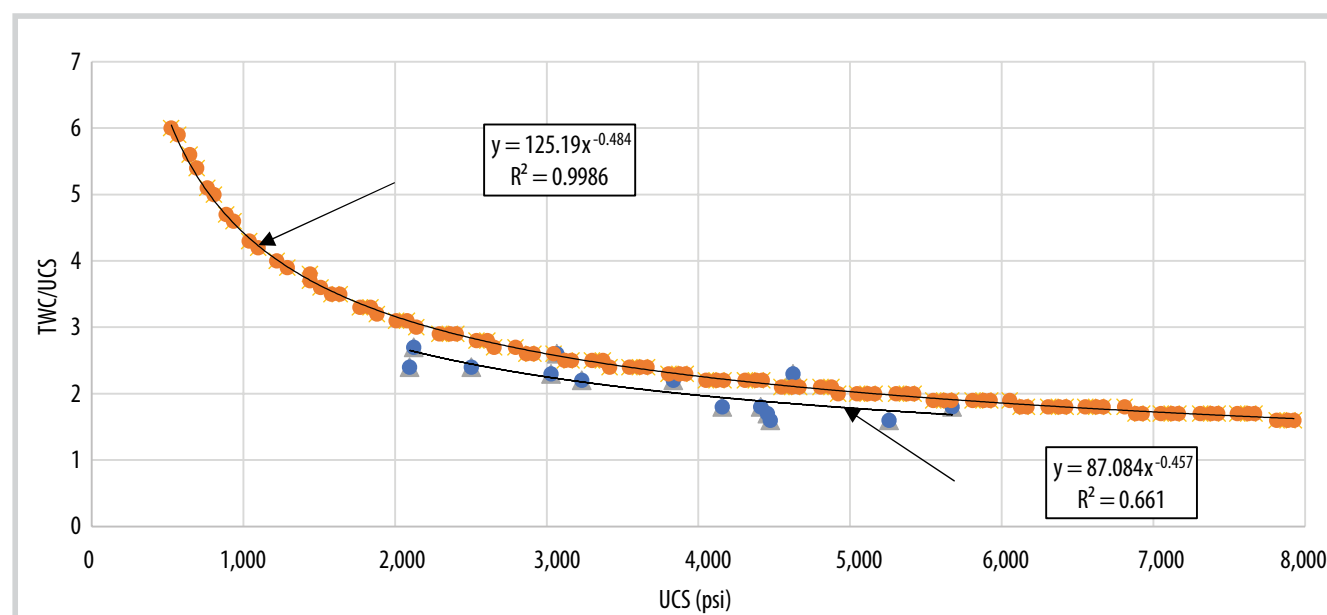


Figure 2. TWC and UCS relationship compared with theoretical model.

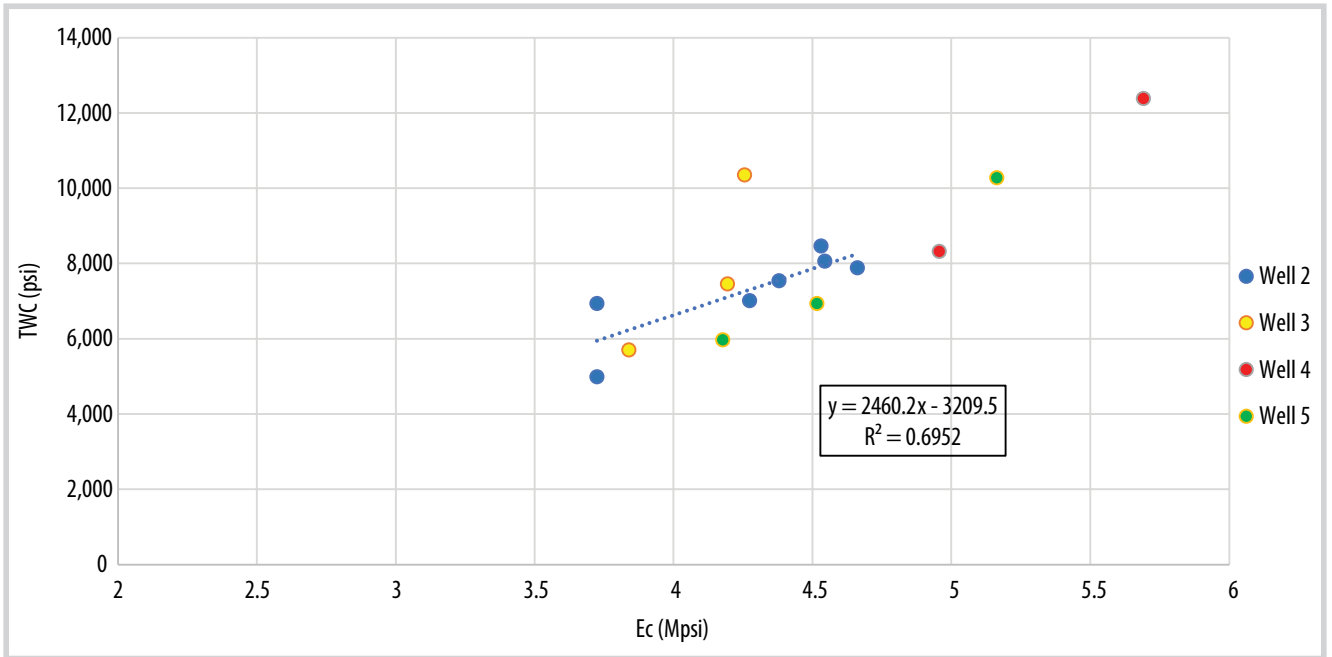


Figure 3. Relationship between TWC and Ec.

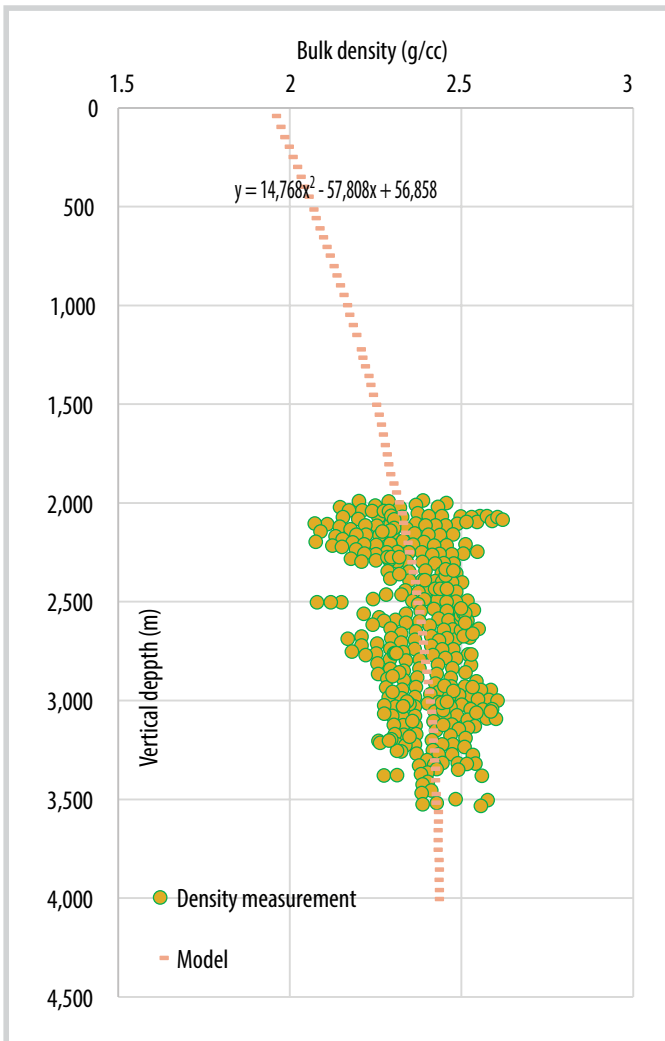


Figure 4. Density versus depth (measurement and model).

operations from mud line to 1,990 m at TVD depth. The uniaxial elastic model provides the calculation of minimum horizontal stress:

$$\sigma_h = \frac{\nu(\sigma_v - \alpha P_p)}{(1 - \nu)} + \alpha P_p \quad (7)$$

Where ν is the Poisson's ratio (0.2 for sand), α is the Biot's factor (1.0 for sand). In our case, the estimated minimum horizontal stress is 0.59 psi/ft.

Maximum horizontal stress and pore pressure

The maximum horizontal stress is determined from observations of image logs and available rock mechanical data. Through breakout observation in some wells, the minimum horizontal stress is in the direction of 35 - 50°, and correspondingly a maximum stress direction of 122 - 140°. In addition, the breakout analysis uses the stress polygon approach to estimate the magnitude of the maximum horizontal stress. Our approach is based on Mohr-Coulomb theory [8]. For the breakout area to occur, it is assumed that the Mohr circle, representing bay hoop stress and radial stress, equals the failure envelope (defined by the cohesive strength and friction angle of the rock material). Equation 8 shows the maximum horizontal stress corresponding to the failure condition:

$$\sigma_H = \frac{C_o + (P_w - \alpha P_p)(\tan\beta)^2 + \sigma_h + P_w + \alpha P_p}{3} \quad (8)$$

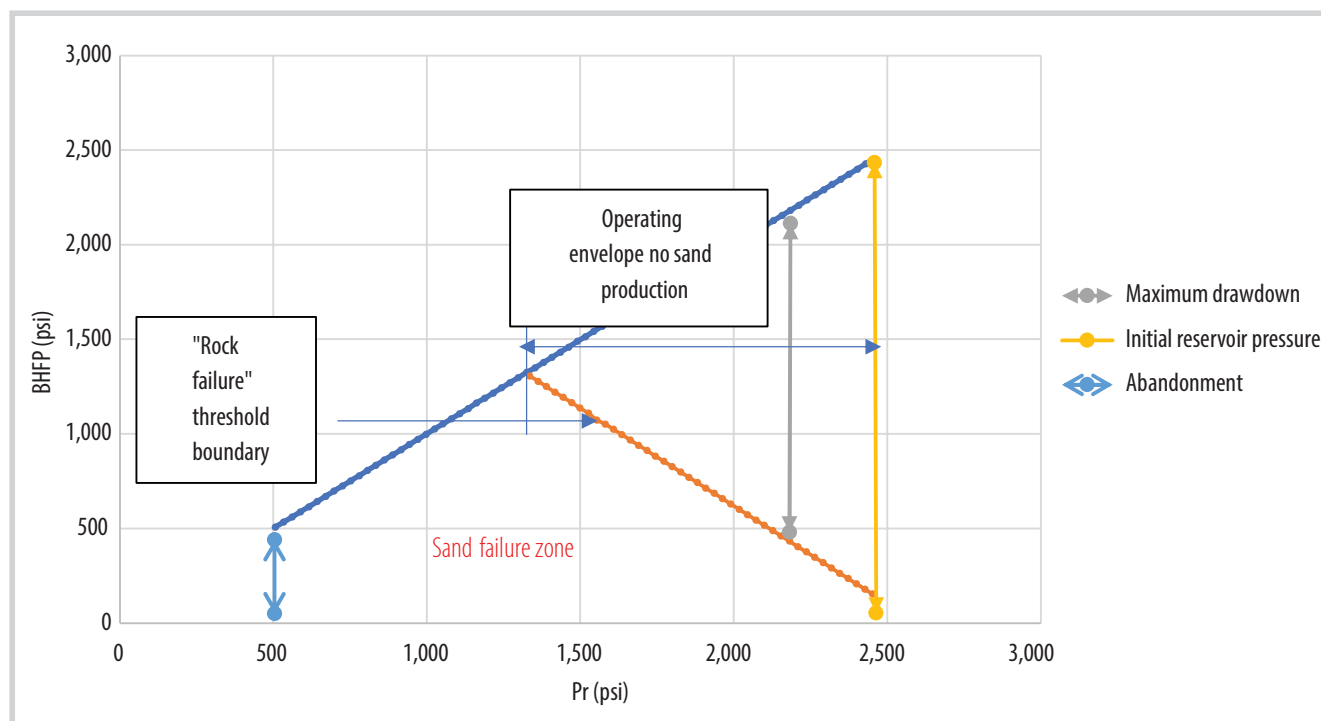


Figure 5. Sand-free operating envelope.

Our data showed the reservoir interval with normal pressure regime of 0.441 psi/ft.

6. Sanding onset assessment

For a vertical well with open hole completion and the input data as illustrated in the previous parts, a sand production model is developed to predict the downhole condition (critical drawdown) required for rock failure, and hence potential sand production [9]. Our model uses the laboratory results of TWC. The tangential stress around an opening (perforation or open hole) is calculated and compared to the effective formation strength. In Figure 5, the BHFP is calculated by Equation 1 and the reservoir pressure at any given time. The result shows the potential reservoir pressure and bottom hole flowing pressure that results in rock failure. When the BHFP > Pr, there is no sand production (above blue line). The red line represents the rock failure threshold, which is for a TWC strength and single perforation or well orientation in this case. Any failing point below the sand failure zone indicates that a failure condition has occurred for the relevant cavity, and that sand production is assumed. Any failing point above the red line represents a no failure condition and sand-free hydrocarbon production. In our case, the maximum drawdown is 2,380 psi and the reservoir pressure should be managed above 1,280 psi.

7. Conclusions

This paper presents a method for sand production prediction from laboratory and field data. The method has been applied to a case to assess sanding risk in a proposed well, helping minimise sanding risk in the future. Sanding evaluation results using the predictive model presented in this paper should be verified by field observations. Sanding evaluations are performed over the lifetime of a field from current to final (abandonment) reservoir pressures and at pressure conditions corresponding to a decrease of up to 500 psi for all existing production wells during their life cycle. Some main points can be concluded through this study:

- Rock strength testing is required prior to the execution of a geomechanical study itself;
- The best model for calculating log-derived strength UCS/TWC can be selected using combination of conventional laboratory triaxial testing and non-destructive methods;
- The maximum drawdown is 2,380 psi and the reservoir pressure should be managed above 1,280 psi.

References

- [1] Jong-Won Choi, *Geomechanics of subsurface sand production and gas storage*. Georgia Institute of Technology, 2011.
- [2] R.S. Wulan, Y. Susilo, Y.S. Hendra, D. Ramdan, and A. Mansur, "Development strategies of soft-friable carbonate gas reservoirs through horizontal open hole gravel packed completions: APN field - offshore West Java", *International Petroleum Technology Conference, Dubai, UAE, 4 - 6 December 2007*. DOI: 10.2523/IPTC-11560-MS.
- [3] A. Joseph, L.C. Akubue, and A.B. Oriji, "Sanding prediction using rock mechanical properties", *Nigeria Annual International Conference and Exhibition, Lagos, Nigeria, 6 - 8 August 2012*. DOI: 10.2118/162945-MS.
- [4] Mazen Y. Kanj and Younane Abousleiman, "Realistic sanding predictions - A neural approach", *SPE Annual Technical Conference and Exhibition, Houston, Texas, 3 - 6 October 1999*. DOI: 10.2118/56631-MS.
- [5] Bernt Aadnøy and Reza Looyeh, *Petroleum rock mechanics - Drilling operations and well design*, 1st edition. Gulf Professional Publishing, 2011.
- [6] Mark D. Zoback, *Reservoir geomechanics*. Stanford University, 2009.
- [7] M. Azad, G. Zargar, R. Arabjamaloei, A. Hamzei, and M.A. Ekramzadeh, "A new approach to sand production onset prediction using artificial neural networks", *Petroleum Science and Technology*, Vol. 29, No. 19, pp. 1975 - 1983, 2011. DOI: 10.1080/10916460903551081.
- [8] Nguyen Van Hung, "Overview of geomechanics and its applications to petroleum industry - A case study for minimum overbalance pressure calculation", *CIGOS 2019: Innovation for Sustainable Infrastructure*, Singapore: Springer, 2020, pp. 739 - 744. DOI: 10.1007/978-981-15-0802-8_117.
- [9] Ian D. Palmer, Nigel Higgs, Ion Ispas, Kirk Baksh, and Kimberly Diane Krieger, "Prediction of sanding using oriented perforations in a deviated well, and validation in the field", *SPE International Symposium and Exhibition on Formation Damage Control, Lafayette, Louisiana, USA, 15 - 17 February 2006*. DOI: 10.2118/98252-MS.

AN OVERVIEW OF THE APPLICATION OF MACHINE LEARNING IN PREDICTIVE MAINTENANCE

Tran Ngoc Trung¹, Trieu Hung Truong², Tran Vu Tung¹, Ngo Huu Hai¹, Dao Quang Khoa¹

¹Bien Dong Petroleum Operating Company

²Ha Noi University of Mining and Geology

Email: trungtn@biendongpoc.vn

<https://doi.org/10.47800/PVJ.2021.10-05>

Summary

With the rise of industrial artificial intelligence (AI), smart sensing, and the Internet of Things (IoT), companies are learning how to use their data not only for analysing the past but also for predicting the future. Maintenance is a crucial area that can drive significant cost savings and production value around the world.

Predictive maintenance (PdM) is a technique that collects, cleans, analyses, and utilises data from various manufacturing and sensing sources like machines usage, operating conditions, and equipment feedback. It applies advanced algorithms to the data, automatically compares the fed data and the information from previous cases to anticipate or predict equipment failure before it happens, thus helping optimise equipment utilisation and maintenance strategies, improve performance and productivity, and extend equipment life. Robust PdM tools enable organisations to leverage and maximise the value of their existing data to stay ahead of potential breakdowns or disruptions in services, and address them proactively instead of reacting to issues as they arise. Therefore, it has attracted more and more attention of specialists in recent years.

This paper provides a comprehensive review of the recent advancements of machine learning (ML) techniques widely applied to PdM by classifying the research according to the ML algorithms, machinery and equipment used in data acquisition. Important contributions of the researchers are highlighted, leading to some guidelines and foundation for further studies. Currently, BIENDONG POC is running some pilot PdM projects for critical equipment in Hai Thach - Moc Tinh gas processing plant.

Key words: Machine learning, predictive maintenance.

1. Introduction

As defined by the European Standard PN-EN 13306 [1], maintenance is “a combination of all technical, administrative, and managerial actions during the life cycle of an item intended to retain it, or restore it to a state, in which it can perform the required function”. Maintenance on the field generally includes repair and replacement of equipment parts to maintain equipment within its operating conditions.

In manufacturing environment, maintenance is one of the critical success factors. Poorly maintained equipment

often leads to unplanned downtime and low performance. Some adverse impacts on business performance are behind schedule operation, waste increase, and poor quality products, etc. According to the International Society of Automation, the cost of machine downtime is USD 647 billion each year globally [2]. Different corporations may have different maintenance strategies depending on several factors, such as maintenance goals, equipment’s nature, operational process design, and work environment. Commonly used maintenance approaches are categorised into a) corrective maintenance (CM), b) preventive maintenance (PM), c) predictive maintenance (PdM), and d) proactive maintenance [3]. Amongst these approaches, the PdM aims to make timely maintenance decisions timely by focusing on fault detection, component diagnosis, degradation monitoring, and



Date of receipt: 21/9/2021. Date of review and editing: 2/9 - 16/10/2021.
Date of approval: 16/10/2021.

failure prediction in real-time, therefore reducing the uncertainty of maintenance activities.

With the Fourth Industrial Revolution (Industry 4.0), IT infrastructure has been continuously improved to support smart sensing, Internet of Things (IoT), big data collection, and analytics tools; companies now can get the most out of their data. Data-driven decisions can be made by analysing historical events and trends in the past [4, 5]. In the case of complex equipment with a large amount of data, processing and analysing become more and more challenging for humans to handle. There are disadvantages of human dependent scenarios, where humans monitor equipment and make decisions manually for the work needed on the equipment. First, specialists' performance is highly dependent on their expertise levels. In a study by Smith-Bindman R. et al. [6], less experienced physicians tend to make false diagnostic decisions at a rate of 50% higher than more experienced ones. This issue becomes worse with industries that lack specialists who are well trained and experienced. In addition, the consistency of diagnostic decisions among specialists cannot be guaranteed. A study by Gulshan et al. [7] compared decisions from seven US-certified ophthalmologists regarding diagnosing the severity levels of diabetic retinopathy based on photographs of the retinal fundus. It showed poor consistency among ophthalmologists, in which only 20% of the cases demonstrating a complete agreement among them. Last but not least, specialists who analyse a large number of data for a long time can make more mistakes and work less efficiently because of mental fatigue and cognitive overload [8].

Artificial intelligence (AI) is an element of Industry 4.0, showing its application in the manufacturing industry as a powerful tool for machine health diagnosis. A recent survey indicated that PdM is expected to be one of the first fields where AI-based technologies will be successfully implemented [9]. Indeed, it is almost impossible for a human operator to interpret data in real-time, and the conventional systems can neither spot anomalies in data nor predict a sensor reading in a specified time window, AI and machine learning (ML) techniques have therefore emerged as a promising tool in PdM applications for intelligent manufacturing in Industry 4.0, which involves rethinking and optimising the entire maintenance strategy as a whole.

As illustrated in Figure 1 machine learning is a subfield of AI and defined as an algorithm or programme capable of learning independently with minimal or without assistance from humans. ML supports solving many complex human problems, such as image processing, big data, robotics, and speech recognition. By utilising ML in processing, continuously monitoring, and analysing equipment's health, corporates can achieve greater operational and maintenance efficiency and effective growth management by improving equipment performance. A case study by Roosefert et al. show an impressive 84% reduction of breakdown time and 88% reduction of breakdown occurrences when applying intelligent ML-based PdM approach compared to the conventional Industry 3.0 setup [10]. This will also increase the availability and reliability of equipment and reduce operational risks, therefore improving corporates' competitive advantages. With recent advances in ML techniques, numerous studies have explored the potential of the ML approach and demonstrated promising results. For example, Akram et al. [11] developed the convolution neural networks (CNNs) for fault detection of photovoltaic cell defects and achieved 93.02% accuracy. In another study, Ren et al. [12] employed region-based CNN (R-CNN) to automate object detection training in real-time. Cha et al. [13] applied R-CNN to detect five types of structural surface damages on bridges and achieved a mean average precision (mAP) of 87.8%. The problem of concern today regarding ML in PdM applications is to choose the most suitable, simple, and effective algorithm for each specific problem. ML algorithms often require large data acquisition about failure situations and different operating states of the system or device to train the model.

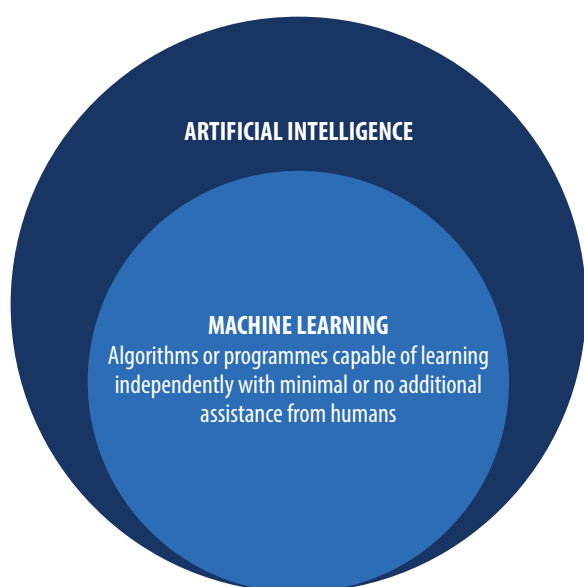


Figure 1. Machine learning is a subset of artificial intelligence.

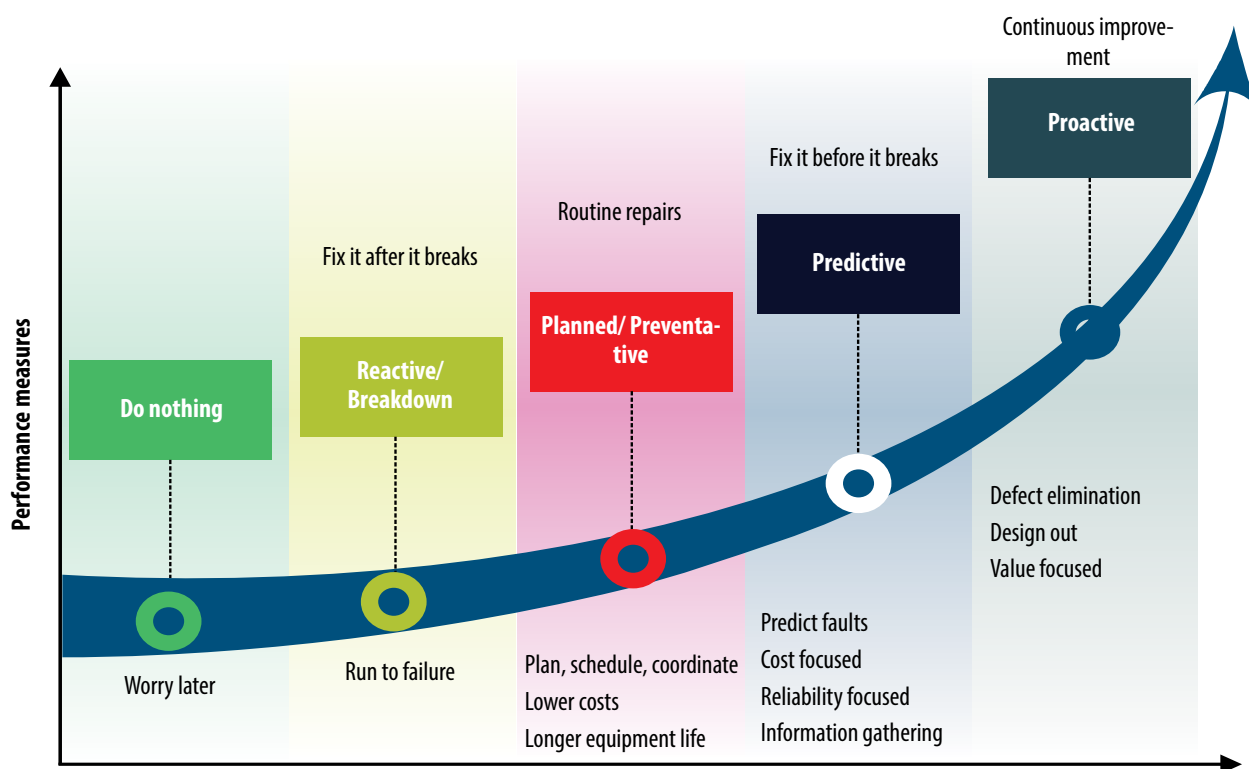


Figure 2. Evolution of maintenance approaches [3].

2. Evolution of maintenance approaches

The evolution of maintenance approaches is presented in Figure 2.

Corrective maintenance (CM), also known as “breakdown maintenance” or “run to failure”, is the first approach to maintenance. No routine maintenance activity is scheduled in this approach, and maintenance actions only occur after equipment breakdown. It is, therefore, impossible to optimise equipment performance with respect to economic or reliability criteria [3], and subsequently, equipment availability and reliability performance are substandard. Despite being inferior to other approaches, the CM approach is still in use due to the low cost of implementation, and suitable for equipment that has a low budget to repair or replace. Companies often apply CM to equipment that has insignificant or no impact on the whole production line.

Preventive maintenance (PM) is the next stage of maintenance approach evolution. PM is a time-based approach where inspection and replacement/repair works are scheduled and conducted regularly before any failure can happen. It aims to avoid system failures during operation, especially when such an event is costly and/or dangerous. PM is the dominant maintenance policy used

in industry. For systems such as transportation, production, or critical infrastructure, the time-based inspection and maintenance policies can improve performance, increase reliability and capability of assets concerned, and reduce the cost of assets running [14]. PM, however, is not always cost-effective. Because maintenance work is carried out on a time basis regardless of equipment’s conditions, it can lead to a high workload and cost if the equipment is still working correctly. Another disadvantage of PM is the infant mortality of equipment induced by human error during preventive maintenance work.

The next level of maintenance approach evolution is condition-based maintenance (CBM), and its improved version which is the so-called predictive maintenance (PdM). The PdM approach uses advanced analytics techniques to predict faults or failures in a deteriorating system to optimise maintenance efforts by monitoring equipment operating conditions and performances to detect any signs of wear or deterioration leading to a component's failure [15, 16]. More than just monitoring the basic condition of equipment, the main objective of PdM which is to predict the remaining useful life of machines using historical data is one of the promising areas of machine prognosis which could lead to significant maintenance optimisation and cost savings.

PdM approaches have been extensively applied in industries for handling the health status of equipment by detecting early signs of failure in advance, enabling maintenance measures to be taken ahead of time, which allows the saving of more costs because repair after failure is always more expensive than maintenance in advance [17]. According to data from McKinsey [18], PdM tools can reduce manufacturing machine downtime by 30% - 50% and increase machine life by 20% - 40%. Besides, PdM initiatives enable organisations around the world to save USD 17B in 2018 globally [19].

In PdM, the optimal time point for maintenance actions is predicted by analysing the system's health state and historical maintenance data to make a timely repair to avoid costly repairs due to system breakdown and premature maintenance activities which may induce infant mortality. The PdM approach is used in industrial sectors where reliability is paramount, like nuclear power plants, transportation systems, or emergency systems [3]. The most used monitoring and diagnostic techniques include vibration monitoring, thermography, tribology, and visual inspection.

On the other hand, proactive maintenance emphasises keeping assets and equipment in top conditions by identifying potential problems and addressing them as early as possible. That is one of the main reasons why proactive maintenance is considered different from other approaches that help reduce maintenance costs and risk of property damage. Some examples of proactive maintenance activities are: (i) applying anti-corrosion coating to metal surfaces; (ii) performing an inspection for cracks, leaks, and rust; (iii) lubricating the machine to reduce wear and diffusion corrosion and (iv) applying sealant for junction boxes to prevent water ingress. In proactive maintenance approach, possible causes of equipment failure are analysed, and works are carried out to eliminate those causes in very early stages (e.g., designing, installation, and commissioning stages), which definitely distinguish proactive maintenance from other approaches.

3. ML approach in PdM

In PdM approach, equipment health is continuously monitored and analysed in real-time. Lei et al. [20] divide the process of diagnosing health of machinery into four steps: (i) data acquisition; (ii) health indicators construction; (iii) health stage division; and (iv) remaining useful life prediction.

In data acquisition phase, the measured data, such as vibration, current, temperature, or pressure signals, are collected from sensors to monitor the health condition of machinery. In the next step, health indicators (HI) are constructed to represent the health condition of machinery using statistics, signal processing, or artificial intelligence techniques. Then, the HI will be analysed and classified into two or more health stages (HS) depending on HI degradation trends. In the final step, the remaining useful life is predicted to determine how much time is left until machinery reaches the end of its lifetime, based on which optimal maintenance activities can be scheduled.

3.1. Data acquisition

Data acquisition is a prerequisite from which raw data can be processed and analysed later to solve a PdM problem. Data acquisition involves designing and sizing the appropriate system architecture to be installed on the equipment to capture and store different sensing data. A data acquisition system consists of sensors, data transmission, and data storage devices. Depending on equipment types, different combinations of sensors are used so that the captured data can fully reflect the degradation process of machinery. Some commonly used sensors are accelerometers, acoustic emission sensors, infrared thermometers, current, temperature, and pressure sensors, etc. The captured data are transmitted into a PC or portable devices through a data transmission device and stored in a memory location or historian system for further analysis. With a rapid development of sensor and communication technologies, more advanced data acquisition devices have been designed and applied to modern industries.

One of the essential data acquisition techniques often discussed in ML algorithms is data pre-processing techniques. In this step, commonly used techniques for data pre-processing include data normalisation and noise removal, feature extraction, and feature selection. Feature extraction is the process of mapping the original dataset to new data space, including new attributes that contain more explicit information for performing PdM. There are two basic feature extraction methods commonly applied in PdM: data-driven and statistical techniques.

With the data-driven technique, these feature extraction processes are performed automatically based on specific data sets (data-driven) using a machine learning model. The weakness of this approach is that a lot of data will be needed to train the model, and the

user may not be able to be interpreted or described the extracted attributes. Several proven examples of machine learning tools used for feature extraction include CNN [21, 22], autoencoder [22 - 24], or principal component analysis [25 - 27].

Feature extraction based on statistical theory is a classic and commonly used method in data studies. Statistical methods will usually be used first in surveying and understanding system performance trends from sensor data. Statistical methods can be performed in three types [27]: time domain, frequency domain, and time-frequency domain. Statistical methods in the time domain include monotony, trend, consistency, similarity, stability, or correlation. Many techniques can be used to extract these features, including peak value, the difference between the highest and the lowest values, mean absolute value, root mean square (RMS), crest factor, standard deviation, kurtosis, or distributed shape factor. The feature extraction of the time domain technique have many advantages - it is fast, simple, and can be used for many different types of device failures. The disadvantage of time-domain feature extraction is that it is susceptible to noise and often requires data pre-processing before extraction. The advantage of feature extraction in the frequency domain technique is its efficiency in representing anomaly information and equipment errors, which are not visible in the time domain. The disadvantage of the frequency domain technique is the need for specialised knowledge of device failures in the frequency domain, and this method cannot be universally applicable to all types of devices. The time-frequency domain technique is a powerful tool that allows analysing and representing essential features of the data spectrum over time. Time-frequency domain feature extraction method is generally not affected by noise. However, some of its disadvantages are high computational cost, and the difficulty in determining the parameters of the data transformation process from the original time domain to the time-frequency domain. Statistical approaches have been widely applied in predictive intelligence problems and achieved many positive results [28, 29].

After collecting these values, we can do one more step called feature fusion or feature aggregation. This step combines the features extracted from the above statistical method to create more complex features with better data representation. For example, we can use other mathematical formulas [28] or genetic algorithms [29] to combine features.

3.2. Health indicator construction

After extracting the features, the next step is to determine the health indicator. Indeed, a health indicator represents the health state of machinery in real-time, taking into account different kinds of condition monitoring signals, such as vibration, current, and acoustic emission signals. HI construction plays a significant role in PdM. A suitable HI can help simplify the prognostic modelling and produce a more accurate prediction. In addition, from the HI information, specific methods can be devised for estimating the remaining useful life of the device. HI can be derived from monitoring signals using statistical methods or signal processing methods, such as RMS of vibration signals. In fact, machines are often monitored by multiple sensors. While analysing a high-dimensional dataset, different AI techniques can be employed to fuse those multi-sensor signals into an indicator representing the machinery's degradation trend.

In a study by Lei et al. in 2018, there are two main techniques to develop the HI [30], including (i) physical HI (PHI) relating to physical faults of the machine and usually extracted from the sensor using statistical or data processing techniques; (ii) virtual HI (VHI) built by combining many physical indicators or the different sensors. VHI usually carries no physical implication about the device but only information about the failure tendency of the device in a virtual manner.

Principal component analysis (PCA) is one of the most popular techniques for HI construction. PCA is a linear dimension reduction technique that uses an orthogonal transformation to convert a set of observations of possibly correlated or dependent variables into a set of linearly uncorrelated variables called principal components. Some of the significant studies are the construction of an HI using PCA to reduce the dimensions of the feature sets and subsequently calculate the deviations between unknown states and the healthy state [25], using PCA combined with isometric feature mapping to construct an HI for cutting tools [26], and fusing multiple features to calculate the T^2 statistics as an HI of bearings [27].

Self-organising map (SOM) is another widely used technique for HI construction. The SOM is a non-supervised learning neural network that produces a low-dimensional representation of a higher-dimensional dataset by organising itself according to the nature of the input data. The SOM technique was introduced into HI construction by Qiu et al. [31] for the condition

monitoring of roller bearing. Some authors also used the SOM technique for HI construction. Hong et al. [32] used wavelet packet decomposition (WPD) and empirical mode decomposition (EMD) to extract entropy sequences from original vibration signals and use them as input vectors of the SOM network. The confidence value derived from the SOM is then used as an HI of bearing. Lei et al. [33] trained the SOM by the feature vector in the operational stage. Then the feature vector under an unidentified condition is compared with the weight vector of its best matching unit (BMU) in the SOM. Liao et al. [34] used the Restricted Boltzmann Machine algorithm to extract features from the dataset and compare them with the weight vectors of all the units in the baseline map. The distance to the baseline map is calculated as minimum quantisation error (MQE), used as the machine's health value. And Huang et al. [35] trained the SOM network using 6 vibration features and used the MQE indicator derived from SOM as an HI.

Mahalanobis distance (MD) is used in some publications as an HI construction technique. MD generalises multivariate dataset by finding how many standard deviations away a point is from the mean of the multivariate distribution. Wang et al. [36] utilised Mahalanobis distance to construct HI from 14 different statistics into a new feature to reflect the degradation of the bearing. Jin et al. [37] calculated the energies of wavelet coefficients and fused them by calculating their Mahalanobis distance with reference to the healthy one. Kumar et al. [38] also constructed an HI based on Mahalanobis distance to monitor bearings.

Researchers also explored different combinations of AI techniques for HI construction. Ocak et al. [39] used the wavelet packet decomposition (WPD), a time-frequency domain technique, in connection with the hidden Markov modelling (HMM) technique to develop a method for real-time tracking of bearing health and prognostic. HMM has also been successfully applied to many other fields, such as tool wear condition monitoring [40] and bearing diagnosis [41]. Shen et al. [42] constructed an HI that reflects the running state of the rolling bearing in real-time and effectively guarantees the operation reliability of bearings using the fuzzy support vector data description (FSVDD) technique. Liu et al. [43] proposed an HI for bearings through phase space reconstitution combined with approximate diagonalisation of eigen-matrices. Guo et al. [44] constructed an HI that contains rich degradation signatures of bearings from six related-similarity features

and eight time-frequency features using the recurrent neural network.

Besides using mathematical functions to define HI, another way is to compare the current state of the device to be monitored to that of a similar one. The selected devices are also working in the same environment and performing the same task. When the operating envelope of the two devices is the same, their HI will be the same.

3.3. Health stage division

Staged machine operation is the next step after determining HI. However, it is not always easy to separate the working states of the machine. In particular, if the device continuously works with a linear HI from start to finish, it is impossible to subdivide the device's different working stages. In that case, the working state of the device changes uniformly at a constant rate [30]. However, it does not mean that this is an unimportant step in the PdM application. With many other types of mechanical devices (such as journal bearings), the operating state of the equipment can be divided into two or more stages. With these devices, in the healthy stage, the HI readings are nearly constant, so there is no information about the failure trend of the device. Forecasting the RUL at this stage would be neither accurate nor necessary. RUL forecasting should only begin to be performed after the machine transitions from normal operation to deterioration due to failure or a so-called unhealthy state. Then, the division of working states makes sense and is used to determine the device's initial degradations and provide a reasonable transition time for the RUL estimation in PdM.

HI's of machinery generally present varying degradation trends with the development of fault severity. Subsequently, the degradation process of machinery can be divided into different health stages (HS) according to the varying trends of HI. HS division is vital in machinery health diagnostics because it identifies the start time of the unhealthy stage, also known as the first predicting time (FPT), and triggers the remaining useful life (RUL) prediction [20].

In one-stage HS, the health of machinery shows gradual degradation, which can be described using a single degradation model. In this case, the HS division process is not required. In two-stage HS, the degradation trend shows two distinct stages: the healthy stage, where no fault occurs, and the unhealthy stage, where there is an accelerated degradation trend over time. In multiple-stage HS, the

unhealthy equipment stage is further divided into different stages according to the characteristics of degradation trends. HS division can classify the degradation process into one stage, two stages, multiple stages (Figure 3).

The most straightforward approach in HS division is to identify whether the HI exceeds a constant alarm threshold. However, using a constant alarm threshold may yield false alarms due to random noise interference [20]. Some publications used a clustering algorithm to derive an adaptive threshold to avoid this problem. A commonly used algorithm is K-nearest neighbor (KNN), a data classification approach that estimates how likely a data point is to be a member of one group or the other depending on what group the data points nearest to it are in a study by Ramasso et al. [44]. KNN is used to assess the system's discrete state (functioning mode) while using a multidimensional degradation signal. Other AI classification algorithms are also studied in different publications. Kamran et al. [46] developed a model using a fuzzy c-mean clustering algorithm that can adaptively estimate the health state of the system rather than with a fixed number of states. Liu et al. [47] trained a model by applying PCA to reduce the dataset dimension and then using fuzzy c-means to automatically extract knowledge about health state labels of all the time points. Scanlon et al. [48] used a K-means clustering algorithm to determine the boundaries between different states.

The multi-stage degradation processes can also be described using discrete state transition models such as the hidden Markov model (HMM). The hidden Markov model is a probabilistic model attempting to explain or derive the probabilistic characteristic of any random process. It says that an observed event will not correspond to its step-

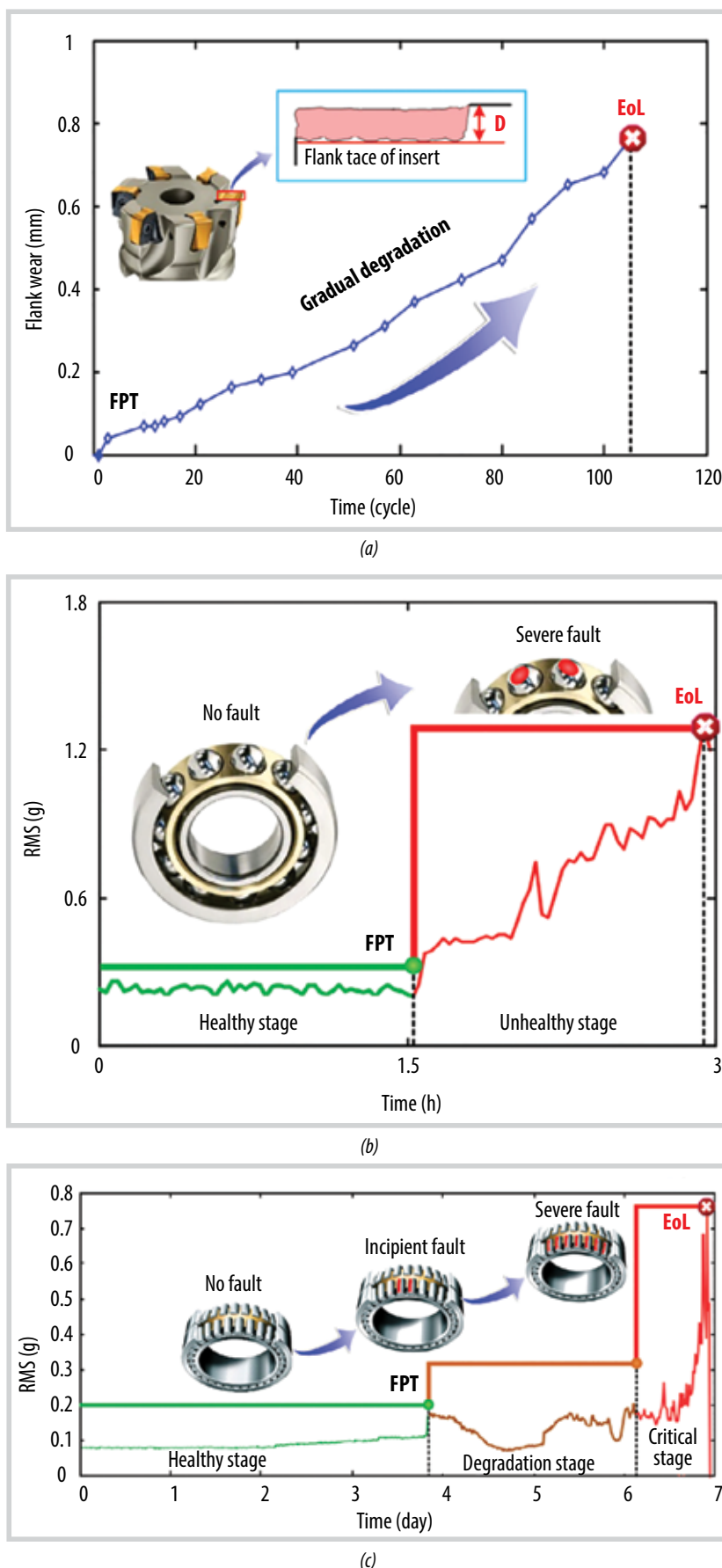


Figure 3. Degradation processes with (a) one stage, (b) two stages, and (c) multiple stages [20].

by-step status but a set of probability distributions. HMM is also applied in the studies of Giantomassi et al. [49], Ramasso et al. [50], and Sloukia et al. [51]. Some AI classifiers are applied to multi-stage HS division as well, such as artificial neural networks [52 - 54] and support vector machine [55, 56].

3.4. Remaining useful life prediction

Prediction of the remaining useful life (RUL) of machinery is the most critical problem in the field of PdM. The RUL of machinery is defined as “the length from the current time to the end of the useful life” [57]. The primary task of RUL prediction is to forecast the time left before the machinery loses its operation ability based on the condition monitoring information. It is the last technical process as well as the last goal of machinery prognostics. Approaches for RUL prediction can be categorised into physical model-based approaches, statistical model-based approaches, and AI approaches.

Physical model-based is a classical approach that describes degradation processes of machinery through building mathematical models based on the failure mechanisms or the first principal damage [58]. The parameters of the physical models reflect the material properties and stress levels, which are generally obtained by experiments or finite element analysis. To provide an accurate estimation of the RUL physical model-based approach, it is required that the model is developed with a complete understanding of the failure mechanisms and effective estimation of model parameters. However, it is difficult for some complex mechanical systems to understand the physics the damage, which restricts the application of these approaches [20].

Statistical model-based approaches, also known as empirical model-based approaches, estimate the RUL of machinery by establishing statistical models based on empirical knowledge [57]. The statistical model-based approach does not rely on physics to construct RUL prediction models. Rather, the RUL is predicted by fitting available observations into random coefficient models or stochastic process models under a probabilistic method. In the RUL problem, this method uses probabilistic statistical models to represent the relationship between variables in the state of the device. Random variances are generally introduced into model parameters to describe the uncertainties caused by different kinds of variability sources, such as temporal variability, unit-to-unit

variability, and measurement variability [59]. Therefore, the statistical model-based approaches effectively describe the uncertainty of degradation process and its influence on RUL prediction.

AI approaches attempt to learn the machinery degradation patterns using AI techniques from available observations instead of building physical models or statistical models. They can deal with prognostic issues of complex mechanical systems whose degradation processes are challenging to be interrelated by physical models or statistical models. Therefore, they are attracting more and more attention in the field of machinery prognostics. The results of AI approaches are hard to explain because of the lack of transparency; thus, these techniques are consistently named “black boxes” [20]. The commonly used AI techniques in machinery prognostics include artificial neural networks, neuro-fuzzy systems, support vector machine, K-nearest neighbour, and Gaussian process regression (GPR), etc.

The artificial neural network is an ML reasoning technique inspired by the working process of human brains. It is a collection of nodes, also known as artificial neurons, in a complex structure of the input, hidden, and output layers. In ANNs, different layers may perform different transformations on their inputs. Input layer nodes pass information to hidden layer nodes by activation functions. Subsequently, the hidden layers apply weighting functions until some threshold of the hidden layer is reached. Finally, the result is passed to the output layer. Because ANNs can learn complex non-linear relationships by training the multi-layer networks, they have a good performance in dealing with complex systems and become the most used AI techniques in machinery RUL prediction. Two widely used ANNs are feed-forward neural network and recurrent neural network, which are classified based on the architecture of layers in the network. The difference is illustrated in Figure 4.

The feed-forward neural network (FFNN) is a class of ANNs, where inputs are processed forward. Sbarufatti et al. [60] combined FFNNs with sequential Monte-Carlo sampling to predict the RUL of fatigue cracks. Pan et al. [61] and Xiao et al. [62] used an FFNN to conduct multi-step ahead prediction for the bearing health states. Wang et al. [63] used a three-layer FFNN to predict the future HIs and input the predicted HIs into a PH model to estimate the hazard rate and survival probability. The results showed that RUL can be predicted with high accuracy in the

incipient degradation phase and trace the degradation well with a limited amount of data.

On the other hand, the recurrent neural network (RNN) is another class of ANNs that have many applications in solving time-series or sequential data problems. Unlike FFNN, which assumes inputs and outputs are independent, RNN has a recurrent connection in the hidden state that makes the output of RNN depend on the prior or previous elements within the sequence. RNN method is widely used in RUL prediction because of its ability to deal with detailed time-series data. As illustrated in many studies, this method showed good performance, such as the recurrent radial basis function network to predict the RUL of machinery by Zemouri [64]. Malhi et al. developed a competitive learning-based approach to revise the training technique of RNNs that helps improve the long-term prediction accuracy [65]. In addition, Peng et al. improved the RNN model by replacing a hidden layer using a large sparse reservoir to develop a new RUL prediction approach [66]. Liu et al. proposed an enhanced RNN for RUL prediction by improving RNNs' memory property [67].

The ANN networks still have limitations in terms of their low transparency and the requirement of a large dataset for high-quality training process, which are difficult to capture in industrial applications. In addition, their structures and parameters are generally initialised randomly or specified manually, which reduces their generalisation ability among different cases [20].

The neural fuzzy (NF) approach is based on the

fuzzy system trained by algorithms derived from neural networks. The basic idea behind this NF system is that it combines the human-like reasoning style of fuzzy systems with neural networks' learning and connectionist structure [69]. The NF-based time-series forecasting approach was proposed by Jang et al. [70]. Wang et al. [71] adopted the NF system to develop an online prognostic approach for different kinds of gear faults. Wang [72] further improve this approach from several aspects to enhance its forecasting performance. NF systems take advantage of both the expert knowledge and the intelligent ANNs, thus being competitive candidates for machinery RUL prediction [73 - 77]. However, they still need lots of high-quality training data.

Support vector machine (SVM) is a kind of ML technique based on the statistical learning theory proposed by Vapnik [78]. Different kinds of SVM have been applied to the RUL prediction of machinery, such as the least square-SVM [79], one-class SVM [80], and multi-class SVM [81]. Widodo et al. [82] trained an SVM model using both the censored and the complete data and predicted the survival probability of machinery. Tran et al. [83] integrated an SVM-based RUL prediction module into an intelligent condition-based maintenance platform. In addition, support vector regression (SVR) is the standard application form of SVM in prognostics [83]. Benkedjouh et al. [84] used the SVR to map the HIs into non-linear regressions and then fitted the obtained regressions into power models for RUL prediction of machinery. Liu et al. [85] developed a modified probabilistic SVR to predict the degradation processes of nuclear power plant

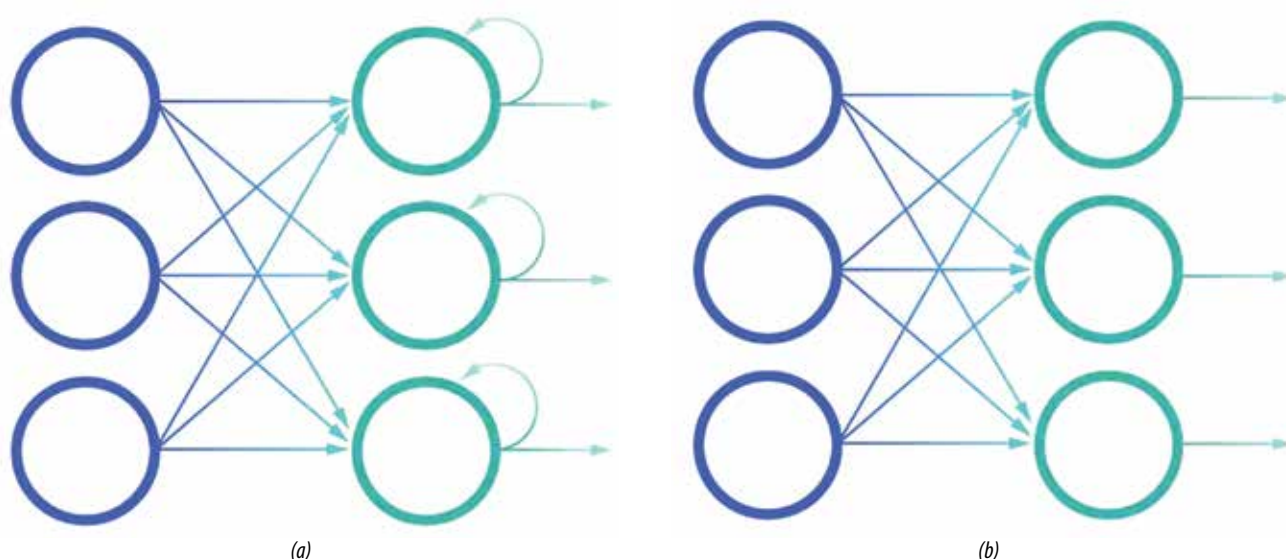


Figure 4. Comparison of RNN (a) and FFNN (b) [68].

components. Fumeo et al. [86] developed an online SVR model for the RUL prediction of bearings by optimising the trade-off between accuracy and the computing efficiency.

Compared to ANNs, SVM are superior in dealing with the issues of small sample sizes. Thus, they may be more suitable for the issues of RUL prediction where only limited measurements are available. However, the performance of SVM is highly dependent on the selected kernel functions and parameter optimisation process.

Gaussian process regression (GPR) is an ML technique that implements Gaussian processes for regression purposes [87]. Gaussian processes are cumulative damage processes of random variables with joint multivariate Gaussian distributions. Many regression models have been published recently, such as introducing theoretical details and the flexibility of the GPR in non-linear regression [88], predicting RUL by GPR [89], applying GPR with three different covariance functions for RUL prediction of bearings [32] and predicting the degradation trends of rolling element bearings using an integrated GPR model [90]. In contrast to the above AI techniques, GPR is highly adaptable and suitable for RUL prediction problem of high-dimension and small-size datasets [91]. The major drawback of GPR is that it generally requires heavy computational work.

3.5. Challenges for PdM using ML in Vietnam

In essence, each device has many different failure modes and must be tested in laboratory to produce the most complete and standard datasets. During normal operating conditions, these figures are difficult to obtain. There can only be specific failure modes. In addition, it is necessary to aggregate data on equivalent machines. It is challenging to compare and synthesise data in many cases due to the unavailability of machines in most companies. Where possible, oil and gas companies, especially in Vietnam, need to collaborate and share data about machinery to support the development and research of PdM.

Infrastructure for data acquisition is not enough due to high installation and maintenance costs. Instrumentation is often poorly equipped or does not have a proper acquisition system to collect data for a long time. Moreover, special data acquisition equipment such as vibration analyser, ultrasonic sound measurement, and oil sampling analyser is typically expensive, dependent

on advanced technology or requiring intensive training to use. Recently, PdM applications often used AI and ML. Due to the lack of specialised research facilities for PdM in Vietnam, there will be many difficulties and challenges for the technology to be applied in the country. However, the benefits it brings if successfully implemented are very desirable.

4. Conclusion

PdM practices become more and more popular in many industrial sectors because of their effectiveness in reducing unnecessary maintenance operations and improving machinery reliability. With the recent advancement of Industry 4.0, ML has found wide applications in PdM practice to assist humans in processing, continuously monitoring and analysing equipment's health. This paper has discussed the practice of PdM and reviewed the applications of some state-of-the-art AI techniques that have been studied in this field. Different AI techniques are structurally discussed in the four technical steps of the machinery health prognostics process, including data acquisition, HI construction, HS division, and RUL prediction.

BIENDONG POC is aiming to deploy PdM solutions for monitoring, maintaining, and tracking equipment's reliability and performance in a plant by ML modelling. The monitoring and quick identification of failures help make decisions and plans for maintenance and enable support for continuous performance, health surveillance, and focus on performance degradation as a leading indicator of potential equipment problems. Therefore, it is necessary to review research achievements and trends in PdM to assess the current status and orientate the focus of research at BIENDONG POC.

5. Acknowledgement

This research work is described herein as part of the government research project number 077.2021.CNKK. QG/HĐKH-CN, order 196/QĐ-BCT of Vietnam Ministry of Industry and Trade, Viet Nam.

References

- [1] BS EN 1336:2017, "Maintenance - Maintenance terminology", 2017.
- [2] Raghu Raj, "How preventive maintenance can backfire and harm your assets", 2020. [Online]. Available:

https://www.ey.com/en_gl/consulting/how-preventive-maintenance-can-backfire-and-harm-your-assets.

[3] Tomasz Nowakowski, Agnieszka Tubis, and Sylwia Werbińska-Wojciechowska, "Evolution of technical systems maintenance approaches-review and a case study", *International Conference on Intelligent Systems in Production Engineering and Maintenance*. Springer, 2018, pp. 161 - 174.

[4] Tran Vu Tung, Tran Ngoc Trung, Ngo Huu Hai, and Nguyen Thanh Tinh, "Digital transformation in oil and gas companies - A case study of Bien Dong POC", *Petrovietnam Journal*, Vol. 10, pp. 67 - 78, 2020. DOI: 10.47800/PVJ.2020.10-07.

[5] Trần Ngọc Trung, Trần Vũ Tùng, Hoàng Kỳ Sơn, Ngô Hữu Hải và Đào Quang Khoa, "Thực tiễn triển khai nền tảng số hóa tập trung tại mỏ Hải Thạch - Mộc Tinh", *Tạp chí Dầu khí*, Số 12, trang 47 - 56, 2020. DOI: 10.47800/PVJ.2020.12-06.

[6] Rebecca Smith-Bindman, Philip Chu, Diana Lynn Miglioretti, Chris Quale, Robert Daniel Rosenberg, Gary Cutter, Berta Geller, Peter Bacchetti, Edward A. Sickles, and Karla Kerlikowske, "Physician predictors of mammographic accuracy", *Journal of the National Cancer Institute*, Vol. 97, No. 5, pp. 358 - 367, 2005. DOI: 10.1093/jnci/dji060.

[7] Varun Gulshan, Lily Peng, Marc Coram, Martin C. Stumpe, Derek Wu, Arunachalam Narayanaswamy, Subhashini Venugopalan, Kasumi Widner, Tom Madams, Jorge Cuadros, Ramasamy Kim, Rajiv Raman, Philip C. Nelson, Jessica L. Mega, and Dale R. Webster, "Development and validation of a deep learning algorithm for detection of diabetic retinopathy in retinal fundus photographs", *JAMA*, Vol. 316, No. 22, pp. 2402 - 2410, 2016. DOI: 10.1001/jama.2016.17216.

[8] Bruce I. Reiner and Elizabeth Krupinski, "The insidious problem of fatigue in medical imaging practice", *Journal of Digital Imaging*, Vol. 25, No. 1, pp. 3 - 6, 2012. DOI: 10.1007/s10278-011-9436-4.

[9] Won Shin, Jeongyun Han, and Wonjong Rhee, "AI-assistance for predictive maintenance of renewable energy systems", *Energy*, Vol. 221, 2021. DOI: 10.1016/j.energy.2021.119775.

[10] Roosefert Mohan T., Preetha Roselyn J., Annie Uthra R., Devaraj D., and Umachandran K., "Intelligent machine learning based total productive maintenance

approach for achieving zero downtime in industrial machinery", *Computer & Industrial Engineering*, Vol. 157, 2021.

[11] M.Waqar Akramad, Guiqiang Li, Yi Jin, Xiao Chen, Changan Zhu, Xudong Zhao, Abdul Khaliq, M.Faheem, and Ashfaq Ahmad, "CNN based automatic detection of photovoltaic cell defects in electroluminescence images", *Energy*, Vol. 189, 2019. DOI: 10.1016/j.energy.2019.116319.

[12] Shaoqing Ren, Kaiming He, Ross Girshick, and Jian Sun, "Faster R-CNN: Towards real-time object detection with region proposal networks", *IEEE Transactions on Pattern Analysis and Machine Intelligence*, Vol. 39, pp. 1137-1149, 2017. DOI: 10.1109/TPAMI.2016.2577031.

[13] Young-Jin Cha, Wooram Choi, Gahyun Suh, Sadegh Mahmoudkhani, and Oral Büyükoztürk, "Autonomous structural visual inspection using region-based deep learning for detecting multiple damage types", *Computer-Aided Civil and Infrastructure Engineering*, Vol. 33, No. 9, pp. 731 - 747, 2018. DOI: doi/10.1111/mice.12334.

[14] Wenbin Wang, Matthew J. Carr, Tommy Wai Shing Chow, and Michael G. Pecht, "A two-level inspection model with technological insertions", *IEEE Transactions on Reliability*, Vol. 61, pp. 479 - 490, 2012. DOI: 10.1109/TR.2012.2183911.

[15] Sule Selcuk, "Predictive maintenance, its implementation and latest trends", *Journal of Engineering Manufacture*, Vol. 231, No. 9, pp. 1670 - 1679, 2017. DOI: 10.1177/0954405415601640.

[16] R. Keith Mobley, Lindley R. Higgins, and Darrin J. Wikoff, *Maintenance engineering handbook*, 7th edition. McGraw-Hill Education, 2008.

[17] PwC, "Predictive maintenance 4.0 - Beyond the hype: PdM 4.0 delivers results", 2018. [Online]. Available: <https://www.pwc.de/de/industrielle-produktion/pwc-predictive-maintenance-4-0.pdf>.

[18] Valerio Dilda, Lapo Mori, Olivier Noterdaeme, and Christoph Schmitz, "Manufacturing: Analytics unleashes productivity and profitability", 2017. [Online]. Available: <https://www.mckinsey.com/business-functions/operations/our-insights/manufacturing-analytics-unleashes-productivity-and-profitability>.

[19] Knud Lasse Lueth, "Predictive maintenance initiatives saved organizations \$17B in 2018, as the number of vendors surges", 2019. [Online]. Available: <https://>

iot-analytics.com/numbers-of-predictive-maintenance-vendors-surges/.

[20] Yaguo Lei, Naipeng Li, Liang Guo, Ningbo Li, Tao Yan, and Jing Lin, "Machinery health prognostics: A systematic review from data acquisition to RUL prediction", *Mechanical Systems and Signal Processing*, Vol. 104, pp. 799 - 834, 2018. DOI: 10.1016/j.ymssp.2017.11.016.

[21] Rui Zhao, Ruqiang Yan, Jinjiang Wang, and Kezhi Mao, "Learning to monitor machine health with convolutional bi-directional LSTM networks", *Sensors*, Vol. 17, No. 2, pp. 273, 2017. DOI: 10.3390/s17020273.

[22] Ling Xiang, Penghe Wang, Xin Yang, Aijun Hu, and Hao Su, "Fault detection of wind turbine based on SCADA data analysis using CNN and LSTM with attention mechanism", *Measurement*, Vol. 175, No. 8, 2021. DOI: 10.1016/j.measurement.2021.109094.

[23] Pankaj Malhotra, Lovekesh Vig, Gautam Shroff, and Puneet Agarwal, "Long short term memory networks for anomaly detection in time series", *23rd European Symposium on Artificial Neural Networks, Computational Intelligence and Machine Learning (ESANN), Bruges, Belgium, 2015*.

[24] Pankaj Malhotra, Anusha Ramakrishnan, Gaurangi Anand, Lovekesh Vig, Puneet Agarwal, and Gautam Shroff, "LSTM-based encoder-decoder for multi-sensor anomaly detection", 2016. [Online]. Available: <https://arxiv.org/pdf/1607.00148.pdf>.

[25] Achmad Widodo and Bo-Suk Yang, "Application of relevance vector machine and survival probability to machine degradation assessment", *Expert Systems with Applications*, Vol. 38, No. 3, pp. 2592 - 2599, 2011. DOI: 10.1016/j.eswa.2010.08.049.

[26] Tarak Benkedjough, Kamal Medjaher, Nouredine Zerhouni, and Said Rechak, "Health assessment and life prediction of cutting tools based on support vector regression", *Journal of Intelligent Manufacturing*, Vol. 26, No. 2, pp. 213 - 223, 2015. DOI: 10.1007/s10845-013-0774-6.

[27] Tianyi Wang, "Bearing life prediction based on vibration signals: A case study and lessons learned", *IEEE Conference on Prognostics and Health Management, Beijing*, 2012. DOI: 10.1109/ICPHM.2012.6299547.

[28] Yuanhong Chang, Jinglong Chen, Haixin Lv, and Shen Liu, "Heterogeneous bi-directional recurrent neural network combining fusion health indicator for predictive

analytics of rotating machinery", *ISA Transactions*, 2021. DOI: 10.1016/j.isatra.2021.04.024.

[29] Khanh T. P. Nguyen and Kamal Medjaher, "An automated health indicator construction methodology for prognostics based on multi-criteria optimization", *ISA Transactions*, Vol. 113, pp. 81 - 96, 2021. DOI: 10.1016/j.isatra.2020.03.017.

[30] Yaguo Lei, Naipeng Li, Liang Guo, Ningbo Li, Tao Yan, and Jing Lin, "Machinery health prognostics: A systematic review from data acquisition to RUL prediction", *Mechanical Systems and Signal Processing*, Vol. 104, pp. 799 - 834, 2018. DOI: 10.1016/j.ymssp.2017.11.016.

[31] Jay Lee, Hai Qiu, Jing Lin, and Gang Yu, "Robust performance degradation assessment methods for enhanced rolling element bearing prognostics", *Advanced Engineering Informatics*, Vol. 17, No. 3 - 4, pp. 127 - 140, 2003. DOI: 10.1016/j.aei.2004.08.001.

[32] Zheng Zhou, Sheng Hong, Enrico Zio, and Kan Hong, "Condition assessment for the performance degradation of bearing based on a combinatorial feature extraction method", *Digital Signal Processing*, Vol. 27, pp. 159 - 166, 2014. DOI: 10.1016/j.dsp.2013.12.010.

[33] Yaguo Lei, Naipeng Li, Szymon Gontarz, Jing Lin, Stanislaw Radkowski, and Jacek Dybala, "A model-based method for remaining useful life prediction of machinery", *IEEE Transactions on Reliability*, Vol. 65, No. 3, pp. 1314 - 1326, 2016. DOI: 10.1109/TR.2016.2570568.

[34] Linxia Liao, Radu Pavel, and Wenjing Jin, "Enhanced restricted Boltzmann machine with prognosability regularization for prognostics and health assessment", *IEEE Transactions on Industrial*, Vol. 63, No. 11, pp. 7076 - 7083, 2016. DOI: 10.1109/TIE.2016.2586442.

[35] Runqing Huang, Lifeng Xi, Xinglin Li, C. Richard Liu, Hai Qiu, and Jay Lee, "Residual life predictions for ball bearings based on self-organizing map and back propagation neural network methods", *Mechanical Systems and Signal Processing*, Vol. 21, No. 1, pp. 193 - 207, 2007. DOI: 10.1016/j.ymssp.2005.11.008.

[36] Yu Wang, Yizhen Peng, Zi, Yanyang Zi, Xiaohang Jin, and Kwok-Leung Tsui, "A two-stage data-driven-based prognostic approach for bearing degradation problem", *IEEE Transactions on Industrial Informatics*, Vol. 12, No. 3, pp. 924 - 932, 2016. DOI: 10.1109/TII.2016.2535368.

[37] Xiaohang Jin, Yi Sun, Zijun Que, Yu Wang, and Tommy Wai Shing Chow, "Anomaly detection

and fault prognosis for bearings", *IEEE Transactions on Instrumentation and Measurement*, Vol. 65, pp. 2046 - 2054, 2016. DOI: 10.1109/TIM.2016.2570398.

[38] Kumar H S, P. Srinivasa Pai, N. S. Sriram, and Vijay Gs, "Rolling element bearing fault diagnostics: Development of health index", *Proceedings of the Institution of Mechanical Engineers, Part C: Journal of Mechanical Engineering Science 1989 - 1996*, Vol. 231, No. 21, pp. 3923 - 3939, 2017. DOI: 10.1177/0954406216656214.

[39] Hasan Ocak, Kenneth A. Loparo, Fred M. Discenzo, "Online tracking of bearing wear using wavelet packet decomposition and probabilistic modeling: A method for bearing prognostics", *Journal of Sound and Vibration*, Vol. 302, No. 4 - 5, pp. 951 - 961, 2007. DOI: 10.1016/j.jsv.2007.01.001.

[40] Huseyin M. Ertunc, Kenneth A. Loparo, Hasan Ocak, "Tool wear condition monitoring in drilling operations using hidden Markov models (HMMs)", *International Journal of Machine Tools and Manufacture*, Vol. 41, No. 9, pp. 1363 - 1384, 2001. DOI: 10.1016/S0890-6955(00)00112-7.

[41] Hasan Ocak and Kenneth A. Loparo, "HMM-based fault detection and diagnosis scheme for rolling element bearings", *Journal of Vibration and Acoustics*, Vol. 127, No. 4, pp. 299 - 306, 2005. DOI: 10.1115/1.1924636.

[42] Zhongjie Shen, Zhengjia He, Xuefeng Chen, Chuang Sun, and Zhiwen Liu, "A monotonic degradation assessment index of rolling bearings using fuzzy support vector data description and running time", *Sensors*, Vol. 12, No. 8, pp. 10109 - 10135, 2012. DOI: 10.3390/s120810109.

[43] Yan-Cheng Liu, Siyuan Liu, and Ning Wang, "Fully-tuned fuzzy neural network based robust adaptive tracking control of unmanned underwater vehicle with thruster dynamics", *Neurocomputing*, Vol. 196, pp. 1 - 13, 2016. DOI: 10.1016/j.neucom.2016.02.042.

[44] Guo Liang, Li Naipeng, Jia Feng, Lei Yaguo, and Lin Jing, "A recurrent neural network based health indicator for remaining useful life prediction of bearings", *Neurocomputing*, Vol. 240, pp. 98 - 109, 2017. DOI: 10.1016/j.neucom.2017.02.045.

[45] Emmanuel Ramasso, Michèle Rombaut, and Nouredine Zerhouni, "Joint prediction of continuous and discrete states in time-series based on belief functions", *IEEE Transactions on Cybernetics*, Vol. 43, No. 1, pp. 37 - 50, 2013.

[46] Kamran Javed, Rafael Gouriveau, and Nouredine Zerhouni, "A new multivariate approach for prognostics based on extreme learning machine and fuzzy clustering", *IEEE Transactions on Cybernetics*, Vol. 45, No. 12, pp. 2626 - 2639, 2015. DOI: 10.1109/TCYB.2014.2378056.c

[47] Zhilian Liu, Ming J. Zuo, and Yong Qin, "Remaining useful life prediction of rolling element bearings based on health state assessment", *Proceedings of the Institution of Mechanical Engineers, Part C: Journal of Mechanical Engineering Science*, Vol. 230, No. 2, pp. 314 - 330, 2016. DOI: 10.1177/0954406215590167.

[48] Patricia Scanlon, Darren F. Kavanagh, and Francis Boland, "Residual life prediction of rotating machines using acoustic noise signals", *IEEE Transactions on Instrumentation and Measurement*, Vol. 62, pp. 95 - 108, 2012. DOI: 10.1109/TIM.2012.2212508.

[49] Andrea Giantomassi, Francesco Ferracuti, Alessandro Benini, Gianluca Ippoliti, Sauro Longhi, and Antonio Petrucci, "Hidden Markov model for health estimation and prognosis of turbofan engines", *ASME 2011 International Design Engineering Technical Conferences and Computers and Information in Engineering Conference*, 28 - 31 August, 2011. DOI: 10.1115/DETC2011-48174.

[50] E. Ramasso and T. Denoeux, "Making use of partial knowledge about hidden states in HMMs: An approach based on belief functions", *IEEE Transactions on Fuzzy Systems*, Vol. 22, pp. 395 - 405, 2014.

[51] F. Sloukia, R. Bouarfa, H. Medromi, and M. Wahbi, "Bearings prognostic using mixture of Gaussians hidden Markov model and support vector machine", *International Journal of Network Security & Its Applications*, Vol. 5, pp. 85 - 97, 2013.

[52] P. Tamilselvan, Yibin Wang, and P. Wang, "Deep belief network based state classification for structural health diagnosis", *2012 IEEE Aerospace Conference, Montana*, 3 - 10 March, 2012.

[53] Liang Guo, Hongli Gao, Haifeng Huang, Xiang He, and ShiChao Li, "Multifeatures fusion and non-linear dimension reduction for intelligent bearing condition monitoring", *Shock and Vibration*, Vol. 2016, pp. 1 - 10, 2016. DOI: 10.1155/2016/4632562.

[54] Jaouher Ben Ali, Brigitte Chebel-Morello, Lotfi Saidi, Simon Malinowski, and Farhat Fnaiech, "Accurate bearing remaining useful life prediction based on Weibull distribution and artificial neural network", *Mechanical*

Systems and Signal Processing, Vol. 56 - 57, pp. 150 - 172, 2015.

[55] A. Soualhi, K. Medjaher, and N. Zerhouni, "Bearing health monitoring based on Hilber-Huang transform, support vector machine, and regression", *IEEE Transactions on Instrumentation and Measurement*, Vol. 64, pp. 52 - 62, 2015.

[56] Hack-Eun Kim, Andy C.C. Tan, Joseph Mathew, and Byeong-Keun Choi, "Bearing fault prognosis based on health state probability estimation", *Expert Systems with Application*, Vol. 39, pp. 5200 - 5213, 2012.

[57] Xiao-Sheng Si, Wenbin Wang, Chang-Hua Hu, Dong-Hua Zhou, "Remaining useful life estimation - A review on the statistical data driven approaches", *European Journal of Operational Research*, Vol. 213, pp. 1 - 14, 2011.

[58] Y. Li, S. Billington, C. Zhang, T. Kurfess, S. Danyluk, and S. Liang, "Adaptive prognostics for rolling element bearing condition", *Mechanical Systems and Signal Processing*, Vol. 13, No. 1, pp. 103 - 113, 1999.

[59] Yaguo Lei, Naifei Li, and Jing Lin, "A new method based on stochastic process models for machine remaining useful life prediction", *IEEE Transactions on Instrumentation and Measurement*, Vol. 65, pp. 2671 - 2684, 2016.

[60] C. Sbarufatti, M. Corbetta, A. Manes, and M. Giglio, "Sequential Monte-Carlo sampling based on a committee of artificial neural networks for posterior state estimation and residual lifetime prediction", *International Journal of Fatigue*, Vol. 83, pp. 10 - 23, 2016.

[61] Yongping Pan, Meng Joo Er, Xiang Li, Haoyong Yu, and Rafael Gouriveau, "Machine health condition prediction via online dynamic fuzzy neural networks", *Engineering Applications of Artificial Intelligence*, Vol. 35, pp. 105 - 113, 2014.

[62] Lei Xiao, Xiaohui Chen, Xinghui Zhang, and Min Liu, "A novel approach for bearing remaining useful life estimation under neither failure nor suspension histories condition", *Journal of Intelligent Manufacturing*, Vol. 28, pp. 1893 - 1914, 2017. DOI: 10.1007/s10845-015-1077-x.

[63] Lu Wang, Li Wang, Xue-zhi Wang, "Reliability estimation and remaining useful lifetime prediction for bearing based on proportional hazard model", *Journal of Central South University*, Vol. 22, pp. 4625 - 4633, 2015.

[64] Ryad Zemouri and Rafael Gouriveau, "Towards accurate and reproducible predictions for prognostic:

An approach combining a RRBf network and an autoRegressive model", *IFAC Proceedings Volumes*, Vol. 43, No. 3, pp. 140 - 145, 2010.

[65] Arnaz Malhi, Ruqiang Yan, and Robert X. Gao, "Prognosis of defect propagation based on recurrent neural networks", *IEEE Transactions on Instrumentation and Measurement*, Vol. 60, pp. 703 - 711, 2011. DOI: 10.1109/TIM.2010.2078296.

[66] Yu Peng, Hong Wang, Jianmin Wang, Datong Liu, and Xiyuan Peng, "A modified echo state network based remaining useful life estimation approach", *2012 IEEE Conference on Prognostics and Health Management*, 2012.

[67] Datong Liu, Wei Xie, Haitao Liao, and Yu Peng, "An integrated probabilistic approach to Lithium-Ion battery remaining useful life estimation", *IEEE Transactions on Instrumentation and Measurement*, Vol. 64, pp. 660 - 670, 2015.

[68] IBM Cloud Education, "Recurrent neural networks", 2020. [Online]. Available: <https://www.ibm.com/cloud/learn/recurrent-neural-networks>.

[69] Samarjit Kar, Sujit Das, and Pijush Ghosh, "Applications of neuro fuzzy systems: A brief review and future outline", *Applied Soft Computing*, Vol. 15, pp. 243 - 259, 2014.

[70] Jyh-Shing Roger Jang, Chuen-Tsai Sun, and Eiji Mizutani, *Neuro-fuzzy and soft computing: A computational approach to learning and machine intelligence*. Prentice-Hall Inc., 1996.

[71] Wilson Q. Wang, M. Farid Golnaraghi, and Fathy Ismail, "Prognosis of machine health condition using neuro-fuzzy systems", *Mechanical Systems and Signal Processing*, Vol. 18, No. 4, pp. 813 - 831, 2004. DOI: 10.1016/s0888-3270(03)00079-7.

[72] Wilson Wang, "An adaptive predictor for dynamic system forecasting", *Mechanical Systems and Signal Processing*, Vol. 21, No. 2, pp. 809 - 823, 2007. DOI:10.1016/j.ymsp.2005.12.008.

[73] Fagang Zhao, Jin Chen, Lei Guo, and Xinglin Li, "Neuro-fuzzy based condition prediction of bearing health", *Journal of Vibration and Control*, Vol. 15, No. 7, pp. 1079 - 1091, 2009. DOI:10.1177/1077546309102665.

[74] Van Tung Tran, Bo-Suk Yang, and Andy Chit Chiow Tan, "Multi-step ahead direct prediction for the machine condition prognosis using regression trees and

neuro-fuzzy systems", *Expert Systems with Applications*, Vol. 36, No. 5, pp. 9378 - 9387, 2009. DOI: 10.1016/j.eswa.2009.01.007

[75] Chaochao Chen, Bin Zhang, George Vachtsevanos, and Marcos E.Orchard, "Machine condition prediction based on adaptive neuro-fuzzy and high-order particle filtering", *IEEE Transactions on Industrial Electronics*, Vol. 58, No. 9, pp. 4353 - 4364, 2011.

[76] Daniel Zurita Millan, Jesus A.Carino, Miguel Delgado-Prieto, and Juan Antonio Redondo, "Distributed neuro-fuzzy feature forecasting approach for condition monitoring", *2014 IEEE Emerging Technology and Factory Automation (ETFA)*, 2015.

[77] Sajid Hussain and Hossam A.Gabbar, "Vibration analysis and time series prediction for wind turbine gearbox prognostics", *International Journal of Prognostics and Health Management*, Vol. 4, No. 3, 2013. DOI: 10.36001/ijphm.2013.v4i3.2144.

[78] Vladimir N.Vapnik, "An overview of statistical learning theory", *IEEE transactions on neural networks*, Vol. 10, No. 5, pp. 988 - 999, 1999.

[79] Shaojiang Dong and Tianhong Luo, "Bearing degradation process prediction based on the PCA and optimized LS-SVM model", *Measurement*, Vol. 46, No. 9, pp. 3143 - 3152, 2013. DOI: 10.1016/j.measurement.2013.06.038.

[80] J. Carino, D. Zurita, Miguel Delgado Prieto, J. A. Redondo, and R. Romero-Troncoso, "Remaining useful life estimation of ball bearings by means of monotonic score calibration", *IEEE International Conference on Industrial Technology (ICIT), 17 - 19 March 2015*. DOI: 10.1109/ICIT.2015.7125351.

[81] James K. Kimotho, Christoph Sondermann-Woelke, Tobias Meyer, and Walter Sextro, "Machinery prognostic method based on multi-class support vector machines and hybrid differential evolution particle swarm optimization", *Chemical Engineering Transactions*, Vol. 33, pp. 619 - 624, 2013.

[82] Achmad Widodo and Bo-Suk Yang, "Machine health prognostics using survival probability and support vector machine", *Expert Systems with Applications*, Vol. 38, No. 7, pp. 8430 - 8437, 2011. DOI: 10.1016/j.eswa.2011.01.038.

[83] Van Tung Tran and Bo-Suk Yang, "An intelligent condition-based maintenance platform for rotating machinery", *Expert Systems with Applications*, Vol. 39, No. 3, pp. 2977 - 2988, 2012. DOI:10.1016/j.eswa.2011.08.159.

[84] T. Benkedjouh, K. Medjaher, N. Zerhouni, and S. Rechak, "Health assessment and life prediction of cutting tools based on support vector regression", *Journal of Intelligent Manufacturing*, Vol. 26, pp. 213 - 223, 2015. DOI: 10.1007/s10845-013-0774-6.

[85] Jie Liu and Enrico Zio, "An adaptive online learning approach for support vector regression: online-SVR-FID", *Mechanical Systems and Signal Processing*, Vol. 76, pp. 796 - 809, 2016. DOI: 10.1016/j.ymssp.2016.02.056.

[86] Emanuele Fumeo, Luca Oneto, Davide Anguita, "Condition based maintenance in railway transportation systems based on big data streaming analysis", *Procedia Computer Science*, Vol. 53, pp. 437 - 446, 2015. DOI: 10.1016/j.procs.2015.07.321.

[87] W. J. Padgett and Meredith A. Tomlinson, "Inference from accelerated degradation and failure data based on Gaussian process models", *Lifetime Data Analysis*, Vol. 10, pp. 191 - 206, 2004.

[88] Carl Edward Rasmussen, "Gaussian processes in machine learning", *Advanced Lectures on Machine Learning*, pp. 63 - 71, 2003. DOI: 10.1007/978-3-540-28650-9_4.

[89] Kai Goebel, Bhaskar Saha, and Abhinav Saxena, "A comparison of three data-driven techniques for prognostics", 2008.

[90] S.A. Aye, P.S. Heyns, "An integrated Gaussian process regression for prediction of remaining useful life of slow speed bearings based on acoustic emission", *Mechanical Systems and Signal Processing*, Vol. 84, pp. 485 - 498, 2017. DOI: 10.1016/j.ymssp.2016.07.039.

[91] Man Shan Kan, Andy C.C. Tan, and Joseph Mathew, "A review on prognostic techniques for non-stationary and non-linear rotating systems", *Mechanical Systems and Signal Processing*, Vol. 62 - 63, pp. 1 - 20, 2015. DOI: 10.1016/j.ymssp.2015.02.016

ENERGY INTEGRATION: GREEN FUTURE FOR LATE-LIFE OFFSHORE OIL AND GAS ASSETS

Nguyen Thu Huong¹, Nguyen Thi Thanh Le²

¹Vietnam Petroleum Institute

²Ministry of Industry and Trade

Email: huongnt@vpi.pvn.vn

<https://doi.org/10.47800/PVJ.2021.10-06>

Summary

In recent years, the oil and gas industry has been facing objections from a public greatly concerned with the severe environmental impact caused by fossil fuels and their infrastructures, and strong demands from policy makers seeking to meet decarbonisation goals. Amidst a global energy transition, the future demand, finance, and social responsibilities of oil and gas companies are increasingly in question. One of the biggest problems of the industry is what are the “green” solutions for the late-life offshore oil and gas assets. Energy integration with reusing or repurposing oil and gas assets for new technologies could be a worthwhile investment strategy helping reduce carbon emission from oil and gas production as well as accelerating carbon capture and storage (CCS) and green hydrogen development to support the global decarbonisation. According to research, the late-life offshore oil and gas assets play an important role in energy integration while helping to have more opportunities to develop the new technologies that are in the early stages of development with high capex, necessary to make them more economically attractive and facilitate maximum energy integration. Reusing or repurposing oil and gas infrastructure can lead to 30% capex saving and million tons of CO₂ pa emission reductions.

In this paper, potential concepts of energy integration for offshore oil and gas assets are introduced, and some lessons learned and implications for reusing or repurposing late-life offshore assets for Vietnam are also presented.

Key words: Energy integration, late-life offshore oil and gas assets, electrification, green hydrogen, carbon capture and storage.

1. Introduction

After years of production, the oil and gas industry is facing an increasing demand for decommissioning which requires large costs and negatively affects the surrounding environment. Though worldwide estimates vary greatly, on average, decommissioning (decom) a complete platform may cost USD 15 million to USD 20 million in shallow waters (such as in the Gulf of Mexico), about GBP 30 million (USD 40 million) for small platforms, and GBP 200 million (USD 269 million) for large structures in deep waters (such as in the UK North Sea) [1]. According to Rystad Energy [2], the total value of the global pool of decom projects that will accumulate through 2024 could reach USD 42 billion, dominated by the UK North Sea. Besides, post-decom environment impacts are also of

great concern since a typical eight-leg structure provides a home for 12,000 to 14,000 fishes, and a typical four-leg structure provides 2 to 3 acres of habitat for hundreds of marine species, according to a study by the Coastal Marine Institute [3]. Therefore, one of the critical issues in the oil and gas industry is how to reduce the decom cost and protect the environment.

Conventionally, late-life offshore oil and gas assets must be decommissioned if they cannot work longer or be reused/repurposed. If the scrap steel market is stable and developed, contractors will get scrap revenue from the sale [4]. Otherwise, the scrap yards will charge the contractors to unload steel platforms [5]. Operating contractors are responsible for executing safe and environmentally sound decommissioning when operations cease. Nevertheless, almost all scrapping yards are on beaches so pollutants can cause serious environmental harm with long-term effects for occupational, public, and environmental health [4]. A “green” solution for offshore oil and gas assets is



Date of receipt: 30/8/2021. Date of review and editing: 30/8 - 30/9/2021.

Date of approval: 7/10/2021.

the best solution to deal with challenges of decarbonisation and decommissioning.

In recent years, international organisations (such as WEC, Nexstep, and North Sea Energy) and countries (such as Norway, UK, and the Netherlands) have been appreciating the role of offshore oil and gas assets in energy integration. By sharing infrastructure, the levelised costs of new technologies will reduce and promote the realisation of the ideas. In the WEC North Sea Conference in January 2017, market parties considered electrification, Power-to-gas (PtG), and carbon capture and storage the most potential technologies. Electrified platforms mean that energy is consumed at sea rather than transport to shore; PtG technologies enable energy storage and efficient transportation to shore; and CCS technologies reduce greenhouse gas emission [6 - 8]. With PtG technology, surplus electricity produced at offshore wind farms could be converted into hydrogen, methane, or other gases, and transported to shore using already existing pipelines.

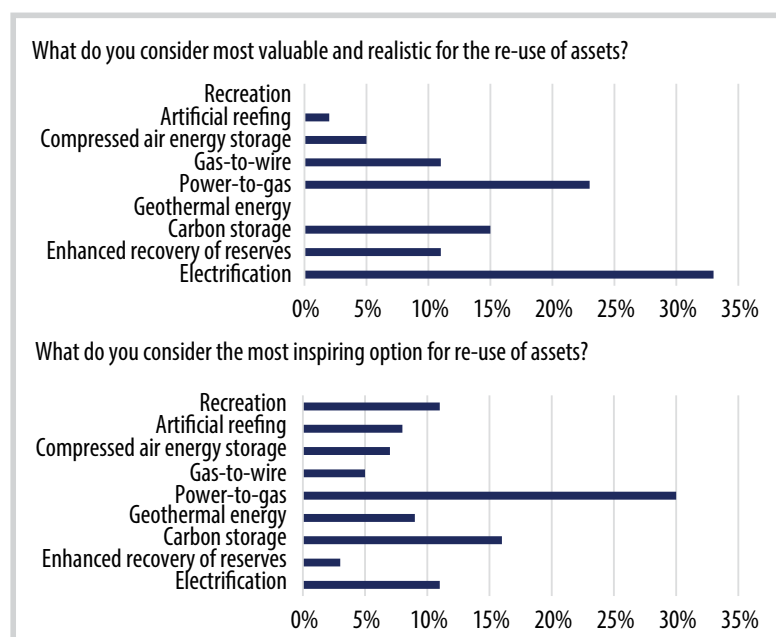


Figure 1. Opinion of market parties on prolonged and re-use options [6].

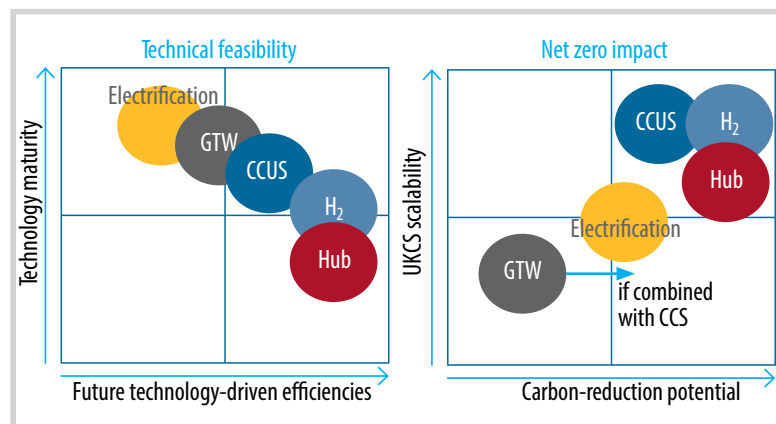


Figure 2. Technology screening for five concepts in the UK [9].

In which, green hydrogen is the most viable option of PtG technologies and is being studied and tested by some countries such as the UK and the Netherlands.

Similarly, the Oil and Gas Authority (OGA) has pointed out that energy integration between oil and gas and renewable energy is the main solution to achieve net-zero emission by 2050 [9, 10]. The North Sea provides several energy options which can all be integrated: wind farms, oil and gas platforms, tidal and wave energy, green hydrogen, floating solar, OTEC (ocean thermal energy conversion). Offshore oil and gas assets can play an important role, for example in the storage of CO₂, and the production of hydrogen and renewable energy [11]. The OGA forecasted that oil and gas will remain an important part of the energy mix for the foreseeable future, and the oil and gas industry will go much further in reducing its carbon footprint from operations. A more integrated offshore energy sector, including closer links between oil and gas and the offshore renewables, will be vital to accelerate the energy transition [9]. Five potential concepts that OGA mentioned to deal with energy transition include Electrification, Gas-to-wire (GtW), CCUS/CCS, Hydrogen, and Energy Hubs.

According to WEC, value is created through the delay of decommissioning costs (~EUR 1 billion). Cost reduction for CCS could save EUR 14 billion over the 2017 - 2050 period. CCS as well as electrification of existing O&G platforms contribute to CO₂ reduction. If 25% of platforms would be electrified, then 4 Mt CO₂ could be avoided over the 2017 - 2050 period. For CCS technology, based on a "medium" roll-out scenario, CO₂ emissions could be reduced by approximately ~1,200 Mt in the 2017 - 2050 period [6]. According to Nexstep, offshore asset reuse will reduce the decommissioning cost in the Netherlands by 30% [11]. However, studies show that only 10% of the platforms in the Netherlands are suitable for reuse.

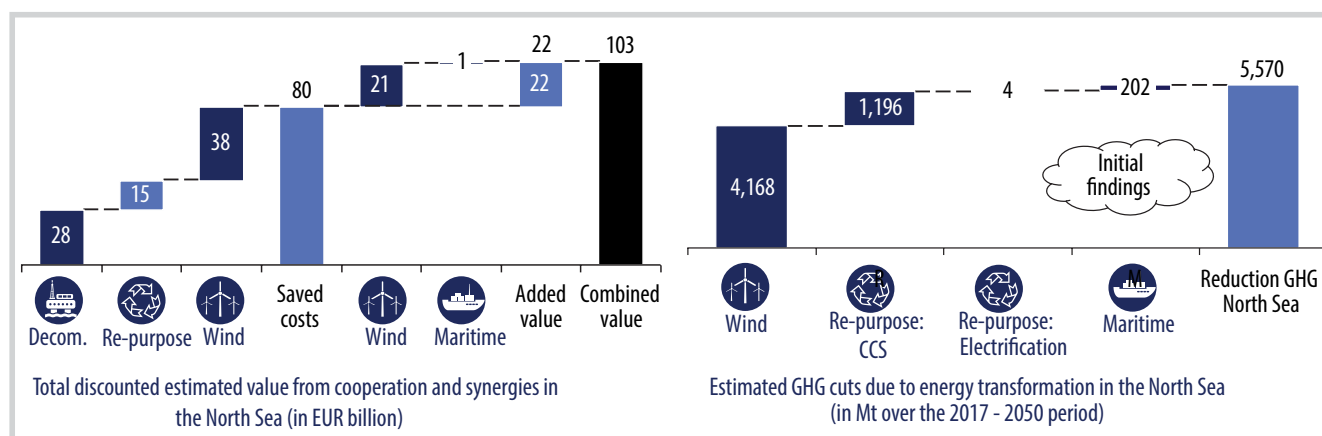
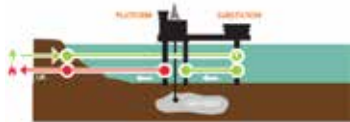
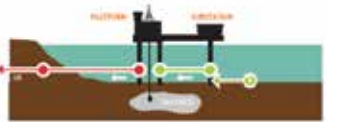
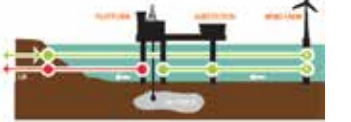


Figure 3. Benefits of repurposing old O&G assets in the North Sea [6].

Table 1. Three options for offshore platform electrification in the North Sea [9, 12]

	Option 1 (Power from shore)	Option 2 (Power from interconnectors)	Option 3 (Power from wind farms)
Description	A platform can be connected via a cable to the onshore grid 	Platform uses power from interconnectors 	Platform uses power from wind farms 
Advantages	Power supply continuity	Power supply continuity Capex savings (shorter cables)	Power supply continuity Capex savings (cables and substations)
Disadvantages	Viable for near-shore platforms High capex investment in cables and substation	Viable with platform near interconnectors	Viable with platform near offshore wind farms

As can be seen, electrification, hydrogen, and CCS are the potential concepts for energy integration. However, these technologies are still at a very early stage of development and therefore hurdles exist in all areas. In many cases, there are no example business cases to learn from and often technologies are not yet available, or not designed for offshore use [6]. At present, there are only a few pilot projects in Norway and the Netherlands, and research projects in the UK. The next part presents the status of these potential concepts of energy integration for offshore oil and gas assets.

2. Potential concepts of energy integration for offshore oil and gas assets

2.1. Electrification

Electrification of oil and gas platforms is a way in which energy can be consumed efficiently at sea [6]. This idea will help increase energy efficiency and cut down a

large amount of carbon emissions. The offshore oil and gas platforms are using gas- or diesel-powered generators to supply their own electricity needs. Due to the space and weight limitations of the platform, these generators are designed with minimum power generation facilities. This means that the energy conversion efficiency rate is low and carbon emissions relatively high. This kind of offshore generator emits more CO₂ than an onshore generator. To reduce carbon emissions of offshore oil and gas activities, electrification is considered the optimal solution.

In addition, old platforms can be converted into electrical substations for floating offshore wind farms at the end of field life. The conversion will be more advantageous if the offshore platform is electrified. Electrification for offshore platforms is still in the early research and implementation stages. In the North Sea, three electrification options for offshore oil and gas platforms are suggested.

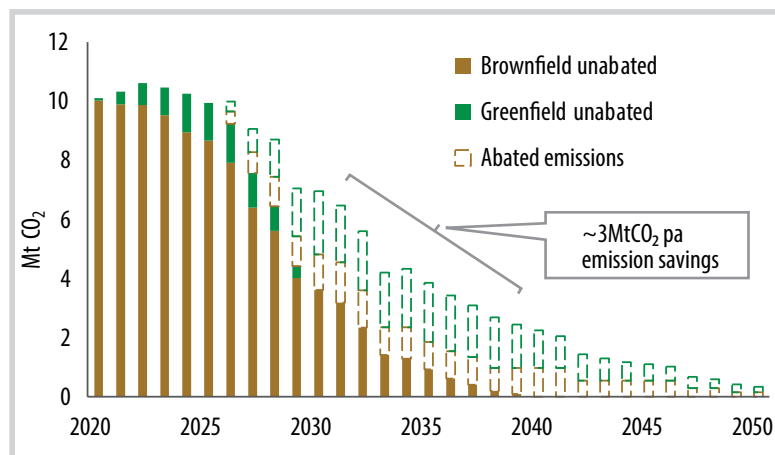


Figure 4. Potential emission reduction from O&G power generation [10].

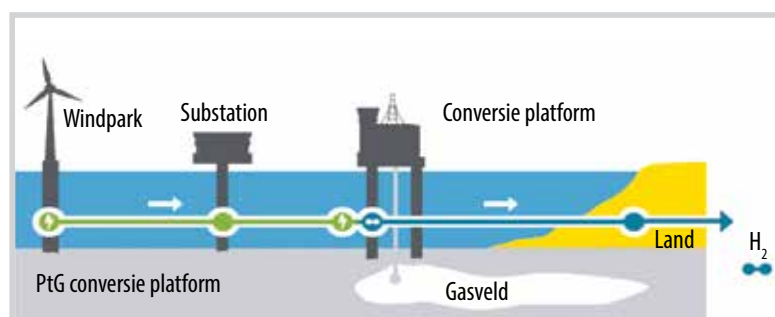


Figure 5. Schematic overview of conversion to green hydrogen [13].

In the Netherlands, the transmission system operator (TSO) TenneT is the designated offshore grid operator with the statutory task to create a dedicated offshore grid to connect offshore wind energy farms to the onshore grids. For many platforms further offshore, it would significantly reduce their costs of obtaining a grid connection if it would be possible to tie in and connect to an offshore platform [12]. Besides, the North Sea Energy program is researching the potential connection between offshore platforms and wind farms.

Electrification can lead to lower operating costs for platform operators and eliminate emissions from traditional generators. According to OGA, the oil and gas industry could significantly reduce GHG emission (by approximately 2 - 3 MtCO₂e pa) by sourcing power for its UKCS platform either from the shore or from offshore renewables. While brownfield electrification projects could face high Capex, which could be significantly reduced through synergies with wind power (could lead to breakeven), while greenfield (new assets) electrification can add value through Capex savings to offset power connection cost (BCR > 1) [10].

It is obvious that electrification is an essential response by the O&G industry to net-zero emission. Reducing emissions will be an urgent mission when IOCs and NOCs are dealing with energy transition. Sourcing electricity for O&G directly from offshore renewables helps reduce project lifecycle costs. Furthermore, lower operating costs can extend the lifetime of the field and increase the opportunity to

utilise the platform for other future potential purposes, such as offshore hydrogen production.

2.2. Green hydrogen

Green hydrogen is produced using renewable energy and electrolysis to split water. With PtG technology, surplus electricity produced at offshore wind farms could be converted into hydrogen and transported to shore using already existing pipelines [6]. This technology is an efficient solution for storing and transporting energy to shore. The existing offshore pipelines could be put into a new production use instead of installation of new offshore power cables. Because the transportation capacity of pipelines is much larger than that of power cables, transportation losses are less, and grid stability is not a concern. However, quantitative evaluation of this idea is difficult because limited real-life experience is available. The offshore hydrogen production model is being studied and tested by some countries, such as the UK and the Netherlands.

In the UK, the results of OGA research show that offshore green hydrogen generation may also be placed offshore, potentially repurposing legacy oil and gas platforms. Depending on distances from shore, this may provide efficient energy transmission [9]. The offshore green hydrogen option consists of three steps: (1) wind-powered electrolysis on offshore platforms; (2) hydrogen storage in abandoned fields or salt caverns; (3) hydrogen transportation with re-used pipelines. As can be seen, all offshore oil and gas assets, such as platforms, pipelines, and reservoirs, are fully utilised in the hydrogen production process. However, this study also indicates that green hydrogen is not economically attractive today (BCR ~ 0.7) due to high electrolysed costs. OGA expects that these costs will be reduced to achieve project breakeven by technology improvements in this decade [10].

In the Netherlands, North Sea Energy also shows that power can be converted into hydrogen using electrolysis [13]. Electrical

electricity. In the future, the platform can be directly powered by offshore wind. Green hydrogen products will be mixed with extracted gas and then transported to shore through the existing gas pipeline system. The future operation and maintenance costs can be shared between hydrogen and gas producers. The project studies how hydrogen can be mixed with natural gas in existing gas pipelines, testing the best percentages for onshore processing [17], and specifying the mixing percentage of hydrogen in the natural gas suitable for the onshore distribution grid [18]. Here are some key technical characteristics of the Q13a-A platform used for testing offshore green hydrogen production and transportation.

According to the implementation progress, the PosHydon project is onshore electrolyser testing and offshore installation, and ready to start up in Q4 2021. If the project is successfully implemented, it will be a good lesson for countries in the North Sea region and the world. Furthermore, some platforms and pipelines could be given a second life in the energy transition and be used for power conversion and transportation of green hydrogen [19].

2.3. Carbon capture and storage (CCS)

The CCS technology will provide an opportunity to reuse/repurpose offshore oil and gas assets to store CO₂ under the empty oil or gas fields. CO₂ will be captured and transported from the shore through new or existing pipelines. Then CO₂ is slowly

injected into the reservoir, which will increase the pressure in the reservoir. Injection will continue until the reservoir's pressure almost reaches the same level as the original natural gas pressure. The reservoir pressure will be kept at a lower level than the original one, to ensure the natural geological closure of the reservoir [13]. If the platform is already electrified, the offshore compression could easily be installed. If the platform is applying the CO₂-EOR method to prolong the field lifetime, the infrastructure is very convenient to develop CCS technology. Almost all offshore oil and gas assets, such as platforms, pipelines, wells, and reservoirs, will be utilised to reduce costs and promote the offshore CCS technology.

According to WEC, the CCS projects in the North Sea have a potential value of EUR 14.4 billion over the period from 2020 to 2050. This value includes the cost savings resulting from the reduction in CCS costs from EUR 70/ton of CO₂ in 2017 to EUR 45/ton of CO₂ in 2030. From 2020 to 2030, the annual CO₂ storage will increase linearly from 4 Mt to 46 Mt storage per year and remain constant at 46 Mt per year from 2030 [6].

In the North Sea, Norway and the UK are two countries that are studying the possibility of developing CCS when taking advantage of offshore oil and gas assets. Below is a summary of the research results of these two countries.

Norway

Norway has a long history of carbon capture and storage from the world's first offshore CCS project "Sleipner" in 1996. The Norwegian

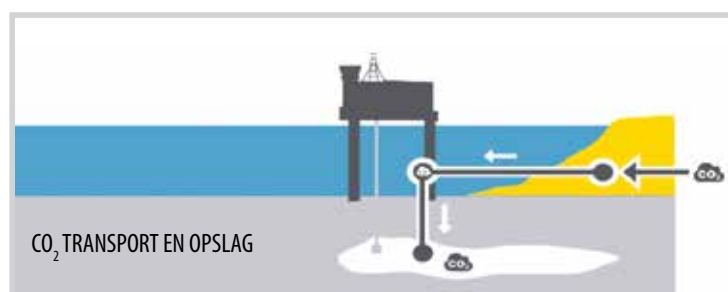


Figure 8. Schematic overview of CCS technology [13].

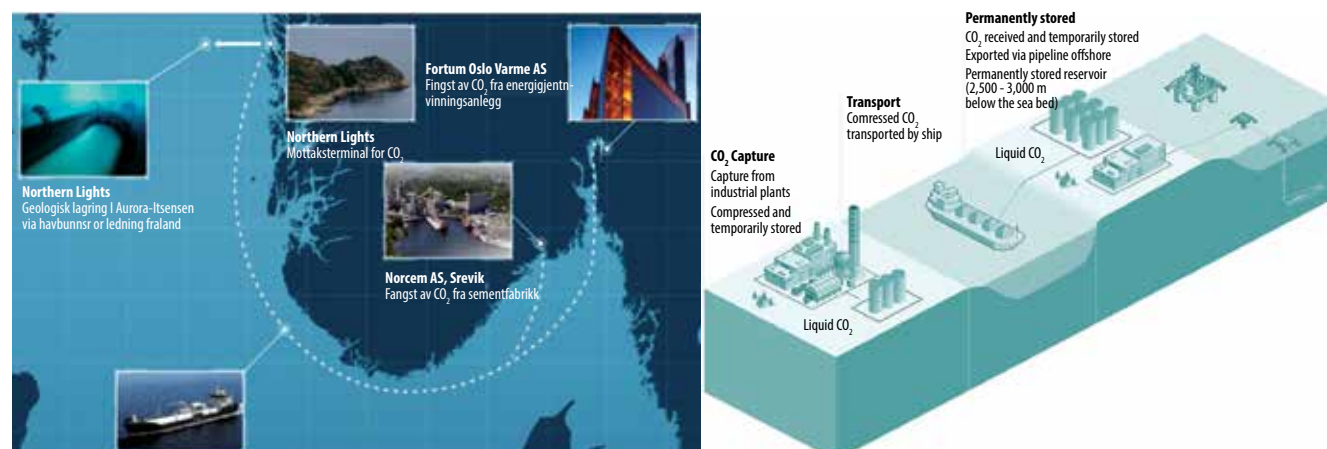


Figure 9. The Norwegian full-scale CCS project Longship [22, 23].

government considers CCS an important solution to achieve net zero emissions by 2050. Since 2005, Gassnova, a state-owned enterprise under the Norwegian Ministry of Oil and Energy, has promoted technological development, reduced costs, and enabled CCS development projects through knowledge sharing and technology transfer with partners [20]. In 2016, the results of a feasibility study on CCS solutions conducted by Statoil were released by the government. This study demonstrated the feasibility of combining components that make up the value chain and can be realised into a full-scale CCS project. Gassnova was assigned to represent the Norwegian government to further develop this idea. In December 2020, the Norwegian government made a funding decision and named the project Longship [21]. The project's ambition is to be able to store 1.5 million tons of CO₂ per year. So far, this is the largest project in the history of Norway with a total cost of about USD 2.83 billion (USD 1.93 billion investment cost and a 10-year operating cost of USD 0.9 billion) which the

Norwegian government is expected to provide USD 1.89 billion [22].

The Longship project consists of three main parts:

- CO₂ capture at Norcem Cement Plant (belonging to Heidelberg Group) in Brevik;
- CO₂ capture at the Fortum Oslo Waste-to-Energy Plant in Oslo;
- Combined transportation and storage solution, managed by Northern Lights JV DA.

The Northern Lights JV was launched in March 2021 as a joint venture between Equinor, Shell, and Total. The Northern Lights project, which is part of the Longship project, is responsible for the transport of CO₂ by ships and the permanent storage of CO₂ in reservoirs located 2.5 - 3 km deep on the seabed. It is expected that phase 1 of this project will operate in mid-2024 with a capacity of 1.5 million tons of CO₂/year.

According to Gassnova, CO₂ can be stored forever under depleted oil and gas reservoirs and salt aquifers. Offshore oil and gas assets have an important role in the CCS process. The existing pipeline transports carbon from shore to the compression station, are converted by platform, to compress CO₂ into depleted reservoirs. In 2020, Gassnova expected the allocation of investment costs for carbon transport and storage as follows:

If late-life offshore oil and gas assets can be used

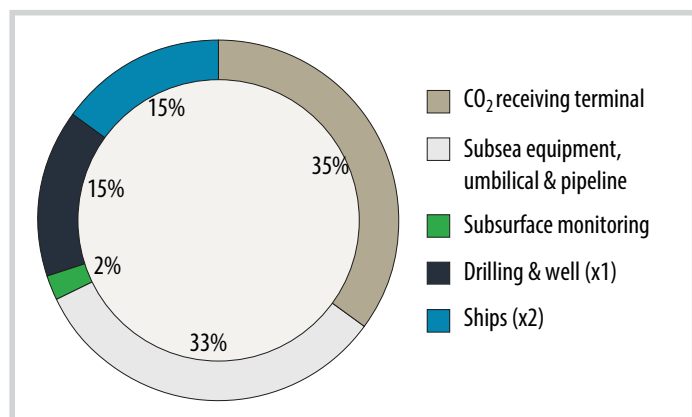


Figure 10. Estimated investment cost spread across the physical elements of the transport and storage facilities [24].

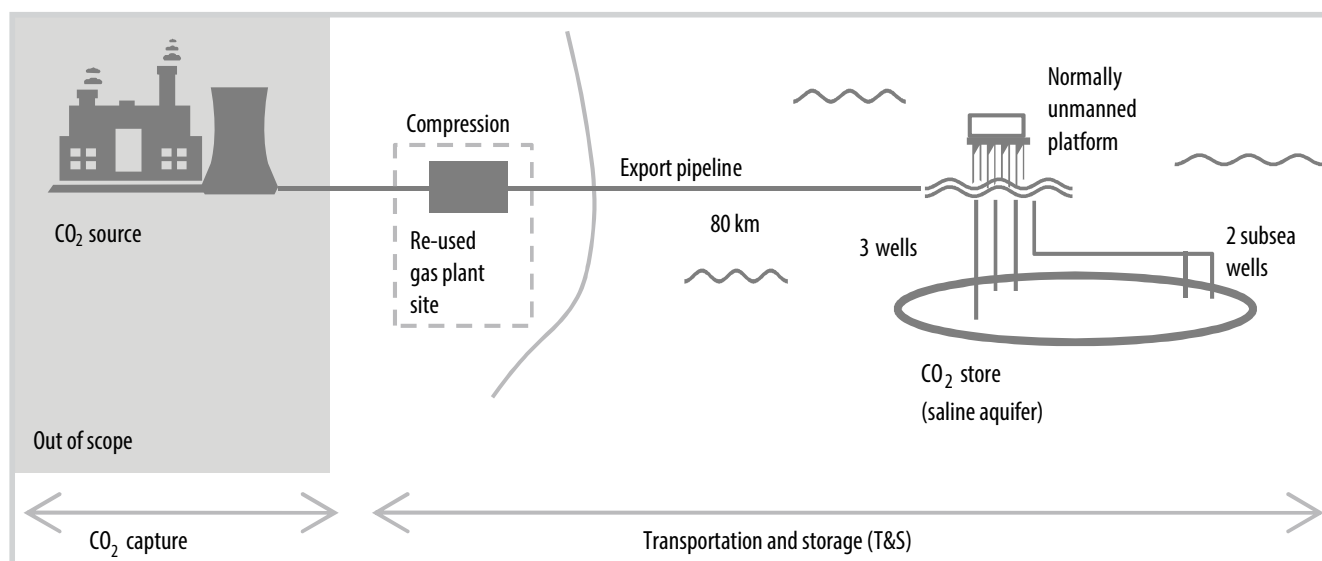


Figure 11. Notional CCS project [10].

for carbon transport and storage, there is potential for investment savings at this stage.

UK

The UK also considers CCS technology as an important solution to achieve net-zero emissions by 2050. To achieve this ambition, OGA has proposed a scenario of building CCS by 2050. Accordingly, OGA expects to increase annual compression capacity at a rapid growth rate from 5 million tons of CO₂/year in 2025 to 69 million tons of CO₂/year by 2040, and 130 million tons of CO₂/year by 2050.

Under the OGA scenario, offshore oil and gas assets will be utilised in CO₂ transport and storage:

- CO₂ transport: Onshore gas plants can be converted into CO₂ compressor plants, taking advantage of the existing pipeline system from gas plants to transport CO₂ to compressed air points. It is assumed that this pipeline is about 80 km long and 20" in diameter.

- CO₂ storage: Existing platforms and wells can be used to compress CO₂ into empty reservoirs.

The OGA research results indicate that reuse of existing oil and gas infrastructure can lead to 20 - 30% capex savings, thus the transportation and storage costs around GBP 12 - 30/ton of CO₂ (USD 16 - 40/ton of CO₂) could make CCS economically attractive to help decarbonise in the UK [10].

2.4. Lesson learned for late-life offshore oil and gas assets in Vietnam

Obviously, offshore oil and gas assets play an important role in energy integration which can help reduce production emission for the oil and gas industry, as well as accelerate the progress of CCS and green hydrogen in support of decarbonisation. Firstly, platform electrification could reduce emissions on oil and gas structures by using offshore electricity generated from wind farms. Secondly, surplus electricity produced at offshore wind farms could be converted into green hydrogen at the platforms and transported to shore by existing pipelines. Finally, CO₂ is transported by pipeline, and injected into depleted offshore oil and gas fields.

However, these new technologies are in the early stages of development with high capex, so it is necessary to maximise the utilisation of energy integration. By sharing offshore infrastructures, these new technologies have more opportunities to develop in the future. Due to the shortage of example business cases, it is difficult to

generalise the technical requirements for offshore oil and gas assets. Based on existing documents, the offshore oil and gas assets in the North Sea often have the following technical characteristics:

- Water depth (WD): often in shallow water
 - + 20 m: Neptune Energy's Q13a-A in PosHydon project [16];
 - + 29.6 m: project IJVERGAS [25];
 - + Less than 50 m: 10% of platforms in the Netherlands that have been reused by Nexstep [11, 26].
- Distance from shore:
 - + 51 km: Neptune Energy's Q13a-A in PosHydon project [16];
 - + 80 km: UK CCS development scenario [10].
- Type of platform: Mostly fixed platforms.
- Diameters of pipelines: 20" [10], 24" and 36" [25].

Compared to the above-mentioned, Vietnamese offshore oil and gas assets have similar characteristics [27], specifically:

- Water depth (WD): All production projects are in shallow water.
- Distance from shore: Structures are located far from the shore, but the infrastructure allows easy connection to shore through offshore pipelines. The distance from onshore of main pipelines in Cuu Long basin, Nam Con Son basin, and Malay - Tho Chu basin is 110 km, 371 km, and 298 km, respectively.
- Type of platform: Mostly wellhead platforms (a kind of fixed platform), only one semi-submersible platform in Dai Hung field.
- Diameters of pipelines: ~ 26" for main pipelines.
- Density of distribution: All production projects are concentrated in the 4 main basins: Cuu Long basin, Nam Con Son basin, Malay - Tho Chu basin, and Song Hong basin.
- Ability to connect to existing infrastructure: Pipelines are only connected internally in each basin.
- Oil/gas reservoirs: Offshore oil/gas reservoirs are connected to wellhead platforms. Therefore, CCS projects can reuse the offshore facilities to store CO₂ in these empty reservoirs.

- Ability to connect to offshore wind farms: According to draft Power Master Plan VIII [28], potential offshore wind plants will be located in the North, North Central, South Central, and Southern regions of Vietnam, corresponding to the Song Hong basin, Cuu Long basin, Nam Con Son basin, and Malay - Tho Chu basin. The potential offshore wind plants can be in more or less 50 m of water depth in the South, South Central, and North Central regions.

If preliminary assessment, Vietnam offshore facilities can research the potential connecting oil and gas assets and renewable energy instead of decommissioning, especially late-life offshore oil and gas assets in the South. However, not all oil and gas assets can be reused for new technologies. In the Netherlands, only 10% of platforms is suitable for reuse/repurpose, but it can lead to 30% capex savings and million tons of CO₂ pa emission reductions [11], which is a great driving factor to develop the new technologies.

3. Conclusion

Energy integration is a green solution reusing or repurposing assets for new technologies, such as electrification, green hydrogen and CCS, or promoting synchronous development of technologies, sharing offshore infrastructure, and reducing infrastructure investment costs. The energy sector can start making unified decisions about how to deal with end-of-life offshore oil production facilities. The late-life offshore oil and gas assets will have a new life and play an important role in dealing with climate change and gradually achieving decarbonisation goals. Integrating late-life offshore oil and gas assets and other offshore energy farms could reduce the costs and make the new technologies more economically feasible.

According to the North Sea's case, the conversion of offshore oil and gas assets needs to have a long-term strategy and follow a roadmap. In which, three important milestones need to be achieved: (i) minimising carbon emissions in offshore oil and gas exploitation through electrification technology; (ii) energy transition, connection, and development of green hydrogen and CCS technologies; (iii) connecting all energy sources to reach the committed carbon emission reduction target.

In general, the Vietnamese offshore oil and gas assets have similar technical characteristics with those in the North Sea. Therefore, there is an opportunity to have

a green future for late-life offshore oil and gas assets in Vietnam. To turn the ideas into reality, more detailed studies will be needed. The studies should be conducted as soon as possible because Vietnam will face the wave of decommissioning in the next decade.

References

- [1] Rajesh Chhabara, "Offshore oil rigs: Can decommissioning ever be green?", *Sustainable Business*, 1/9/2009. [Online]. Available: <https://www.reutersevents.com/sustainability/stakeholder-engagement/offshore-oil-rigs-can-decommissioning-ever-be-green>.
- [2] Rystad Energy, "Global oil & gas decommissioning costs to total USD 42 billion through 2024, dominated by UK North Sea", 22/5/2020. [Online]. Available: [https://www.rystadenergy.com/newsevents/news/press-releases/global-oil-gas-decommissioning-costs-to-total-\\$42-billion-through-2024-dominated-by-uk-north-sea/](https://www.rystadenergy.com/newsevents/news/press-releases/global-oil-gas-decommissioning-costs-to-total-$42-billion-through-2024-dominated-by-uk-north-sea/).
- [3] Bureau of Safety and Environmental Enforcement (BSEE), "Rigs-to-reefs", 2021. [Online]. Available: <https://www.bsee.gov/what-we-do/environmental-compliance/environmental-programs/rigs-to-reefs>.
- [4] NGO Shipbreaking Platform, "Recycling outlook: Decommissioning of North Sea floating oil & gas units", Norway, 2019.
- [5] ICF International and TSB Offshore, "Decommissioning methodology and cost evaluation", 2015.
- [6] World Energy Council (WEC), "The North Sea opportunity", 2017.
- [7] Rene Peters and Ewald Breunese, "Prolonging life and re-purpose of oil and gas assets", World Energy Council, 2016. [Online]. Available: <https://www.worldenergycouncil.nl/wp-content/uploads/2017/02/WEC-repurpose-TNO-Shell-breakout-session.pdf>
- [8] Rene Peters, "A green use for old drilling platforms?", *Energy World*, 2019.
- [9] OGA, "UKCS energy integration: Interim findings", 17/12/2019. [Online]. Available: <https://www.ogauthority.co.uk/news-publications/publications/2019/ukcs-energy-integration-interim-findings/>.
- [10] OGA, "UKCS energy integration: Final report", 6/8/2020. [Online]. Available: https://www.ogauthority.co.uk/media/6625/ukcs_energy_integration_phase-ii_report_website-version-final.pdf.

- [11] Nexstep, "Re-use & decommissioning report: Innovation & collaboration", 2020. [Online]. Available: https://www.nexstep.nl/wp-content/uploads/2020/07/Re-use-decommissioning-rapport-2020-ENG_final.pdf
- [12] North Sea Energy, "North Sea Energy II regulatory framework: Barriers or drivers for offshore system integration", 2018.
- [13] Sytske Stuij and Suzan Tack, "North Sea Energy II: Strategic assessment of environmental impacts of offshore system integration options", North Sea Energy, 2018. [Online]. Available: https://north-sea-energy.eu/static/ce06f2b63708efd85f33fbf216fbd28e/NSE2_D.D2_Strategic-Assessment-of-Environmental-Impacts-of-Offshore-system-Integration-Options-1.pdf.
- [14] Sanja Pekic, "Netherlands grants PosHYdon offshore green hydrogen project", 22/7/2021. [Online]. Available: <https://www.offshore-energy.biz/netherlands-grants-poshydon-offshore-green-hydrogen-project/>.
- [15] Neptune Energy, "The world's first offshore green hydrogen plant", 2021. [Online]. Available: <https://www.neptuneenergy.com/esg/new-energy/poshydon-hydrogen-pilot>.
- [16] Neptune Energy, "PosHYdon Pilot: Offshore green hydrogen", 2019. [Online]. Available: <https://www.neptuneenergy.com/esg/new-energy/poshydon-hydrogen-pilot>.
- [17] Naomi Klinge, "Existing oil and gas infrastructure has potential in offshore green hydrogen", 19/8/2021. [Online]. Available: <https://www.upstreamonline.com/energy-transition/existing-oil-and-gas-infrastructure-has-potential-in-offshore-green-hydrogen/2-1-1054605>.
- [18] Chris Carpenter, "Offshore hydrogen production enables far offshore wind development", 23/11/2020. [Online]. Available: <https://jpt.spe.org/offshore-hydrogen-production-enables-far-offshore-wind-development>.
- [19] World Energy Council, "Bringing North Sea energy ashore efficiently", 2017. [Online]. Available: <https://www.worldenergycouncil.nl/new-report-released-on-bringing-north-sea-energy-ashore-efficiently/>.
- [20] Gassnova SF, "UK's hydrogen strategy proposal launched", 2021.
- [21] Northern Lights, "About the longship project", 2021. [Online]. Available: <https://northernlightssccs.com/about-the-longship-project/>.
- [22] Norwegian Government, "The Government launches 'longship' for carbon capture and storage in Norway", 21/9/2020. [Online]. Available: <https://www.regjeringen.no/en/aktuelt/the-government-launches-longship-for-carbon-capture-and-storage-in-norway/id2765288/>.
- [23] Equinor, "Carbon capture, utilisation and storage (CCS & CCUS): We're sending carbon back where it came from", 2021. [Online]. Available: <https://www.equinor.com/en/what-we-do/carbon-capture-and-storage.html>.
- [24] Gassnova SF, "Developing longship, key lessons learned", 25/11/2020. [Online]. Available: <https://gassnova.no/en/news/report-developing-longship-key-lessons-learned>.
- [25] North Sea Energy, "JVERGAS: Feasibility of hydrogen generation on a multifunctional island at Ijmuiden Ver", 2020.
- [26] Nexstep, "Offshore decom conference: National platform for re-use & decommissioning", 2017.
- [27] Nguyễn Thu Hương, "Báo cáo khảo sát: Tận thu giá trị các tài sản khai thác dầu khí ngoài khơi sau khi dự án dừng hoạt động", Viện Dầu khí Việt Nam, 2021.
- [28] Viện Năng lượng, "Dự thảo Đề án Quy hoạch phát triển điện lực quốc gia thời kỳ 2021 - 2030, tầm nhìn đến năm 2045", 2021.

Fertilizer production: Rising input material cost

In the “Commodity Markets Outlook” report by the World Bank, energy prices soared in the 3rd quarter of 2021 and are expected to remain elevated in 2022, adding to global inflationary pressures and potentially shifting economic growth to energy-exporting countries from energy-importing ones.

The World Bank’s latest Commodity Markets Outlook forecasts that energy prices - expected to average more than 80% higher in 2021 compared to last year - will remain at high levels in 2022 but will start to decline in the second half of the year as supply constraints ease. Non-energy prices, including agriculture and metals, are projected to decrease in 2022, following strong gains this year.

In 2021, some commodity prices rose to or exceeded levels not seen since the spike of 2011. For example, natural gas and coal prices reached record highs amid supply constraints and rebounding demand for electricity, although they are expected to decline in 2022 as demand eases and supply improves. However, additional price spikes may occur in the near-term amid very low inventories and persistent supply bottlenecks.

Crude oil prices (an average of Brent, WTI, and Dubai) are expected to average USD 70 a barrel in 2021, an increase of 70%. They are projected to be USD 74 a barrel in 2022 as oil demand strengthens and reaches pre-pandemic levels. The use of crude oil as a substitute for natural gas presents a major upside risk to the demand outlook, although higher energy prices may start to weigh on global growth.

“High natural gas and coal prices are impacting the production of other commodities and pose an upside risk to price forecasts”, said John Baffes, Senior Economist in the World Bank’s Prospects Group. “Fertilizer production has been curtailed by higher natural gas and coal

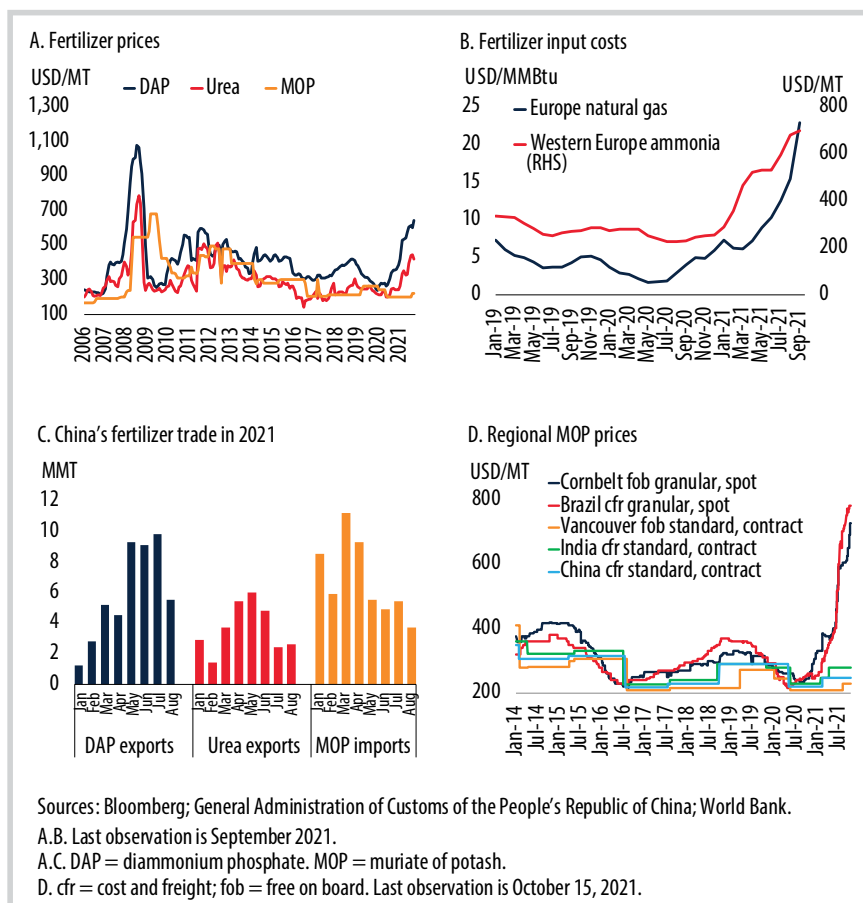


Figure 1. Fertilizer market developments [1].

prices, and higher fertilizer prices have been pushing up input costs for key food crops”.

According to the World Bank [1], most fertilizer prices increased sharply in the third quarter of 2021 and continued rising in early November, reaching levels unseen since the 2008 - 2009 global financial crisis. Prices have been driven by a confluence of factors - strong demand, rising input costs (energy, materials), production cuts, and trade policies of several countries. Surging natural gas prices in Europe resulted in widespread production cutbacks in ammonia - an important input for nitrogen

fertilizers - while escalating thermal coal prices in China led to a rationing of electricity use in some provinces and forced fertilizer factories to cut production. Energy prices also increased in the United States as Hurricane Ida hampered natural gas production in the U.S. Gulf Coast and several large fertilizer companies had to declare force majeure as production was halted.

Urea prices reached levels unseen since 2008 and DAP (diammonium phosphate) prices climbed to the highest since 2012, while potash prices saw historically large divergence across regional markets [1].

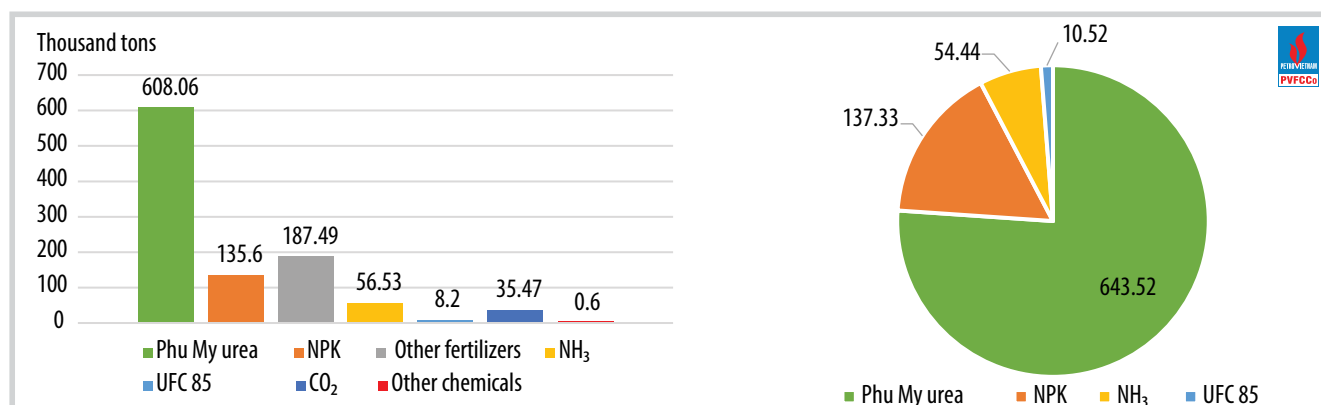


Figure 2. PVFCCo's sales and production in the first 10 months (thousand tons).

According to the Chemical & Engineering News [2], in Illinois, the price of DAP, the most widely used phosphate fertilizer, rose by more than 78% over the past year, according to a 4 November report from the US Department of Agriculture. The price of two nitrogen-based fertilizers, anhydrous ammonia and urea, more than doubled over the same period. Much of the price increase has happened since the beginning of October. Schnitkey noted that manufacturers have big incentives to produce more fertilizer, which could lower prices. But the price will also depend on more unpredictable factors, like the state of the Covid-19 pandemic and the cost of natural gas.

As per mid October 2021 (14 October 2021), the prices of both prilled urea and granular urea have increased as compared to mid September 2021. Specifically, prilled urea surged by USD 305/ton in the Baltic Sea, by USD 312/ton in the Black Sea, and by USD 330/ton in the Middle East. Granular urea increased by USD 277/ton in the Middle East, and by USD 265 /ton in SE Asia. On 14 October 2021, prices ranged from USD 620/ton to USD 780/ton for prilled urea and from USD 624/ton to USD 780/ton for granular urea.

In the first 10 months of 2021, PVFCCo has operated Phu My Fertilizer Plant safely and stably, with the production reaching

643,520 tons of Phu My urea (3% higher than planned), 137,330 tons of NPK (8% higher), 54,440 tons of NH₃ (6% higher) and 10,520 tons of UFC 85 (3% higher).

Regarding its sales in the same period, PVFCCo reported a volume of 608.06 thousand tons of Phu My urea (95% of the plan), 35.47 thousand tons of CO₂ (88%), 135.60 thousand tons of NPK (116%), 187.49 thousand tons of other fertilizers (116%), 56.53 thousand tons of NH₃ (111%), 8.2 thousand tons of UFC 85 (119%) and 0.6 thousand tons of other chemicals (112%).

In 2021, PVFCCo faced difficulties since the prices of input materials have risen higher than planned: gas price by 34% (USD 6.33/ton vs. the planned USD 4.74/ton, excluding VAT); the price of methanol (feedstock for UFC 85 production) by 46%. The prices of raw materials for NPK production also soared sharply from the planned price: H₂SO₄ by 57%, H₃PO₄ by 48%, DAP by 51%, and SA by 53%.

By synchronously implementing solutions to optimise production and reduce costs, PVFCCo has achieved a total revenue of over VND 9,400 billion, which is 35% higher than the 10-month plan, and 13% higher than the 2021 plan; and contributed VND 421.3 billion to the national budget, which is 220% higher than the plan.

Urea prices are anticipated to decline marginally in 2022 as feedstock costs moderate. DAP prices are projected to remain elevated in the first half of 2022 on expectations of tight supply unless Chinese export restrictions are relaxed earlier than anticipated. MOP contract prices are forecast to surge in 2022 following significant increases in spot prices.

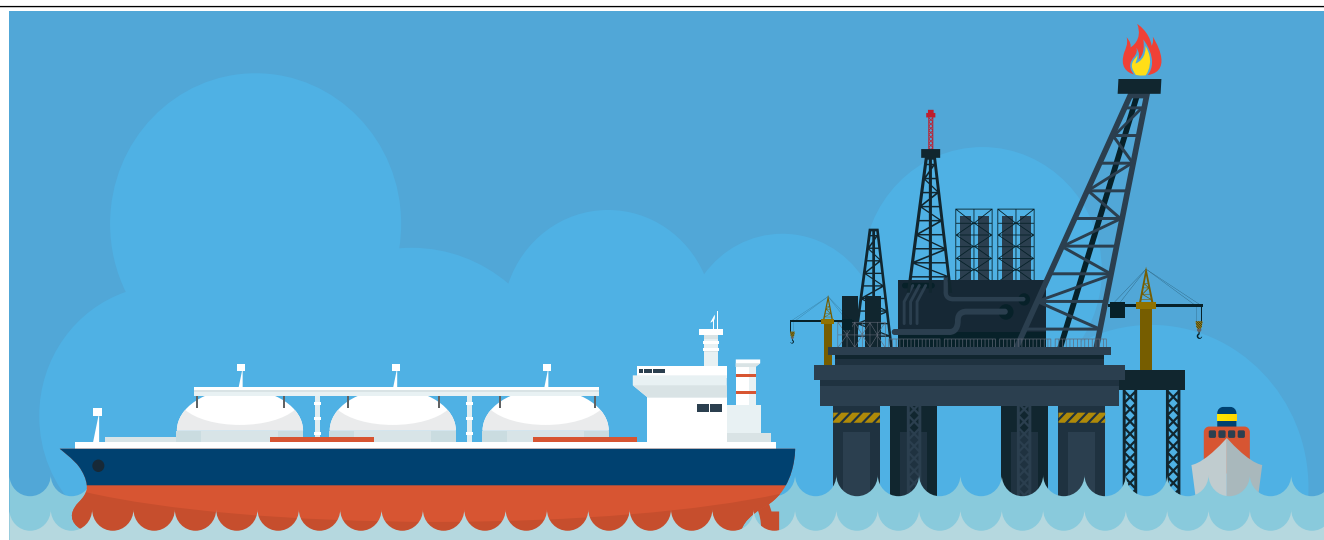
World Bank

PVFCCo has successfully launched two new lines of product formula, NPK Phu My 18-12-8+TE and NPK 18-10-8+8S+TE, with the first batch of 5,000 tons produced in November 2021. The two products will help diversify the high-quality Phu My NPK product line and boost the total output, which is experiencing a spectacular growth in 2021 with an estimate exceeding 150,000 tons.

Hong Minh

References

[1] World Bank, "Commodity Markets Outlook", 21/10/2021.
 [2] Matt Blois, "Expensive inputs and strong demand send fertilizer prices through the roof", *Chemical & Engineering News*, 17/11/2021.



WORLD OIL AND GAS MARKET

The International Energy Agency (IEA) said Brent prices may reach USD 71.50 per barrel in 2021 and USD 79.40 per barrel in 2022 [1], while U.S. Energy Information Administration (EIA) predicted that it would be around USD 72 a barrel in 2022 [2].

In Oil Market Report - November 2021 reported by the IEA, global oil demand is strengthening due to robust gasoline consumption and increasing international travel as more countries re-open their borders. However, new Covid-19 waves in Europe, weaker industrial activity and higher oil prices will temper gains, leaving forecast for oil demand growth largely unchanged since last month's report at 5.5 million barrels per day for 2021 and 3.4 million barrels per day in 2022 [1].

World oil supply is set to rise 1.5 million barrels per day over November and December, with the US providing 400,000 barrels per day of the gain. Saudi Arabia and Russia combined would account for 330,000 barrels per day in line with OPEC+ targets. Total oil supply had already leapt 1.4 million barrels per day m-o-m in October after the US rebounded from Hurricane Ida.

Global refining throughput is set to

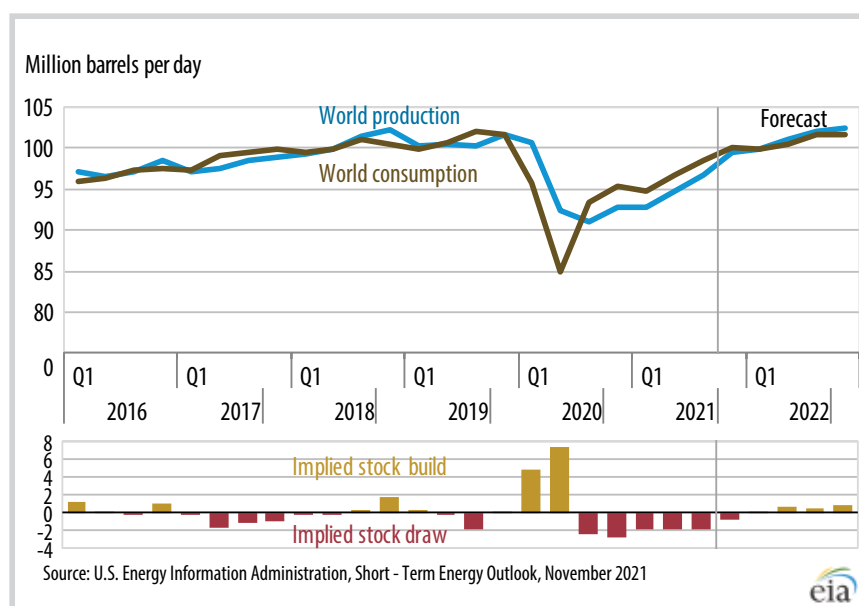


Figure 1. World liquid fuels production and consumption balance [2].

increase by almost 3 million barrels per day from October through December as seasonal maintenance wraps up. Refinery margins rose in October, driven by exceptionally tight product markets, despite the sharp gains in crude oil prices. Further ahead, refinery throughputs are expected to stabilise and generally hold flat in the first half of 2022 before the seasonal increase in 3rd quarter of 2022.

OECD total industry stocks plunged by 51 million barrels in September, with crude oil and middle distillate holdings accounting for most of the declines. In

terms of regions, Europe led the draw-down. At 2,762 million barrels, total OECD industry stocks stood 250 million barrels below the 5-year average and at their lowest level since the start of 2015. Preliminary data for October point to a marginal stock build.

Oil market drivers have begun to shift and benchmark crude prices are easing as a result. Brent crude futures were trading around USD 81 per barrel, down from a high of more than USD 86 per barrel in October. On physical markets, North Sea Dated prices rose in October by USD 9.15

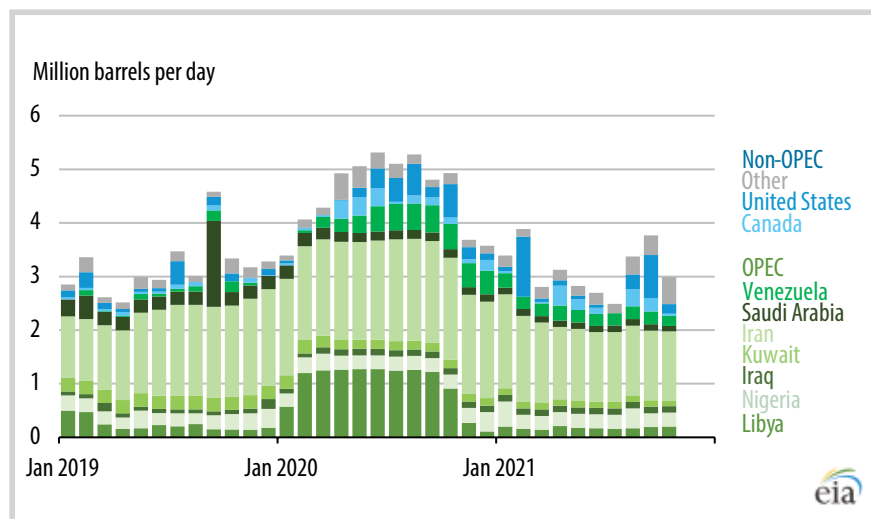


Figure 2. Estimated unplanned liquid fuels production outages among OPEC and non-OPEC producers [2].

Table 1. World crude oil and liquid fuels production (million barrels per day) [2]

Region/Country	2018	2019	2020	2021	2022
OPEC Countries	36,721	34,670	30,710	31,679	33,899
North America	25,334	26,928	25,779	26,265	27,866
Canada	5,364	5,494	5,255	5,589	5,835
Mexico	2,083	1,921	1,939	1,925	1,881
United States	17,886	19,513	18,585	18,750	20,151
Eurasia	14,442	14,488	13,318	13,588	14,515
Russia	11,391	11,480	10,504	10,793	11,583
Azerbaijan	0.796	0.774	0.702	0.719	0.748
Kazakhstan	1,959	1,966	1,860	1,837	1,956
Turkmenistan	0.296	0.267	0.252	0.239	0.228
Latin America	5,389	5,667	5,665	5,738	6,164
Argentina	0.679	0.690	0.635	0.670	0.727
Brazil	3,428	3,674	3,787	3,836	4,141
Colombia	0.895	0.918	0.811	0.764	0.757
Other Latin America	0.388	0.385	0.432	0.467	0.540
Other Non-OPEC	18,831	18,899	18,715	18,698	18,972
World total	100,718	100,652	94,187	95,967	101,417

per barrel m-o-m to USD 83.54 per barrel and WTI at Cushing by USD 9.79 per barrel to USD 81.96 per barrel [1].

IEA reported that global oil production is already rising. In October, oil supplies leapt by 1.4 million barrels per day to 97.7 million barrels per day, with the US post-hurricane recovery accounting for half the increase. A further boost of 1.5 million barrels per day is expected over November and December even as OPEC+ disregarded pleas from major consumers to ramp up beyond a monthly allocated 400,000

barrels per day to cool prices. Over this period, the US is now poised to provide the largest increase in supply of any individual country. IEA has raised its forecast for the US by 300,000 barrels per day for 4th quarter of 2021 and by 200 barrels per day on average in 2022 as current prices provide a strong incentive to boost activity even as operators stick to capital discipline pledges. The US is set to account for 60% of 2022 non-OPEC+ supply gains, now forecast at 1.9 million barrels per day. Even so, the US will not return to pre-Covid rates until the end of 2022 [1].

In the November Short-Term Energy Outlook reported by the U.S. Energy Information Administration (EIA), supply uncertainty in the forecast results from the production decisions of OPEC+ along with the rate at which U.S. oil and natural gas producers increase drilling at forecast price levels [2].

Brent crude oil spot prices averaged USD 84 per barrel in October 2021, up USD 9 per barrel from September and up USD 43 per barrel from October 2020. Crude oil prices have risen over the past year as result of steady draws on global oil inventories, which averaged 1.9 million barrels per day during the first three quarters of 2021. In addition to sustained inventory draws, prices increased after OPEC+ announced in early October - and reaffirmed on 4 November - that the group would keep current production targets unchanged. EIA expects Brent prices will remain near current levels for the rest of 2021, averaging USD 82 per barrel in the 4th quarter of 2021. In 2022, EIA expects that growth in production from OPEC+, U.S. tight oil, and other non-OPEC countries will outpace slowing growth in global oil consumption and contribute to Brent prices declining from current levels to an annual average of USD 72 per barrel.

EIA estimates that 98.9 million barrels per day of petroleum and liquid fuels was consumed globally in October, an increase of 4.5 million barrels per day from October 2020 but 1.9 million barrels per day less than in October 2019. EIA has been revised up forecast for consumption of petroleum and liquid fuels for the 4th quarter of 2021, partially as a result of fuel switching from natural gas to petroleum in the electric power sector in parts of Asia and Europe. This fuel switching is a result of increases in natural gas prices in

Asia and Europe. EIA forecasts that global consumption of petroleum and liquid fuels will average 97.5 million barrels per day for all of 2021, which is a 5.1 million barrels per day increase from 2020. EIA forecasts that global consumption of petroleum and liquid fuels will increase by 3.3 million barrels per day in 2022.

U.S. crude oil production averaged an estimated 11.4 million barrels per day in October, up from 10.7 million barrels per day in September as a result of production increases following disruptions from Hurricane Ida. EIA forecasts production will rise to 11.6 million barrels per day in December. EIA forecasts annual production will average 11.1 million barrels per day in 2021, increasing to 11.9 million barrels per day in 2022 as tight oil production rises in the United States.

At its early October meeting and reaffirmed at its 4 November meeting, OPEC+ committed to maintaining its scheduled crude oil production increase of 400,000 barrels per day in December rather than increase production by more in response to high crude oil prices and increasing demand [2].

OPEC now expects global oil demand to average 96.44 million barrels per day in 2021, for year-on-year growth of 5.65 million barrels per day. For 2022, demand will rise by 4.15 million barrels per day, unchanged from last month's forecast, to hit 100.59 million barrels per day. Its forecasts for non-OPEC production were unchanged from last month's report, at 63.64 million barrels per day for 2021, up 660,000 barrels per day year-on-year, and 66.66 million barrels per day for 2022, up 3.02 million barrels per day [3].

According to the Bloomberg, global oil supply is set to average 101.42 million barrels a day in 2022, while worldwide

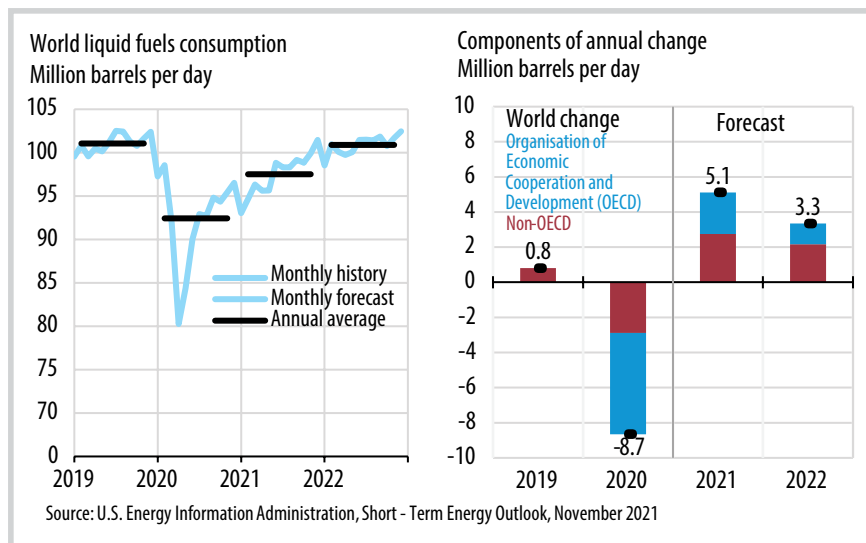


Figure 3. World liquid fuels consumption [2].

demand is seen at 100.88 million barrels a day. Meanwhile, U.S. crude production is expected to rise to average 11.9 million barrels a day in 2022 as drillers make a comeback. A nearly 15% rally in WTI crude prices since July is luring some shale producers to ramp up output, most notably private drillers. While the outlook marks an expected increase in supply, it is still far from the record annual volume reached in 2019 as the recovery across major shale regions has been mixed [4].

If the world continues to make progress on keeping Covid-19 infection and death rates low, the current price of about USD 80 a barrel is reasonable. Actual growth that matches expectations would not push prices higher [5].

Hanh Nguyen

References

[1] IEA, "Oil market report", 11/2021. [Online]. Available: <https://www.iea.org/reports/oil-market-report-november-2021>.

[2] EIA, Short-term energy outlook (STEO), 9/11/2021. [Online]. Available: <https://www.eia.gov/outlooks/steo/>.

[3] Herman Wang, "OPEC cuts 2021 oil demand outlook; still sees big market deficit through year-end", 11/11/2021. [Online]. Available: <https://www.spglobal.com/platts/en/market-insights/latest-news/oil/111121-ope-cuts-2021-oil-demand-outlook-still-sees-big-market-deficit-through-year-end>.

[4] Sheela Tobben and Devika Krishna Kumar, "U.S. sees oil market oversupplied by early next year", 10/11/2021. [Online]. Available: <https://www.bloomberg.com/news/articles/2021-11-09/oil-outlook-biden-s-been-waiting-for-projects-rising-prices>.

[5] Bill Conerly, "Oil forecast 2022 and beyond", 13/11/2021. [Online]. Available: <https://www.forbes.com/sites/billconerly/2021/11/13/oil-forecast-2022-and-beyond/?sh=2f87c9536a67>.